Inter-Bubble Interactions in Ultrasonically Excited Microbubble Clusters

by

Hossein Haghi

B.Sc., Amirkabir University of Technology, 2016

A thesis

presented to Ryerson University

in partial fulfillment of the

requirements for the degree of

Master of Science

in the program of

Biomedical Physics

Toronto, Ontario, Canada, 2018

Author's Declaration

I hereby declare that I am the sole author of this thesis. This is a true copy of the thesis, including any required final revisions, as accepted by my examiners.

I authorize Ryerson University to lend this thesis to other institutions or individuals for the purpose of scholarly research,

I further authorize Ryerson University to reproduce this thesis by photocopying or by other means, in total or in part, at the request of other institutions or individuals for the purpose of scholarly research.

I understand that my thesis may be made electronically available to the public.

Abstract

Inter-Bubble Interactions in Ultrasonically Excited Microbubble Clusters

Hossein Haghi

Master of Science - Biomedical Physics

Ryerson University

2018

Microbubbles (MBs) have been utilized in a variety of applications ranging from medicine to chemistry. There have been extensive studies on many aspects of microbubble dynamics. The majority of previous theoretical studies examine the oscillations of single microbubbles. In most applications multiple microbubbles form clusters. Oscillating microbubbles generate secondary pressure waves in the medium which have been shown to modify the dynamics of neighboring MBs. Large microbubble clusters have not been studied due to the complexity of solving many coupled differential equations governing the dynamics of a large number of microbubbles. This work expands on previous works conducted on the study of multiple bubble interactions. Two approaches are introduced to simulate large clusters. Inter-bubble interactions are classified and used to explain and predict collective behavior within large polydisperse clusters. This work shows that even identical MBs within a monodisperse cluster do not necessarily exhibit identical behavior.

Acknowledgments

I would like to thank my supervisor Dr. Michael Kolios for his support, guidance and the positive environment he has provided for us in the Kolios Lab. This work would not have been possible without the guidance of Amin Jafarisojahrood as he provided insights and advice that helped me throughout this project. Additionally, I would like to extend my gratitude to members of my supervisory committee Dr. Raffi Karshafian and Dr. Meaghan O'Reilly for their critical questions during committee meetings that helped shape this work. Last but definitely not the least, I would like to thank my parents and my brother for their constant positive energy, encouragement and support during this work and supporting me to pursue my interest in biomedical science and research halfway across the world in Canada.

Dedication

I dedicate this work to my father and mother.

Table of Contents

List of Symbols

$m =$ Mass

$t =$ Time

$\rho =$ Density

$\rho_g =$ Gas density

$\mu =$ Viscosity

$s =$ Surface Tension

$\gamma =$ Polytropic exponent

$C_P =$ Specific heat in constant pressure

$C_V =$ Specific heat in constant volume

$P =$ Pressure

$P_0 =$ Initial pressure

$P_{\text{amb}} =$ Ambient pressure

$P_a =$ Pressure amplitude

$P_\infty =$ Pressure in far field

$P_g =$ Gas Pressure

$f =$ Frequency

$f_r =$ Resonance frequency

$f_r^{m/n} =$ m/n resonance frequency

$r =$ Radial component of spherical coordinates

$\dot{r} =$ Radial component of velocity

$\ddot{r} =$ Radial component of acceleration

$\theta =$ Polar angle in spherical coordinates

$\varphi =$ Azimuthal angle in spherical coordinates

$R =$ Instantaneous radius of the bubble

$R_0 =$ Initial radius of the bubble

$\dot{R} =$ Instantaneous bubble wall velocity

$\ddot{R} =$ Instantaneous bubble wall acceleration

$c =$ Speed of sound

$V =$ Volume

$S =$ Surface

$x_i =$ Cartesian coordinate components

$v =$ Velocity

$v_r =$ Radial velocity

$\phi =$ Velocity potential

$\delta_{ij} =$ Dirac's delta

$\Pi_{ij} =$ Momentum flux tensor

$P =$ Pressure

$\sigma_{ij} =$ Momentum transfer tensor due to mass transfer

$\sigma'_{ij} =$ Momentum transfer tensor due to viscosity

$F =$ Force

List of Figures

List of Appendices

1. Introduction

1.1. History

Cavitation refers formation of an empty space, within continuous media. For instance, in case of water it refers to generation of vapor bubbles in regions of low pressure in an incompressible liquid due to Bernoulli's principle. The onset of cavitation was first predicted by Euler as early as 1754 in his work on the theory of turbines (1). However, it was not noticed until the end of nineteenth century. In the development of high speed ships in the British Royal Navy, anticipated higher speeds could not be achieved due to cavitation around the propeller blades. Cavitation reduced performance in ships by thrust breakdown, erosion and vibration. It happens when the propeller operates at very high rotational velocities. If the pressure on the upstream surface of the blade drops below vapor pressure, vapor bubbles will start forming. The collapse of vapor bubbles creates shockwaves eroding the propeller blades. The cavitation erosion problem was first addressed by Parson and Cook (1919) (2) and Rayleigh (1917) (3). Parson and Cook found that bubbles can exert pressures as high as 180 tons per sq. in. on the propeller blades (2). Rayleigh formulated the problem of bubbles as

"*An infinite mass of homogeneous incompressible fluid acted upon by no forces is at rest, and a spherical portion of the fluid is suddenly annihilated; it is required to find the instantaneous alteration of pressure at any point of the mass, and the time in which the cavity will be filled up, the pressure at an infinite distance being supposed to remain constant*"

Rayleigh's work formed the theoretical basis of bubble dynamics later studied by Plesset (4) which derived the Rayleigh-Plesset equation (RPE) that became the foundational equation for

the study of bubble dynamics. Later attempts were focused on expanding the RPE by adding terms to the equation to better model the physics of the bubble oscillation. One of the main assumptions in the RPE is considering the medium to be fully incompressible. Keller and Miksis expanded the RPE into the Keller-Miksis equation (KME) by taking into account the viscosity and surface tension of the medium and the acoustic radiation radiated by oscillating bubbles (5).

Cavitation was mostly found to be a detrimental phenomenon, limiting different applications such as in naval development. In an ultrasound cardiography study performed by Gramiak et al. in 1969, a solution of indocyanine green dye was used to determine cardiac output (6). They observed an unusually significant increase in contrast in acquired ultrasound scans after injection. Upon further investigation, they found that the indocyanine solution was contaminated with a small amount of miniature bubbles. The authors proposed that the bubbles were responsible for the increase in contrast. Kremkau et al. 1970 investigated feasibility of the microbubble idea by Gramiak et al. and discovered that a small amount of cavitation at the injection catheter tips was responsible for the formation of bubbles and the increase in ultrasound contrast (7). This opened a new chapter in bubble dynamics studies: bubbles now had beneficial applications in medicine.

1.2. Background

Further investigations into microbubble dynamics have shown that, despite their simple structure, they exhibit rich oscillatory dynamics under ultrasonic excitation (8). Behavior of ultrasonically driven microbubbles is found to be highly nonlinear, complex and chaotic (9) (10) (11) (12) (13) (14) (15) (16) (17). Different aspects of their complex behavior can be used in applications ranging from medicine to chemistry. MBs play a role in sonoluminescence (18),

oceanography (19), underwater acoustics (20) and medicine (21) (22) (23) (24) (25) (26) (27). For example, owning to their high echogenicity, MBs are employed in ultrasound imaging as contrast agents (28). Furthermore, their nonlinear oscillations generate subharmonics (29) and ultraharmonics (30) which are utilized in diagnostic ultrasound to enhance the detection of vascular tissue as tissue responds linearly to ultrasonic waves (31). At high excitation pressures, MBs can undergo inertial collapse generating shockwaves and high velocity jets which is exploited in shockwave lithotripsy (32). Stable oscillations of MBs can also generate microstreaming in the surrounding liquid (33) exerting shear stress on the nearby objects. The shear stress offers further potential for therapeutic interventions such as site-specific drug and gene delivery (34) through creating pores on the cell membrane (also known as sonoporation) (35) . The same mechanism has been shown to reversibly open the blood brain barrier to deliver macromolecules to better treat CNS disorders and brain cancers (36). MBs are involved in sonoluminescence (37), enhancing the efficacy of chemical reactions in sonochemical reactors (38) (39). In microfluidics, the response of MBs to an applied acoustical field has been utilized to stir or pump liquids on miniature scales (33).

Previous studies are predominantly based on the assumption that MBs within a cluster are sufficiently far apart from each other that their oscillations are independent from one another. Such investigations have provided valuable insight on the dynamic behavior of acoustically excited single isolated MBs in an infinite domain of liquid. Nevertheless, the majority of applications utilizing MBs, and the phenomena associated with them, typically involve dense clusters of polydisperse MBs. Physical models governing the dynamics of interacting bubbles result in sets of a large number of coupled differential equations. Obtaining numerical solutions

for such equations is not as straightforward as it is for single isolated MBs. For this reason, the majority of previous investigations on bubble clusters were limited to a few (<5) interacting bubbles (40) (41) (42). These studies have demonstrated the importance of inter-bubble interactions. However, the small number of bubbles used in such numerical investigations is insufficient to capture the complex emergent patterns of oscillatory bubble dynamics in applications where many bubbles are interacting within a cluster. Here we present two new methods that can be used to solve the system of equations governing the dynamics of large bubble clusters. These methods enable us to simulate oscillations of hundreds of bubbles in bubble clusters efficiently. Using the proposed methods, and for the first time, dynamics of large bubble clusters are studied and new insights are gained from the emergent properties of these clusters.

In this thesis I start from fundamentals of fluid mechanics required to derive the essential equations. In Chapter 1.3 with inclusion of a term describing the scattered pressure from each oscillating bubble at the location of each bubble, KME is expanded for a cluster of bubbles. New contributions to the field first appear in the next section where I introduce numerical approaches to solve the coupled differential equations resulting from the previous formulation, and provide two simple yet effective methods to solve the system of equations. In Chapter 4 my proposed algorithms are verified against analytical solutions for a cluster of 3 and 4 microbubbles. Methods of nonlinear physics are discussed in Chapter 5 that are used to evaluate the response of individual MBs within clusters in a wide range of geometric and ultrasonic parameters. Next, in Chapter 6, the newly developed methods are used to investigate the collective dynamics of individual MBs. Inter-bubble interactions are classified

into two broad categories of constructive and destructive interactions. In Chapter 7 the dynamics of large monodisperse MB clusters are investigated. The first set of simulations use exposures with low pressures the excite the MBs at their natural resonance frequency (for individual MBs). The excitation pressure is then increased to levels which cause changes in the resonant frequency of individual microbubbles (due to pressure dependent resonance), and we study the nonlinear response of the bubble cluster. I show that at lower ultrasound exposure pressures the linear resonance frequency of MBs changes as a function of their number density (number of MBs per unit volume). Furthermore, it is shown that linear resonance frequencies of monodisperse MBs within a cluster are the same for all of the bubbles in the cluster and this resonant frequency decreases with increasing number density due to inter-bubble interactions. Next, for higher ultrasound pressures, the nonlinear resonance frequencies of MBs within monodisperse clusters is studied. It is shown that identical MBs within monodisperse clusters do not exhibit identical oscillatory dynamics due to inter-bubble interactions. Furthermore, I use the proposed classification of inter-bubble interactions (constructive and destructive interactions) to predict and explain the dynamics of MBs within polydisperse clusters.

1.3. Introduction to Fluid Mechanics

Here, I start with a brief introduction to the required fluid mechanics as the basis of understanding the equations of motion governing the dynamics of bubbles in fluids. We will start with equations of motion in an ideal fluid and then expand it to viscous media. The fluid dynamics basis required to derive and understand the physics behind bubble dynamics is presented in this chapter. The discussion and derivations in this chapter are based on (43).

1.3.1. Continuity Equation

We start with an ideal fluid flow where there is no viscosity between different elements of fluid. Suppose we have a volume of V with a surface area of S, the changes in the mass of the fluid within V is

$$\frac{dm}{dt} = -\frac{\partial}{\partial t}\int_V \rho dV \quad (1.1)$$

The incoming, and outgoing mass m into the volume V has to go through the surface S enclosing V, therefore we can write

$$\frac{dm}{dt} = \oint_S \rho\vec{v}.\overrightarrow{dS} \quad (1.2)$$

The surface integral in Eq. 1.2 can be transformed into a volume integral using Green's formula:

$$\oint_S \rho\vec{v}.\overrightarrow{dS} = \int_V \vec{\nabla}.(\rho\vec{v})\, dV \quad (1.3)$$

Using Eqq. 1.1, 1.2 and 1.3 we can write:

$$\int_V \vec{\nabla}.(\rho\vec{v})\, dV = -\frac{\partial}{\partial t}\int_V \rho dV \qquad \rightarrow \qquad \int_V \left[\frac{\partial \rho}{\partial t} + \vec{\nabla}.(\rho\vec{v})\right] dV = 0 \qquad (1.4)$$

Since we considered an arbitrary volume, Eq. 1.4 must hold for any volume, therefore

$$\frac{\partial \rho}{\partial t} + \vec{\nabla}.(\rho \vec{v}) = 0 \qquad (1.5)$$

Eq. 1.5 can be written in tensor notation as

$$\frac{\partial \rho}{\partial t} = -\frac{\partial (\rho v_i)}{\partial x_i} \qquad (1.6)$$

Eqq. 1.5 and 1.6 are referred to as continuity equation which are a form of conservation of mass in fluids and show that changes in the mass of the medium in the volume V, is equal to the amount of mass transferred through enclosing surface S.

1.3.2. Euler's Equation

The force applied to an element in a fluid media can be written as

$$\vec{F} = -\oint_S P\overrightarrow{dS} \qquad (1.7)$$

Transforming the surface integral in Eq. 1.7 to volume integral using Green's formula we have

$$\vec{F} = -\int_V \vec{\nabla} P dV \quad \rightarrow \quad \overrightarrow{dF} = \vec{\nabla} P dV \qquad (1.8)$$

The force applied to a mass dm can also be written as

$$\overrightarrow{dF} = dm\frac{d\vec{v}}{dt} = \rho dV\frac{d\vec{v}}{dt} \qquad (1.9)$$

Equating Eq. 1.8 and 1.9 we can write

$$\rho dV\frac{d\vec{v}}{dt} = \vec{\nabla} P dV \quad \rightarrow \quad \rho\frac{d\vec{v}}{dt} = \vec{\nabla} P \qquad (1.10)$$

In Eq. 1.10, $\frac{\overrightarrow{dv}}{dt}$ refers to changes in speed in the moving elements where the volume V is composed of many elements. The velocity of each element in the volume V is a function of both space and time. Therefore, $d\vec{v}$ can be written as

$$d\vec{v} = \frac{\partial \vec{v}}{\partial x}dx + \frac{\partial \vec{v}}{\partial y}dy + \frac{\partial \vec{v}}{\partial z}dz + \frac{\partial \vec{v}}{\partial t}dt \qquad (1.11)$$

In the right-hand-side of Eq. 1.11, the first three terms refer to changes of speed with location and the fourth term refers to changes in speed of the element with time. Knowing $\overrightarrow{dr} = dx\hat{\imath} + dy\hat{\jmath} + dz\hat{k}$, we have:

$$d\vec{v} = \left(d\vec{r}.\vec{\nabla}\right)\vec{v} + \frac{\partial \vec{v}}{\partial t}dt \qquad (1.12)$$

$$\xrightarrow{\times\frac{1}{dt}} \qquad \frac{d\vec{v}}{dt} = \frac{\left(d\vec{r}.\vec{\nabla}\right)\vec{v}}{dt} + \frac{\partial \vec{v}}{\partial t} \qquad (1.13)$$

$$\rightarrow \quad \frac{d\vec{v}}{dt} = \left(\vec{v}.\vec{\nabla}\right)\vec{v} + \frac{\partial \vec{v}}{\partial t} \qquad (1.14)$$

Using Eq. 1.10 and 1.14 we can write Euler's equation as

$$\left(\vec{v}.\vec{\nabla}\right)\vec{v} + \frac{\partial \vec{v}}{\partial t} = -\frac{1}{\rho}\vec{\nabla}P \qquad (1.15)$$

Rewriting Eq. 1.15 in tensor notation we have

$$v_j\frac{\partial v_i}{\partial x_j} + \frac{\partial v_i}{\partial t} = -\frac{1}{\rho}\frac{\partial P}{\partial x_i} \qquad (1.16)$$

1.3.3. Momentum Flux

Momentum of a unit mass of a fluid with density ρ can be written as $\rho\vec{v}$. Hence, we write the changes with time in the momentum for a unit mass of a fluid as

$$\frac{\partial}{\partial t}(\rho v_i) = \rho\frac{\partial v_i}{\partial t} + v_i\frac{\partial \rho}{\partial t} \quad (1.17)$$

Substituting $\frac{\partial v_i}{\partial t}$ from Euler's equation and using the tensor notation of continuity Eq. 1.6 we have

$$\frac{\partial}{\partial t}(\rho v_i) = -\frac{\partial P}{\partial x_i} - \rho v_j\frac{\partial v_i}{\partial x_j} - v_i\frac{\partial(\rho v_i)}{\partial x_j} \quad (1.18)$$

$$\rightarrow \frac{\partial}{\partial t}(\rho v_i) = -\frac{\partial P}{\partial x_i} - \frac{\partial}{\partial x_j}\left(\rho v_i v_j\right) \quad (1.19)$$

Writing $\frac{\partial P}{\partial x_i}$ as $\delta_{ij}\frac{\partial P}{\partial x_j}$, where δ_{ij} denotes Dirac's delta, we can write Eq. 1.19 as

$$\begin{cases} \dfrac{\partial(\rho v_i)}{\partial t} = -\dfrac{\partial \Pi_{ij}}{\partial x_j} \\ \Pi_{ij} = P\delta_{ij} + \rho v_i v_j \end{cases} \quad (1.20)$$

Π_{ij} is a symmetrical tensor termed as momentum flux density tensor. Π_{ij} represents transfer of momentum in a fluid from one particle to another.

To better understand the physical meaning of Π_{ij} we integrate Eq. 1.20 over a volume V

$$\frac{\partial}{\partial t}\int_V \rho v_i dV = -\int_V \frac{\partial \Pi_{ij}}{\partial x_j} dV \quad (1.21)$$

Using Green's formula, we can transform the right-hand-side of Eq. 1.21 into a surface integral

$$\frac{\partial}{\partial t}\int_V \rho v_i dV = -\oint_S \Pi_{ij}\, dS_j \quad (1.22)$$

The left hand side of Eq. 1.22 represents the rate of ith component of momentum contained in volume V and the right hand side denotes the momentum flowing out through the surface S, enclosing volume V in unit time. The term $\Pi_{ij}\, dS_j$ expresses the ith component of the momentum flowing through the surface S enclosing V.

1.3.4. Equation of Motion in a Viscous Flow – Navier-Stokes Equation

In Eq. 1.20, the momentum transfer is represented as simple mechanical transport from one location to the another and to pressure forces acting in liquid through Π_{ij}. This method of momentum transfer is completely reversible. Viscosity causes an irreversible momentum transfer in the liquid from points with higher velocity to points with lower velocity. Therefore, the equation of motion for a viscous flow can be obtained by addition of a term $-\sigma'_{ij}$ to momentum flux density tensor. $-\sigma'_{ij}$ gives the irreversible transfer of momentum through viscous effects in liquids. Therefore, we have

$$\begin{cases} \Pi_{ij} = P\delta_{ij} + \rho v_i v_j - \sigma'_{ij} = -\sigma_{ij} + \rho v_i v_j \\ \sigma_{ij} = -P\delta_{ij} + \sigma'_{ij} \end{cases} \quad (1.23)$$

The term σ_{ij} is referred to as stress tensor where σ'_{ij} is the viscous component of stress tensor, the viscous stress tensor. σ_{ij} represents the component of momentum transfer that is not due to transfer of mass within the liquid.

Next we are going to derive a mathematical expression for σ'_{ij}. Viscosity can be thought as internal friction in liquids. It only occurs only if neighboring elements in the flow have different

velocities. Therefore, σ'_{ij} must be a function of spatial derivatives of the velocity. For small velocity gradients, which is a valid assumption for neighboring elements in a flow, we can assume that momentum transfer only depends on the first derivatives of the velocity. Therefore, σ'_{ij} should be a linear function of the derivatives $\partial v_i/\partial x_j$. Since no velocity gradient results in zero momentum due to viscosity, σ'_{ij} cannot contain any term independent of $\partial v_i/\partial x_j$s.

In an isotropic fluid, in which there is no preferred direction, the stress tensor, σ_{ij} must be symmetric. Since δ_{ij} is also symmetric, it is required for σ'_{ij} to be a symmetric tensor. Moreover, σ'_{ij} represents the shear stresses resulting from viscosity of fluid, therefore, the sum of its diagonal components must be zero. Following the assumption that σ'_{ij} is a linear function of velocity gradients, we can write

$$\sigma'_{ij} = A_{ijkl}\frac{\partial v_k}{\partial x_l} \qquad (1.24)$$

Where A_{ijkl} is a fourth order tensor since both σ'_{ij} and $\frac{\partial v_k}{\partial x_l}$ are second order tensors. The simplest possible symmetric fourth order tensor we can implement for A_{ijkl} is as follows

$$A_{ijkl} = \alpha\delta_{ij}\delta_{kl} + \beta\delta_{ik}\delta_{jl} + \gamma\delta_{il}\delta_{jk} \qquad (1.25)$$

Where α, β and γ are arbitrary scalars which can be functions of both time and position. Using Eqq. 1.24 and 1.25 we can write σ'_{ij} as

$$\sigma'_{ij} = \alpha\frac{\partial v_k}{\partial x_k}\delta_{ij} + \beta\frac{\partial v_i}{\partial x_j} + \gamma\frac{\partial v_j}{\partial x_i} \qquad (1.26)$$

Since σ'_{ij} should be symmetric, $\sigma'_{ij} = \sigma'_{ji}$, we have

$$\frac{\partial v_k}{\partial x_k}\delta_{ij} + \beta\frac{\partial v_j}{\partial x_i} + \gamma\frac{\partial v_i}{\partial x_j} = \frac{\partial v_k}{\partial x_k}\delta_{ij} + \beta\frac{\partial v_i}{\partial x_j} + \gamma\frac{\partial v_j}{\partial x_i} \quad \rightarrow \beta\frac{\partial v_j}{\partial x_i} + \gamma\frac{\partial v_i}{\partial x_j} = \beta\frac{\partial v_i}{\partial x_j} + \gamma\frac{\partial v_j}{\partial x_i}$$

$$\beta = \gamma \quad (1.27)$$

Therefore, we can write σ'_{ij} as

$$\sigma'_{ij} = \alpha e_{kk}\delta_{ij} + 2\beta e_{ij} \quad (1.28)$$

Where e_{ij} is defined as

$$e_{ij} = \frac{1}{2}\left(\frac{\partial v_i}{\partial x_j} + \frac{\partial v_j}{\partial x_i}\right) \quad (1.29)$$

The tensor e_{ij} is referred to as rate of strain tensor. Finally, since the sum of diagonal components of σ'_{ij} must be zero we have

$$3\alpha e_{ii} + 2\beta e_{ii} = 0 \quad \rightarrow \quad 3\alpha = 2\beta \quad (1.30)$$

Hence, the viscosity stress tensor can be we written as

$$\sigma'_{ij} = 2\mu\left(e_{ij} - \frac{1}{3}e_{kk}\delta_{ij}\right) \quad (1.31)$$

Where $\beta = \mu$. Thus, the most general form of stress tensor in viscous isotropic fluid can be written as

$$\sigma_{ij} = -P\delta_{ij} + 2\mu\left(e_{ij} - \frac{1}{3}e_{kk}\delta_{ij}\right) \qquad (1.32)$$

Using Eqq. 1.32 and 1.23, we can write the momentum flux density tensor as

$$\Pi_{ij} = P\delta_{ij} - 2\mu\left(e_{ij} - \frac{1}{3}e_{kk}\delta_{ij}\right) + \rho v_i v_j \qquad (1.33)$$

Which can be simplified as

$$\Pi_{ij} = P\delta_{ij} - \mu\left(\frac{\partial v_i}{\partial x_j} + \frac{\partial v_j}{\partial x_i} - \frac{2}{3}\delta_{ij}\frac{\partial v_k}{\partial x_k}\right) + \rho v_i v_j \qquad (1.34)$$

Following Eq. 1.20 and 1.32 we can rewrite Euler's equation for a viscous fluid as follows

$$\frac{\partial(\rho v_i)}{\partial t} = -\frac{\partial}{\partial x_j}\left[P\delta_{ij} - \mu\left(\frac{\partial v_i}{\partial x_j} + \frac{\partial v_j}{\partial x_i} - \frac{2}{3}\delta_{ij}\frac{\partial v_k}{\partial x_k}\right) + \rho v_i v_j \right] \qquad (1.35)$$

$$\rho\left[\frac{\partial v_i}{\partial t} + \frac{\partial}{\partial x_j}\left(\rho v_i v_j\right)\right] = -\frac{\partial}{\partial x_j}\left[P\delta_{ij} - \mu\left(\frac{\partial v_i}{\partial x_j} + \frac{\partial v_j}{\partial x_i} - \frac{2}{3}\delta_{ij}\frac{\partial v_k}{\partial x_k}\right) \right] \qquad (1.36)$$

Eq. 1.36 is referred to as Navier-Stokes equation governing motion of a viscous isotropic fluid.

Writing Eq. 1.36 in vector form gives us

$$\rho\left[\frac{\partial v}{\partial t} + \left(\vec{v}.\vec{\nabla}\right).\vec{v}\right] = -\vec{\nabla}P + \mu\left[\nabla^2\vec{v} + \frac{1}{3}\vec{\nabla}\left(\vec{\nabla}.\vec{v}\right)\right] \qquad (1.37)$$

1.3.5. Spherical Coordinate System

Here we are going to rewrite Navier-Stokes (Eq. 1.37) in spherical coordinate system as it is the most useful framework to study bubble oscillations.

First, we need different components of stress tensor in spherical coordinates. Stress tensor is a second order tensor which can be written as follows

$$\sigma = \begin{pmatrix} \sigma_{rr} & \sigma_{r\theta} & \sigma_{r\varphi} \\ \sigma_{\theta r} & \sigma_{\theta\theta} & \sigma_{\theta\varphi} \\ \sigma_{\varphi r} & \sigma_{\varphi\theta} & \sigma_{\varphi\varphi} \end{pmatrix} \qquad \sigma_{ij} = \sigma_{ji} \qquad (1.38)$$

Elements of stress tensor matrix in Eq. 1.38 in spherical coordinates can be written as

$$\sigma_{ij} = \begin{cases} \sigma_{rr} = -P + 2\mu \dfrac{\partial v_r}{\partial r} \\ \sigma_{\theta\theta} = -P + 2\mu \left(\dfrac{1}{r} \dfrac{\partial v_\theta}{\partial \theta} + \dfrac{v_r}{r} \right) \\ \sigma_{\varphi\varphi} = -P + 2\mu \left(\dfrac{1}{r \sin\theta} \dfrac{\partial v_\theta}{\partial \varphi} + \dfrac{v_r}{r} + \dfrac{v_\theta \cot\theta}{r} \right) \\ \sigma_{r\theta} = \mu \left(\dfrac{1}{r} \dfrac{\partial v_\theta}{\partial \theta} + \dfrac{\partial v_\theta}{\partial r} - \dfrac{v_\theta}{r} \right) \\ \sigma_{\theta\varphi} = \mu \left(\dfrac{1}{r \sin\theta} \dfrac{\partial v_\theta}{\partial \varphi} + \dfrac{1}{r} \dfrac{\partial v_\varphi}{\partial \theta} - \dfrac{v_\varphi \cot\theta}{r} \right) \\ \sigma_{\varphi r} = \mu \left(\dfrac{\partial v_\varphi}{\partial r} + \dfrac{1}{r \sin\theta} \dfrac{\partial v_r}{\partial \varphi} - \dfrac{v_\varphi}{r} \right) \end{cases} \quad (1.39)$$

Using Eq. 1.39, we can rewrite three components of Navier-Stokes equation in spherical coordinates as follows

$$\begin{cases} \dfrac{\partial v_r}{\partial t} + (\vec{v}.\vec{\nabla}) v_r - \dfrac{v_\theta^2 + v_\varphi^2}{r} = -\dfrac{1}{\rho} \dfrac{\partial P}{\partial r} + \dfrac{\mu}{\rho} \left[\nabla^2 v_r - \dfrac{2}{r^2 \sin^2\theta} \dfrac{\partial (v_\theta \sin\theta)}{\partial \theta} - \dfrac{2}{r^2 \sin\theta} \dfrac{\partial v_\varphi}{\partial \varphi} - \dfrac{2 v_r}{r^2} \right] \\ \dfrac{\partial v_\theta}{\partial t} + (\vec{v}.\vec{\nabla}) v_\theta + \dfrac{v_r v_\theta}{r} - \dfrac{v_\varphi^2 \cot\theta}{r} = -\dfrac{1}{\rho r} \dfrac{\partial P}{\partial \theta} + v \left[\nabla^2 v_\theta - \dfrac{2\cos\theta}{r^2 \sin^2\theta} \dfrac{\partial v_\varphi}{\partial \varphi} + \dfrac{2}{r^2} \dfrac{\partial v_r}{\partial \theta} - \dfrac{v_\theta}{r^2 \sin^2\theta} \right] \\ \dfrac{\partial v_\varphi}{\partial t} + (\vec{v}.\vec{\nabla}) v_\varphi + \dfrac{v_r v_\varphi}{r} - \dfrac{v_\theta v_\varphi \cot\theta}{r} = -\dfrac{1}{\rho r \sin\theta} \dfrac{\partial P}{\partial \varphi} + v \left[\nabla^2 v_\varphi - \dfrac{2}{r^2 \sin^2\theta} \dfrac{\partial v_r}{\partial \varphi} + \dfrac{2\cos\theta}{r^2 \sin^2\theta} \dfrac{\partial v_\theta}{\partial \varphi} - \dfrac{v_\varphi}{r^2 \sin^2\theta} \right] \end{cases} \quad (1.40)$$

Where

$$(\vec{v}.\vec{\nabla}) X = v_r \frac{\partial X}{\partial r} + \frac{v_\theta}{r} \frac{\partial X}{\partial \theta} + \frac{v_\varphi}{r \sin\theta} \frac{\partial X}{\partial \varphi} \quad (1.41)$$

$$\nabla^2 X = \frac{1}{r^2} \frac{\partial}{\partial r} \left(r^2 \frac{\partial X}{\partial r} \right) + \frac{1}{r^2 \sin\theta} \frac{\partial}{\partial \theta} \left(\sin\theta \frac{\partial X}{\partial \theta} \right) + \frac{1}{r^2 \sin^2\theta} \frac{\partial^2 X}{\partial \varphi^2} \quad (1.42)$$

2. Bubble Dynamics

In this chapter, the concepts introduced in previous chapter are applied to the problem of bubbles in a fluid domain for three scenarios. First, we will consider a single isolated bubble in an infinite domain of incompressible fluid (4). Second, a degree of compressibility will be given to the medium allowing for propagation of acoustic waves in the media. However, the extent of compressibility is as such that we can assume that the changes in the density of the media is negligible (5). This will allow the bubble to lose energy in the form of acoustic radiation. Having established secondary wave propagation in the medium, the pressure amplitude of this wave will be derived. Lastly, we will consider an arbitrary number of bubbles in an infinite domain of liquid. Dynamics of bubbles will be coupled to one another through acoustic radiation emitted from each oscillating bubble (42).

2.1. Single Bubble in an Incompressible Fluid

Let us consider a spherical bubble of initial radius R_0 and instantaneous radius of R with an internal gas pressure of P_g in an infinite domain of fluid with the ambient pressure of P_o. We start with calculating the pressure resulting from the surface tension s in the water-gas interface as follows

$$F_s = 2\pi R s \quad (2.1)$$

$$P_s = \frac{F_s}{A} = \frac{2\pi R s}{\pi R^2} = \frac{2s}{R} \quad (2.2)$$

If we consider the mass of the gas inside the bubble, m_g, we have

$$m_g = \frac{4}{3}\pi r^3 \rho_g \quad (2.3)$$

$$\frac{\partial m_g}{\partial t} = 4\pi r^2 \dot{r} \rho_g \quad (2.4)$$

$$\xrightarrow{G(t)=\frac{\partial m_g}{\partial t}\frac{1}{4\pi\rho_g}} \quad \dot{r} = \frac{G(t)}{r} \qquad (2.5)$$

We assumed the bubble to maintain its spherical symmetry, therefore in the Navier-Stokes equation in spherical coordinates (Eq. 1.40), we are only left with the radial terms. Hence, we have

$$-\frac{1}{\rho_L}\frac{\partial P}{\partial r} = \frac{\partial v_r}{\partial t} + v_r\frac{\partial v_r}{\partial r} - \frac{\mu}{\rho_L}\left[\frac{1}{r^2}\frac{\partial}{\partial r}\left(r^2\frac{\partial v_r}{\partial r}\right) - \frac{2v_r}{r^2}\right] \qquad (2.6)$$

In Eq. 2.6, the term v_r denotes the radial velocity of the flow. We are interested to solve Eq. 2.6 at the location of the bubble wall at which flow velocity is equal to the velocity of the bubble wall ($v_r = \dot{R}$) calculated in Eq. 2.5. Therefore, substituting Eq. 2.5 in 2.6 will give us

$$-\frac{1}{\rho_L}\frac{\partial P}{\partial r} = \frac{\partial}{\partial t}\left(\frac{G(t)}{r^2}\right) + \left(\frac{G(t)}{r^2}\right)\frac{\partial}{\partial r}\left(\frac{G(t)}{r^2}\right) - \frac{\mu}{\rho_L}\left[\frac{1}{r^2}\frac{\partial}{\partial r}\left(r^2\frac{\partial}{\partial r}\left(\frac{G(t)}{r^2}\right)\right) - \frac{2}{r^2}\left(\frac{G(t)}{r^2}\right)\right] \quad (2.7)$$

Expanding Eq. 2.7

$$-\frac{1}{\rho_L}\frac{\partial P}{\partial r} = \frac{\dot{G}(t)}{r^2} + \left(\frac{G(t)}{r^2}\right)\left(\frac{-2G(t)}{r^3}\right) - \frac{\mu}{\rho_L}\left[\frac{1}{r^2}\frac{\partial}{\partial r}\left(\frac{-2G(t)}{r}\right) - \frac{2G(t)}{r^4}\right] \qquad (2.8)$$

$$-\frac{1}{\rho_L}\frac{\partial P}{\partial r} = \frac{\dot{G}(t)}{r^2} + \frac{G^2(t)}{r^5} - \frac{\mu}{\rho_L}\left[\frac{2G(t)}{r^4} - \frac{2G(t)}{4}\right] \quad (2.9)$$

$$-\frac{1}{\rho_L}\frac{\partial P}{\partial r} = \frac{\dot{G}(t)}{r^2} + \frac{G^2(t)}{r^5} \quad (2.10)$$

Integrating Eq. 2.10 from R to ∞ yields

$$-\frac{1}{\rho_L}\int_{P_{r=R}}^{P_r=\infty} dP = \int_R^{\infty}\left(\frac{\dot{G}(t)}{r^2} + \frac{G^2(t)}{r^5}\right)dr \quad (2.11)$$

$$\frac{P_{r=R} - P_\infty}{\rho_L} = \frac{\dot{G}(t)}{R} - \frac{G^2}{2R^4} \quad (2.12)$$

To solve Eq. 2.12, we need to consider the boundary conditions at the bubble wall. Consider an infinitesimal film on a bubble wall shown in Fig. 2.1.

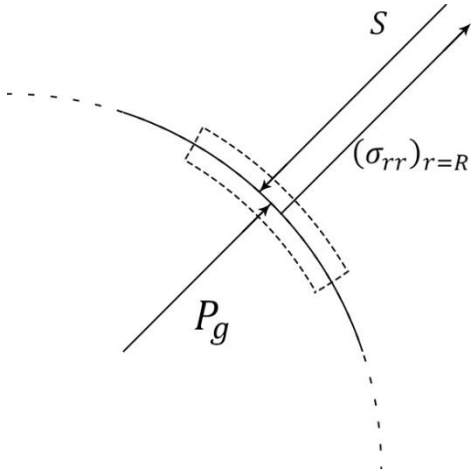

Figure 2.1- Stresses acting on an infinitesimal film on a bubble wall

The total stress acting on the film can be written as

$$\sigma_T = F_{\text{unit Area}} = (\sigma_{rr})_{r=R} + P_g - \frac{2s}{R} \quad (2.13)$$

The normal tensor vector, $(\sigma_{rr})_{r=R}$ was calculated in spherical coordinates in the previous chapter. Substituting Eq. 2.5 into 1.39 yields

$$\begin{cases} \sigma_{rr} = -P + 2\mu \dfrac{\partial v_r}{\partial r} \\ \dot{r} = \dfrac{F(t)}{r^2} \end{cases} \rightarrow (\sigma_{rr})_{r=R} = -P_{r=R} + 2\mu\left(\frac{-2F(t)}{R^3}\right) \quad (2.14)$$

$$(\sigma_{rr})_{r=R} = -P_{r=R} + 2\mu\left(-\frac{2R^2\dot{R}}{R^3}\right) = -P_{r=R} - \frac{4\mu\dot{R}}{R} \quad (2.15)$$

In absence of mass transfer across the bubble wall, the total forces acting on unit area of its wall must be zero. Therefore, substituting Eq. 2.13 into 2.15 results in:

$$F_{\text{unit Area}} = -P_{r=R} - \frac{4\mu\dot{R}}{R} + P_g - \frac{2s}{R} = 0 \quad (2.16)$$

$$P_{r=R} = P_g - \frac{4\mu\dot{R}}{R} - \frac{2s}{R} \quad (2.17)$$

Therefore, now using expressions 2.5, 2.12 and 2.17 we can write

$$\begin{cases} \dfrac{P_{r=R} - P_\infty}{\rho_L} = \dfrac{\dot{F}(t)}{R} - \dfrac{F^2}{2R^4} \\ P_{r=R} = P_g - \dfrac{4\mu\dot{R}}{R} - \dfrac{2s}{R} \\ F(t) = R^2\dot{R} \end{cases} \rightarrow \quad \frac{P_g - P_\infty}{\rho_L} = R\ddot{R} + \frac{3}{2}\dot{R}^2 + \frac{4\mu\dot{R}}{\rho_L R} + \frac{2s}{\rho_L R} \quad (2.18)$$

Eq. 2.18 is known as the Rayleigh-Plesset equation first introduced by Plesset in 1949.

$$\frac{P_g(t) - P_\infty(t)}{\rho_L} = R\ddot{R} + \frac{3}{2}\dot{R}^2 + \frac{4\mu\dot{R}}{\rho_L R} + \frac{2S}{\rho_L R} \quad (2.19)$$

2.2. Single Bubble in a Compressible Fluid (Acoustic Approximation)

Consider a single bubble in an infinite domain of liquid. The liquid is considered to be compressible allowing the propagation of acoustic waves in the medium. However, we assume that propagated pressure fields have a much lower amplitude than the background pressure in

the medium. Therefore, it is reasonable to assume that the changes in the density of the medium in areas of low and high pressure are small and can be negligible. This is a consequence of the fact that water has a very large bulk modulus (2.2 GPa) (44).

A further assumption is that the flow around the bubble is non-rotational. Therefore, we can define a velocity potential in the flow and exploit it in our calculations. We start with the non-rotational flow, we have

$$\vec{\nabla} \times \vec{v} = 0 \;\rightarrow\; \begin{vmatrix} \hat{\imath} & \hat{\jmath} & \hat{k} \\ \frac{\partial}{\partial x} & \frac{\partial}{\partial y} & \frac{\partial}{\partial z} \\ v_x & v_y & v_z \end{vmatrix} = 0 \qquad (2.20)$$

$$\rightarrow \quad \hat{\imath}\left(\frac{\partial v_z}{\partial y} - \frac{\partial v_y}{\partial z}\right) - \hat{\jmath}\left(\frac{\partial v_z}{\partial x} - \frac{\partial v_x}{\partial z}\right) + \hat{k}\left(\frac{\partial v_y}{\partial x} - \frac{\partial v_x}{\partial y}\right) = 0 \qquad (2.21)$$

$$\rightarrow \quad \begin{cases} \frac{\partial v_z}{\partial y} = \frac{\partial v_y}{\partial z} \\ \frac{\partial v_z}{\partial x} = \frac{\partial v_x}{\partial z} \\ \frac{\partial v_y}{\partial x} = \frac{\partial v_x}{\partial y} \end{cases} \qquad (2.22)$$

Now we are going to expand $\vec{\nabla}(\vec{\nabla}.\vec{v})$

$$\vec{\nabla}(\vec{\nabla}.\vec{v}) = \vec{\nabla}\left(\frac{\partial v_x}{\partial x} + \frac{\partial v_y}{\partial y} + \frac{\partial v_z}{\partial z}\right) \quad (2.23)$$

$$\vec{\nabla}(\vec{\nabla}.\vec{v}) = \hat{\imath}\left(\frac{\partial^2 v_x}{\partial x^2} + \frac{\partial^2 v_y}{\partial y \partial x} + \frac{\partial^2 v_z}{\partial z \partial x}\right) + \hat{\jmath}\left(\frac{\partial^2 v_x}{\partial x \partial y} + \frac{\partial^2 v_y}{\partial y^2} + \frac{\partial^2 v_z}{\partial z \partial y}\right) + \hat{k}\left(\frac{\partial^2 v_x}{\partial x \partial z} + \frac{\partial^2 v_y}{\partial y \partial z} + \frac{\partial^2 v_z}{\partial z^2}\right)$$

$$= \hat{\imath}\left[\frac{\partial^2 v_x}{\partial x^2} + \frac{\partial}{\partial y}\left(\frac{\partial v_y}{\partial x}\right) + \frac{\partial}{\partial z}\left(\frac{\partial v_z}{\partial x}\right)\right] + \hat{\jmath}\left[\frac{\partial}{\partial x}\left(\frac{\partial v_x}{\partial y}\right) + \frac{\partial^2 v_y}{\partial y^2} + \frac{\partial}{\partial z}\left(\frac{\partial v_z}{\partial y}\right)\right]$$

$$+ \hat{k}\left[\frac{\partial}{\partial x}\left(\frac{\partial v_x}{\partial z}\right) + \frac{\partial}{\partial y}\left(\frac{\partial v_y}{\partial z}\right) + \frac{\partial^2 v_z}{\partial z^2}\right] \qquad (2.23)$$

Using relations established in Eq. 2.22, we have

$$\vec{\nabla}(\vec{\nabla}.\vec{v}) = \hat{\imath}\left[\frac{\partial^2 v_x}{\partial x^2} + \frac{\partial}{\partial y}\left(\frac{\partial v_x}{\partial y}\right) + \frac{\partial}{\partial z}\left(\frac{\partial v_x}{\partial z}\right)\right] + \hat{\jmath}\left[\frac{\partial}{\partial x}\left(\frac{\partial v_y}{\partial x}\right) + \frac{\partial^2 v_y}{\partial y^2} + \frac{\partial}{\partial z}\left(\frac{\partial v_y}{\partial z}\right)\right]$$

$$+ \hat{k}\left[\frac{\partial}{\partial x}\left(\frac{\partial v_z}{\partial x}\right) + \frac{\partial}{\partial y}\left(\frac{\partial v_z}{\partial y}\right) + \frac{\partial^2 v_z}{\partial z^2}\right] \qquad (2.24)$$

$$\rightarrow \vec{\nabla}(\vec{\nabla}.\vec{v}) = \hat{\imath}\left(\frac{\partial^2 v_x}{\partial x^2} + \frac{\partial^2 v_x}{\partial y^2} + \frac{\partial^2 v_x}{\partial z^2}\right) + \hat{\jmath}\left(\frac{\partial^2 v_y}{\partial x^2} + \frac{\partial^2 v_y}{\partial y^2} + \frac{\partial^2 v_y}{\partial z^2}\right) + \hat{k}\left(\frac{\partial^2 v_z}{\partial x^2} + \frac{\partial^2 v_z}{\partial y^2} + \frac{\partial^2 v_z}{\partial z^2}\right)$$

$$= (\vec{\nabla}.\vec{\nabla})\vec{v} = \nabla^2\vec{v} \qquad (2.25)$$

Therefore, we have established that if a flow is non-rotational, the gradient of divergence of the flow velocity is equal to the Laplacian of the flow velocity. Using this fact, we can simplify the Navier-Stokes equation (Eq. 1.37) as follows

$$\rho\left[\frac{\partial v}{\partial t} + (\vec{v}.\vec{\nabla}).\vec{v}\right] = -\vec{\nabla}P + \frac{4\mu}{3}\nabla^2\vec{v} \qquad (2.26)$$

At the bubble wall, the velocity of the flow is equal to radial velocity of the bubble wall. Moreover, in a non-rotational flow, we can define a velocity potential as follow

$$\begin{cases} v_{r=R} = \dfrac{\partial R}{\partial t} \\ v = \dfrac{\partial \phi(r,t)}{\partial r} \end{cases} \rightarrow \quad \frac{\partial R}{\partial t} = \left.\frac{\partial \phi(r,t)}{\partial r}\right|_{r=R} \qquad (2.27)$$

Using Eq. 2.27 in the radial component of simplified Navier-Stokes Eq. 2.26 yields

$$\rho_L\left[\frac{\partial}{\partial t}\left(\frac{\partial \phi}{\partial r}\right)+\frac{\partial \phi}{\partial r}\left(\frac{\partial}{\partial r}\left(\frac{\partial \phi}{\partial r}\right)\right)\right]+\frac{\partial P}{\partial r}=\frac{4\mu}{3}\frac{\partial}{\partial r}\left(\frac{\partial^2 \phi}{\partial r^2}\right) \qquad (2.28)$$

Integrating Eq. 2.28 from R to ∞ yields

$$\int_R^{\infty}\left[\frac{\partial}{\partial t}\left(\frac{\partial \phi}{\partial r}\right)+\frac{\partial \phi}{\partial r}\left(\frac{\partial}{\partial r}\left(\frac{\partial \phi}{\partial r}\right)\right)\right]dr+\frac{1}{\rho_L}\int_{P_{r=R}}^{P_\infty}\frac{\partial P}{\partial r}dr=\frac{4\mu}{3\rho_L}\int_r^R\frac{\partial}{\partial r}\left(\frac{\partial^2 \phi}{\partial r^2}\right)dr \quad (2.29)$$

$$\frac{\partial \phi}{\partial t}+\frac{1}{2}\left(\frac{\partial \phi}{\partial r}\right)^2+\frac{P_{r=R}-P_\infty}{\rho_L}=\frac{4\mu}{3\rho_L}\frac{\partial^2 \phi}{\partial r^2} \quad (2.30)$$

recall the stress tensor relation (Eq. 1.32) derived in previous chapter

$$\sigma_{ij}=-P\delta_{ij}+2\mu\left(e_{ij}-\frac{1}{3}e_{kk}\delta_{ij}\right)$$

Therefore, for the radial component of the stress tensor we can write

$$\sigma_{rr}=-P_r+2\mu\left(\frac{\partial v_r}{\partial r}-\frac{1}{3}\frac{\partial v_k}{\partial x_k}\right) \;\rightarrow\; \sigma_{rr}=-P_r+2\mu\left(\frac{\partial v_r}{\partial r}-\frac{1}{3}\left(\vec{\nabla}.\vec{v}\right)_r\right) \qquad (2.31)$$

We can rewrite $\left(\vec{\nabla}.\vec{v}\right)_r$ as

$$\left(\vec{\nabla}.\vec{v}\right)_r=\frac{1}{r^2}\frac{\partial}{\partial r}(r^2 v_r)=\frac{2v_r}{r}+\frac{\partial v_r}{\partial r} \quad (2.32)$$

Substituting Eq. 2.32 in 2.31 results in

$$\sigma_{rr}=-P_r+2\mu\left(\frac{\partial v_r}{\partial r}-\frac{2v_r}{3r}-\frac{1}{3}\frac{\partial v_r}{\partial r}\right) \qquad (2.33)$$

$$\sigma_{rr}=-P_r+\frac{4\mu}{3}\left(\frac{\partial v_r}{\partial r}-\frac{v_r}{r}\right) \quad (3.34)$$

Since we have considered the flow as non-rotational, we can write

$$\sigma_{rr} = -P_r + \frac{4\mu}{3}\left(\frac{\partial}{\partial r}\left(\frac{\partial \phi}{\partial r}\right) - \frac{1}{r}\left(\frac{\partial \phi}{\partial r}\right)\right) \quad (2.35)$$

$$\sigma_{rr} = -P_r + \frac{4\mu}{3}\left(\frac{\partial^2 \phi}{\partial r^2} - \frac{1}{r}\left(\frac{\partial \phi}{\partial r}\right)\right) \quad (2.36)$$

Now we can write the total stress acting on the bubble wall. Since there is no mass transfer allowed across the bubble wall, total stress at bubble wall should be zero. Hence, we have

$$\sigma_{rr} = P_g - P_{r=R} + \frac{4\mu}{3}\left(\left.\frac{\partial^2 \phi}{\partial r^2}\right|_{r=R} - \frac{1}{R}\left.\frac{\partial \phi}{\partial r}\right|_{r=R}\right) - \frac{2S}{R} = 0 \quad (2.37)$$

Therefore, we can find the pressure at the bubble wall as

$$P_{r=R} = P_g - \frac{2S}{R} + \frac{4\mu}{3}\left(\left.\frac{\partial^2 \phi}{\partial r^2}\right|_{r=R} - \frac{1}{R}\left.\frac{\partial \phi}{\partial r}\right|_{r=R}\right) \quad (2.38)$$

Inserting Eq. 2.38 into 2.30 yields

$$\Delta(R) = \frac{P_g - P_\infty}{\rho_L} = -\left.\frac{\partial \phi}{\partial t}\right|_{r=R} - \frac{1}{2}\left(\left.\frac{\partial \phi}{\partial r}\right|_{r=R}\right)^2 \frac{2S}{R\rho_L} + \frac{4\mu}{\rho_L R}\left.\frac{\partial \phi}{\partial r}\right|_{r=R} \quad (2.39)$$

An oscillating bubble in a compressible medium will emit acoustic radiation itself. Emitted radiation will result in a loss of net energy within the bubble system and dampens the oscillations. This is in fact referred to as radiation damping. To analyze this effect, we employ the acoustic approximation and therefore consider the density of the medium as constant. T\he wave equation for an spherical velocity potential propagating in a medium with a speed of c can be written as

$$\frac{\partial^2\phi(r,t)}{\partial t^2} - c^2\frac{\partial^2\phi(r,t)}{\partial r^2} = 0 \qquad (2.40)$$

The most general solution for Eq. 2.40 can be written as

$$\phi(r,t) = \frac{f\left(t-\frac{r}{c}\right) + g\left(t+\frac{r}{c}\right)}{r} \qquad (2.41)$$

Where functions f and g respectively represent an outward and inward propagating wave.

Taking the time and space derivate of $\phi(r,t)$ yields

$$\begin{cases} \dfrac{\partial\phi}{\partial t} = \dfrac{f'+g'}{r} \\ \dfrac{\partial\phi}{\partial r} = \dfrac{g'-f'}{rc} - \dfrac{f'+g'}{r^2} \end{cases} \qquad (2.42)$$

The spatial derivatives in Eqq. 2.42 can be written as

$$\frac{\partial\phi}{\partial r} = -\frac{g'+f'}{rc} - \frac{f'+g'}{r^2} + \frac{2g'}{rc} \quad \rightarrow \quad \frac{\partial\phi}{\partial r} = -\frac{1}{c}\frac{\partial\phi}{\partial t} - \frac{\phi}{r} + \frac{2g'}{rc} \qquad (2.43)$$

At the location of the bubble wall we can write

$$\dot{R} = -\frac{1}{c}\frac{\partial\phi(r,t)}{\partial t}\bigg|_{r=R} - \frac{\phi(R,t)}{R} + \frac{2g'}{Rc}$$

$$\xrightarrow{\times cR} \quad -R\frac{\partial\phi}{\partial t}\bigg|_{r=R} = cR\dot{R} + c\phi - 2g' \qquad (2.44)$$

Using Eqq. 2.44 and 2.39 we can rewrite $R\Delta(R)$ as

$$R\Delta(R) = cR\dot{R} + c\phi - 2g' - \frac{R\dot{R}^2}{2} + \frac{4\mu\dot{R}}{\rho_L} + \frac{2S}{\rho_L} \qquad (2.45)$$

Taking the time derivative of Eq. 2.45 yields

$$\dot{R}\Delta(R) + R\dot{\Delta}(R) = c\dot{R}^2 + cR\ddot{R} + c\dot{\phi} - 2\left(1 + \frac{\dot{R}}{c}\right)g'' - \frac{\dot{R}^3}{2} - R\dot{R}\ddot{R} + \frac{4\mu}{\rho_L}\ddot{R} \qquad (2.46)$$

Using Eqq. 2.39 and 2.46 we can write

$$\dot{R}\Delta(R) + R\dot{\Delta}(R)$$
$$= c\dot{R}^2 + cR\ddot{R} + c\Delta(R) - \frac{c\dot{R}^2}{2} + c\left(\frac{4\mu\dot{R}}{\rho_L R} + \frac{2S}{\rho_L R}\right) - \frac{\dot{R}^3}{2} - R\dot{R}\ddot{R} + \frac{4\mu}{\rho_L}\ddot{R}$$
$$- 2\left(1 + \frac{\dot{R}}{c}\right)g'' \qquad (2.47)$$

Assuming that the second derivative of the incoming wave is negligible, we can rearrange 2.47 as

$$\begin{cases} \ddot{R} = \dfrac{-\dfrac{\dot{R}^2}{2}\left(3 - \dfrac{\dot{R}}{c}\right) + \left(1 + \dfrac{\dot{R}}{c} + \dfrac{d}{dt}\right)\Delta(R) - \dfrac{4\mu\dot{R}}{\rho_L R} - \dfrac{2S}{\rho_L R}}{R\left(1 - \dfrac{\dot{R}}{c}\right) + \dfrac{4\mu}{\rho c}} \\ \Delta(R) = \dfrac{P_g - P_\infty}{\rho} \end{cases} \qquad (2.48)$$

Eq. 2.48 is known as the Keller-Miksis equation, first derived by Keller and Miksis in 1980. This equation describes the dynamics of an isolated spherically bubble in an infinite domain of compressible liquid. The main difference between Keller-Miksis and the Rayleigh-Plesset equation lies in the mechanism of acoustic radiation damping considered in the Keller-Miksis equation.

2.3. Pressures Fields Emitted by an Oscillating Bubble (Acoustic Approximation)

Assume a bubble is expanding in an infinite domain of liquid. The expansion of the bubble will result in liquid mass displacement at the location of bubble wall and also at a distance r away from center of the bubble. Mass displacement at the location of bubble can be written as

$$\frac{dm}{dt} = 4\pi R^2 \dot{R} \rho_L \quad (2.49)$$

Furthermore, mass displacement at r can be written as

$$\frac{dm}{dt} = 4\pi r^2 v_r \rho_L \quad (2.50)$$

where v_r is the radial velocity of the moving fluid as a result of the bubble expansion at r. Due to acoustic approximation, the density of the medium, ρ_L is assumed constant and therefore mass displacement at the location of bubble and away from bubble must be equal. Hence, we can write.

$$4\pi R^2 \dot{R} \rho_L = 4\pi r^2 v_r \rho_L \quad \rightarrow \quad v_r = \frac{R^2 \dot{R}}{r^2} \quad (2.51)$$

Having the velocity of the flow away from the pulsating bubble, and considering the spherical symmetry of the bubble, we can use the radial component of Euler's equation to obtain the pressure radiated by the pulsating bubble at r.

$$v_r \frac{\partial v_r}{\partial r} + \frac{\partial v_r}{\partial t} = -\frac{1}{\rho_L} \frac{\partial P}{\partial r} \quad (2.52)$$

Substituting Eq. 2.51 in 2.52 yields

$$\frac{R^2\dot{R}}{r^2}\frac{\partial}{\partial r}\left(\frac{R^2\dot{R}}{r^2}\right)+\frac{\partial}{\partial t}\left(\frac{R^2\dot{R}}{r^2}\right)=-\frac{1}{\rho_L}\frac{\partial P}{\partial r} \quad (2.53)$$

$$\frac{2R^4\dot{R}^2}{r^5}+\frac{2R\dot{R}^2+R^2\ddot{R}}{r^2}=-\frac{1}{\rho_L}\frac{\partial P}{\partial r} \quad (2.54)$$

In Eq. 2.54, we can omit the first term on the left-hand-side since it is in the order of r^{-5} and has a negligible contribution to the pressure gradient at r. Therefore, we have

$$\frac{\partial P}{\partial r}=-\rho\frac{2R\dot{R}^2+R^2\ddot{R}}{r^2} \quad (2.55)$$

Integrating Eq. 2.54 will result in the pressure field a distance r away from the center of the pulsating bubble. We denote this term as P_{sc}, scattered pressure from the pulsating bubble

$$P_{sc}(r)=\rho\frac{2R\dot{R}^2+R^2\ddot{R}}{r} \quad (2.56)$$

It is important to note that in derivation of Eq. 2.56, the medium is considered to maintain a constant density. For instance, this assumption is invalid in the case of inertial collapse where the bubble wall velocity becomes comparable to the speed of sound in the medium. Moreover, each bubble will oscillate in response to two main acoustic waves, the primary acoustic wave sent by the transducer and the scattering of the primary wave by oscillation of bubbles (secondary waves, Eq. 2.56). Generally, since the speed of sound is finite, the primary acoustic wave will be incident on each bubble in the modelled cluster at a different time. This can be neglected if the travel time of the primary wave is much smaller than the time scale of the oscillations. Furthermore, the secondary scattered acoustic waves also travel for a finite amount of time to reach the neighboring bubbles. However, most of the inter-bubble distances are smaller than the scale of the cluster itself (for which we can neglect travel time of the primary wave). Therefore, it is a reasonable assumption to neglect the inter-bubble wave travel time for the secondary acoustic waves.

3. Multiple Interacting Bubbles in an Infinite Domain of Liquid

In this chapter, we are going to derive the governing equations describing the dynamics of multiple bubbles in an infinite domain of liquid (42). Pulsating bubbles will produce secondary pressure waves that need to be included into the Keller-Miksis equation. We will see that in this MB ensemble, oscillations of each bubble is coupled to oscillations of all the rest of the bubbles in the cluster. This will introduce an additional challenge in solving the governing equations as the system of equations becomes large and hard to solve for a large (N>4) number of bubbles. Two new methods I have developed to address the complexity will be introduced. The key advantage of the proposed methods is that they do not require any additional simplifying assumptions that may limit their application. Another key advantage of the proposed methods is their scalability; one can use the introduced algorithms to scale up the governing equations to model many interacting bubbles up to an arbitrary number of bubbles. Since the method introduced solely relies on numerical solutions, the only limitation of the method may be the available computational resources. Both methods will be compared to previous solutions for two, three and four bubbles. To test the algorithm, the distance between bubbles will be increased to verify whether the MB oscillations at large distances from each other are similar to those of isolated bubbles.

3.1. Governing Equations

In the previous chapter, we derived the Keller-Miksis equation (Eq. 2.48) to describe the dynamics of a single isolated bubble in an infinite liquid domain. The Keller-Miksis equation includes the effect of acoustic radiation damping in bubble oscillations. In a more realistic scenario, we can assume that a part of the energy that is lost in the form of acoustic radiation is received by neighboring bubbles in the form of secondary acoustic fields. The secondary acoustic fields radiated by each individual bubble will change the pressure at the wall of each and every bubble in its proximity. The pressure generated by these secondary fields from the MB oscillations is given by Eq. 2.56. Inspection of the equations reveals that the magnitude of the secondary acoustic field is inversely proportional to the distance between the bubbles. Eq. 2.56 also shows that backscattered pressure is directly related to oscillations of the bubble: it depends on the instantaneous the radius of the bubble and the radial velocity and acceleration of the bubble wall. We can rewrite Eq. 2.48 as follows

$$\begin{cases} \left(1-\frac{\dot{R}}{c}\right)R\ddot{R}+\frac{3}{2}\dot{R}^2\left(1-\frac{\dot{R}}{3c}\right)=\frac{P_B\left(R,\dot{R},t\right)}{\rho} \\ P_B\left(R,\dot{R},t\right)=\left(1+\frac{\dot{R}}{c}+\frac{R}{c}\frac{d}{dt}\right)\left[P_g(t)-P_\infty(t)-\frac{4\mu\dot{R}_i}{R_i}-\frac{2\sigma}{R_i}\right] \end{cases} \tag{3.1}$$

where the term $P_B(R,\dot{R},t)$ is the pressure at the bubble wall. For simplicity, we are going to considered no heat and mass transfer across the bubble wall allowing us to rewrite $P_g(t)$ as

$$\begin{cases} P_g(t)=P_0\left[\frac{R_0}{R(t)}\right]^{3\gamma} \\ P_0=P_\infty+\frac{2s}{R_0} \end{cases} \tag{3.2}$$

where the term P_0 is the pressure at the undisturbed bubble wall with a radius of R_0 and $\gamma = C_p/C_v$ is the ratio of specific heats of the gas inside the bubble . We can perturb the pressure at the bubble wall by introduction of sinusoidal waves with a pressure amplitude of P_a and frequency of f. Therefore, we can rewrite $P_\infty(t)$ as

$$P_\infty(t) = P_{\text{amb}} + P_a \sin(2\pi f t) \qquad (3.3)$$

where P_{amb} represents undisturbed ambient pressure in the liquid. Adding the backscattered pressures from neighboring bubbles using Eq. 2.56, we can rewrite the Keller-Miksis equation for a cluster of bubbles in an infinite domain of liquid as

$$\begin{cases} \left[1 - \frac{\dot{R}_i}{c}\right] R_i \ddot{R}_i + \frac{3}{2}\left[1 - \frac{\dot{R}_i}{3c}\right] \dot{R}_i^2 = \frac{P_B(R_i, \dot{R}_i, t)}{\rho} - \sum_{\substack{j=1 \\ j \neq i}}^{N} \frac{R_j}{d_{ij}} \left(R_j \ddot{R}_j + 2\dot{R}_j^2\right) \\ P_B(R_i, \dot{R}_i, t) = \left(P_\infty + \frac{2\sigma}{R_0}\right)\left(\frac{R_{i0}}{R_i}\right)^{3\gamma} - \frac{4\mu \dot{R}_i}{R_i} - \frac{2\sigma}{R_i} - P_{\text{amb}} - P_a \sin(2\pi f t) \end{cases}, \quad i = 1,2,\dots,N \qquad (3.3)$$

Where R_i, $\dot{R}_i$ and $\ddot{R}_i$ respectively represent the instantaneous radius, wall velocity and wall acceleration of each bubble. d_{ij} represents the distance between centers of ith and jth bubble. R_{i0} is the initial radius of the ith bubble, σ and μ are respectively surface tension and viscosity of water.

We can expand Eq. 3.3 to get

$$\left[\left(1-\frac{\dot{R}_i}{c}\right)R_i+\frac{4\mu}{\rho c}\right]\ddot{R}_i+\sum_{\substack{j=1\\ j\neq i}}^{N}\frac{R_j^2}{d_{ij}}\ddot{R}_j$$

$$=\left[-\frac{\dot{R}_i^{\,2}}{2}\left(3-\frac{\dot{R}_i}{c}\right)+\frac{1}{\rho}\left(1+\frac{(1-3\gamma)\dot{R}_i}{c}\right)\left(P_\infty+\frac{2\sigma}{R_{i0}}\right)\left(\frac{R_{i0}}{R_i}\right)^{3\gamma}-\frac{2\sigma}{\rho R_i}-\frac{4\mu\dot{R}_i}{\rho R_i}\right.$$

$$\left.-\frac{1}{\rho}\left(1-\frac{\dot{R}_i}{c}\right)(P_\infty+P_a\sin 2\pi ft)-\frac{2\pi f}{\rho c}P_aR_i\cos 2\pi ft\right]-\sum_{\substack{j=1\\ j\neq i}}^{N}\frac{2R_j\dot{R}_j^2}{d_{ij}} \qquad (3.4)$$

Eq. 3.4 is a system of linearly coupled second order ordinary differential equations. The coupling between Eqq. 3.3 and 3.4 is done through the term that represents the summation of all backscattered pressure waves at the location of each bubble. A solution for Eq. 3.4 requires 2N initial conditions (N is the number of the bubbles in the cluster). We can specify the initial conditions as follows. We assume initially, all of the bubbles in the cluster are at rest (no radial velocity) and their initial radii are known. Therefore, we can write

$$\begin{cases}\dot{R}(t=0)=0\\ R_i(t=0)=R_{i0}\end{cases}\qquad i=1,2,\dots,N \qquad (3.5)$$

3.2. Numerical Solutions

3.2.1. Conventional Methods

With the initial conditions defined in Eq. 3.5, we can now treat Eq. 3.4 as an initial value problem for which we can employ Runge-Kutta (45) numerical algorithms to obtain a solution. In order to use Runge-Kutta, first we need to reduce the order of differentiation as follows

$\dot{x}_{2i-1}=x_{2i}$

$$\left[\left(1-\frac{x_{2i}}{c}\right)x_{2i-1}+\frac{4\mu}{\rho c}\right]\dot{x}_{2i}+\sum_{\substack{j=1\\ j\neq i}}^{N}\frac{x_{2j-1}^2}{d_{ij}}\dot{x}_{2j}$$
$$=\left[-\frac{x_{2i}^2}{2}\left(3-\frac{x_{2i}}{c}\right)+\frac{1}{\rho}\left(1+\frac{(1-3\gamma)x_{2i}}{c}\right)\left(P_\infty+\frac{2\sigma}{R_0}\right)\left(\frac{R_{i0}}{x_{2i-1}}\right)^{3\gamma}-\frac{2\sigma}{\rho x_{2i-1}}\right.$$
$$\left.-\frac{4\mu x_{2i}}{\rho x_{2i-1}}-\frac{1}{\rho}\left(1-\frac{x_{2i}}{c}\right)(P_\infty+P_a\sin 2\pi ft)-\frac{2\pi f}{\rho c}P_a x_{2i-1}\cos 2\pi ft\right]$$
$$-\sum_{\substack{j=1\\ j\neq i}}^{N}\frac{2x_{2j-1}x_{2j}^2}{d_{ij}} \qquad (3.6)$$

Where x_{2i-1} and x_{2i} respectively denote instantaneous radius and radial velocity of the ith bubble.

For simplicity, we define A_i as

$$A_i=-\frac{x_{2i}^2}{2}\left(3-\frac{x_{2i}}{c}\right)+\frac{1}{\rho}\left(1+\frac{(1-3\gamma)x_{2i}}{c}\right)\left(P_\infty+\frac{2\sigma}{R_0}\right)\left(\frac{R_{i0}}{x_{2i-1}}\right)^{3\gamma}-\frac{2\sigma}{\rho x_{2i-1}}-\frac{4\mu x_{2i}}{\rho x_{2i-1}}$$
$$-\frac{1}{\rho}\left(1-\frac{x_{2i}}{c}\right)(P_\infty+P_a\sin 2\pi ft)-\frac{2\pi f}{\rho c}P_a x_{2i-1}\cos 2\pi ft \qquad (3.7)$$

And rewrite Eq. 3.6 as

$$\begin{cases}\dot{x}_{2i-1}=x_{2i}\\ \left[\left(1-\frac{x_{2i}}{c}\right)x_{2i-1}+\frac{4\mu}{\rho c}\right]\dot{x}_{2i}+\sum_{\substack{j=1\\ j\neq i}}^{N}\frac{x_{2j-1}^2}{d_{ij}}\dot{x}_{2j}=A_i-\sum_{\substack{j=1\\ j\neq i}}^{N}\frac{2x_{2j-1}x_{2j}^2}{d_{ij}} & i=1,2,\dots,N\end{cases} \qquad (3.8)$$

Next we need algebraic expressions for the highest order of differentiations to use Runge-Kutta. In other words, we need equation 3.8 in form of

$$\begin{cases}\dot{x}_{2i-1}=x_{2i}\\ \dot{x}_{2i}=f(x_{2i-1},x_{2i},t)\end{cases} \quad i=1,2,\dots,N \qquad (3.9)$$

This step is where numerical complexity arises. For a large number of bubbles (>3) the equations become very large, cumbersome and tedious to deal with. For instance, for two bubbles we have

$$\begin{cases} \dot{x}_1 = x_2 \\ \dot{x}_2 = \dfrac{\left[\left(1-\frac{x_2}{c}\right)x_1+\frac{4\mu}{\rho c}\right]\left[A_2-\frac{3}{2}\left(1-\frac{x_4}{3c}\right)x_4^2-\frac{2x_1x_2^2}{d_{21}}\right]-\frac{x_1^2}{d_{21}}\left[A_1-\frac{3}{2}\left(1-\frac{x_2}{3c}\right)x_2^2-\frac{2x_3x_4^2}{d_{12}}\right]}{\left[\left(\left[1-\frac{x_2}{c}\right]x_1+\frac{4\mu}{\rho c}\right)\right]\left[\left(\left[1-\frac{x_4}{c}\right]x_3+\frac{4\mu}{\rho c}\right)\right]-\frac{x_1^2x_4^2}{d_{12}d_{21}}} \\ \dot{x}_3 = x_4 \\ \dot{x}_4 = \dfrac{\left[\left(1-\frac{x_4}{c}\right)x_3+\frac{4\mu}{\rho c}\right]\left[A_1-\frac{3}{2}\left(1-\frac{x_2}{3c}\right)x_2^2-\frac{2x_3x_4^2}{d_{12}}\right]-\frac{x_3^2}{d_{12}}\left[A_2-\frac{3}{2}\left(1-\frac{x_4}{3c}\right)x_4^2-\frac{2x_1x_2^2}{d_{21}}\right]}{\left[\left(\left[1-\frac{x_2}{c}\right]x_1+\frac{4\mu}{\rho c}\right)\right]\left[\left(\left[1-\frac{x_4}{c}\right]x_3+\frac{4\mu}{\rho c}\right)\right]-\frac{x_1^2x_4^2}{d_{12}d_{21}}} \end{cases} \tag{3.10}$$

Equations for three and four bubbles become exponentially large and for more than four bubbles this approach is not practical. For further reference, equations for three and four bubble systems can be found in Appendix-1 and Appendix-2 respectively.

3.2.2. Matrix Methods

we can rewrite the second part of Eq. 3.8 in a matrix format as follows

$$\underbrace{\begin{bmatrix} \left[\left(1-\frac{x_2}{c}\right)x_1+\frac{4\mu}{\rho c}\right] & \frac{x_3^2}{d_{12}} & \dots & \frac{x_{2N-1}^2}{d_{1N}} \\ \frac{x_1^2}{d_{21}} & \left[\left(1-\frac{x_4}{c}\right)x_3+\frac{4\mu}{\rho c}\right] & \dots & \frac{x_{2N-1}^2}{d_{2N}} \\ \vdots & \vdots & \ddots & \vdots \\ \frac{x_1^2}{d_{N1}} & \frac{x_3^2}{d_{N2}} & \dots & \left[\left(1-\frac{x_{2N}}{c}\right)x_{2N-1}+\frac{4\mu}{\rho c}\right] \end{bmatrix}}_{\boldsymbol{\Phi_{N\times N}}} \underbrace{\begin{bmatrix} \dot{x}_2 \\ \dot{x}_4 \\ \vdots \\ \dot{x}_{2N} \end{bmatrix}}_{\boldsymbol{\Gamma_{N\times 1}}} = \underbrace{\begin{bmatrix} A_1-\sum_{\substack{j=1\\ j\neq 1}}^{N}\frac{2x_{2j-1}x_{2j}^2}{d_{1j}} \\ A_2-\sum_{\substack{j=1\\ j\neq 2}}^{N}\frac{2x_{2j-1}x_{2j}^2}{d_{2j}} \\ \vdots \\ A_N-\sum_{\substack{j=1\\ j\neq N}}^{N}\frac{2x_{2j-1}x_{2j}^2}{d_{Nj}} \end{bmatrix}}_{\boldsymbol{\Psi_{N\times 1}}} \quad (3.11)$$

We need to express the solution matrix, $\Gamma_{N\times 1}$ in terms of $\Phi_{N\times N}$ and $\Psi_{N\times 1}$ to be able to utilize them in the Runge-Kutta method. We can simply multiply both sides of Eq. 3.11 by inverse of $\Phi_{N\times N}$ and obtain

$$\Gamma_{N\times 1} = \Phi_{N\times N}^{-1}\ \Psi_{N\times 1} \qquad (3.12)$$

Thus we have

$$\text{[Inverse Matrix Method]} \qquad \begin{cases} \dot{x}_{2i-1} = x_{2i} \\ \dot{x}_{2i} = \Gamma_i \end{cases} \qquad i = 1, \dots, N \qquad (3.13)$$

where Γ_i is the ith line of matrix $\Gamma_{N\times 1}$. Moreover, in order to solve for each $\dot{x}_{2i}$ individually, we can employ Cramer's rule (46). We define $\Omega(k)_{N\times N}$

$$\Omega(k)_{N\times N} = \begin{cases} \left[\left(1-\frac{x_{2i}}{C}\right)x_{2i-1}+\frac{4\mu}{\rho C}\right] & i=j\neq k \\ \frac{x_{2j-1}^2}{d_{ij}} & i\neq j,\ j\neq k \\ A_i-\sum_{\substack{j=1\\ j\neq i}}^{N}\frac{2x_{2j-1}x_{2j}^2}{d_{ij}} & j=k \end{cases} \qquad (3.14)$$

$\Omega(k)_{N\times N}$ is essentially $\Phi_{N\times N}$ where the kth column is replaced with $\Psi_{N\times 1}$. Now, according to Cramer's rule we can write

$$\dot{x}_{2k} = \frac{\det \Omega(\mathrm{k})_{N\times N}}{\det \Phi_{N\times N}} \qquad (3.15)$$

Therefore, we have

$$[\text{Cramer Method}] \qquad \begin{cases} \dot{x}_{2i-1} = x_{2i} \\ x_{2i} = \dfrac{\det \Omega(\mathrm{i})_{N\times N}}{\det \Phi_{N\times N}} \end{cases} \quad i = 1, \dots, N \qquad (3.16)$$

The main advantage of the introduced approaches is their scalability. In conventional methods one needs to rewrite the system of equations and prepare each one separately for any number of bubbles. Moreover, the simplicity of both proposed methods makes them efficient to implement and use. This enables us to solve for the oscillations of a large number of interacting bubbles within a cluster. Numerical solutions of Eqq. 3.13 and 3.16 will provide us with solutions expressed as radius as a function of time and radial velocity as a function of time for each and every individual bubble within the cluster. One of the main limitations of conventional methods is the number of interacting bubbles that can be simulated, which typically is not more than 4 (42) (41) (40). This restriction limits our understanding of the dynamics of polydisperse bubble clusters. As discussed in the first chapter, applications of MBs predominantly involve the use of polydisperse MB clusters. Our understanding of polydisperse MB clusters is limited since the previously available methods were not capable of providing solution for clusters larger than four bubbles. Proposed approaches will enable us to study the dynamics of large polydisperse

clusters efficiently and investigate their behavior in a wide range of control parameters (discussed in detail in Chapter 7).

4. Method Validation

In this chapter, we will compare numerical solutions of the new introduced methods (Eqq. 3.13 and 3.16), with conventional methods for the cases of two, three and four interacting bubbles. As another measure to validate the model accuracy, inter-bubble distances will be increased to large numbers where we expect the effects of inter-bubble interactions to be minimized. At these distances the dynamics of the interacting bubbles should be identical to those of isolated bubbles of equal size. The equations were solved for a series of bubble sizes, ultrasound exposures and spatial formations.

We begin with a case of two MBs of initial radii of 2μm and 3μm excited with 5 cycles of an ultrasound wave with a frequency of 2MHz and pressure amplitude of 300 kPa. Fig. 4.1 shows the radial oscillations of the 2μm MB for three inter-bubble distances of 10μm, 100μm and 1mm. Radial oscillations of the 3μm MB is presented in Fig. 4.2. An excellent agreement is observed between both of the new proposed methods and the conventional method in Figs. 4.1 and 4.2 for the case of two MB. Figs 4.1 and 4.2 show that dynamics of interacting MBs increasingly diverge from their isolated counterparts as inter-bubble distance decreases. Moreover, Figs. 4.1 and 4.2 illustrate that when the inter-bubble distance between MBs is sufficiently large, interaction effects become negligible and interacting MBs oscillate as isolated MBs.

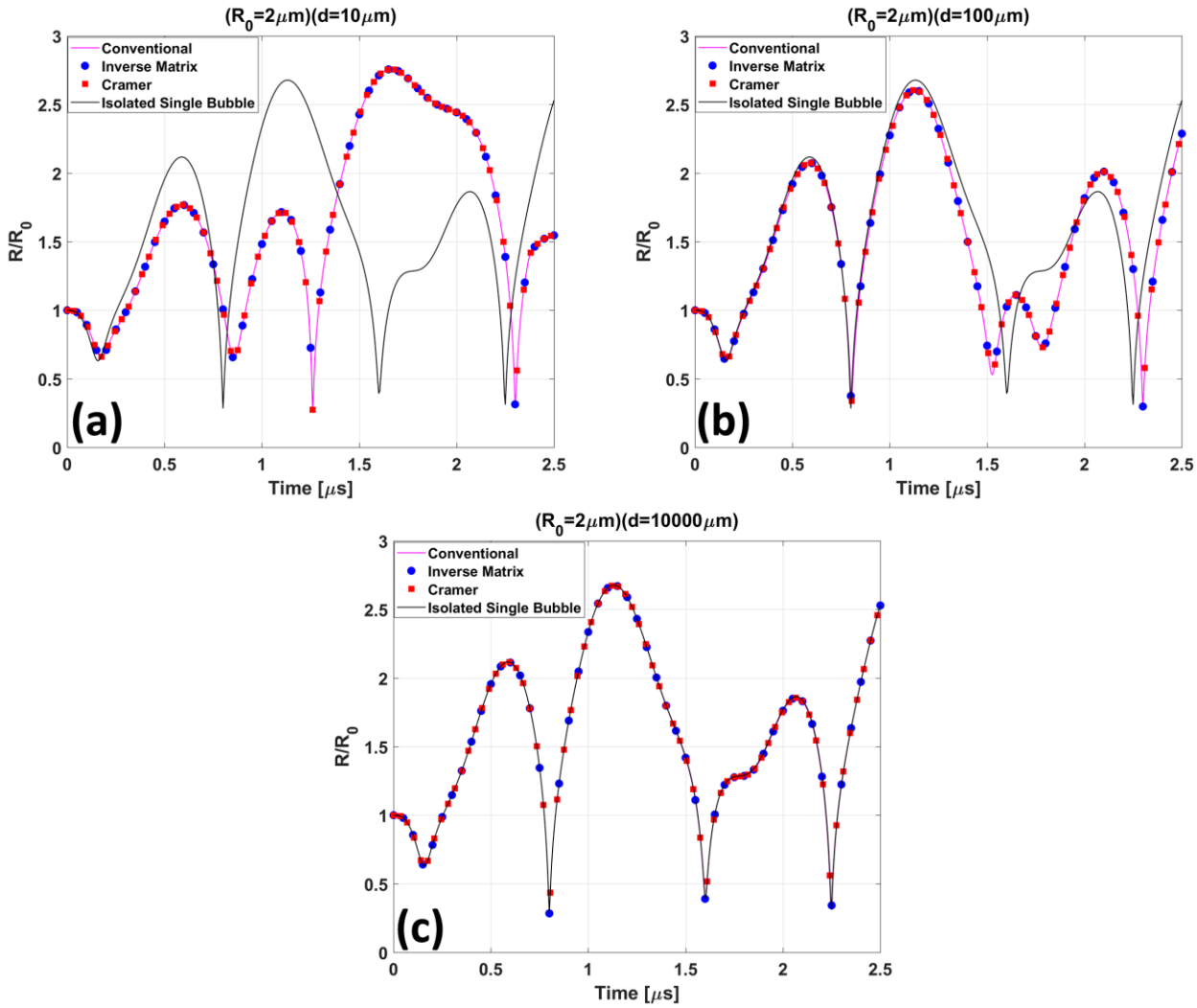

Figure 4.1- Radial oscillations of a MB with initial radius of 2μm in proximity of a MB with initial radius of 3μm inter-bubble distance of (a) 10μm, (b) 100μm and (c) 10000μm sonicated with 5 ultrasound cycles with a frequency of 2MHz and pressure amplitude of 300kPa.

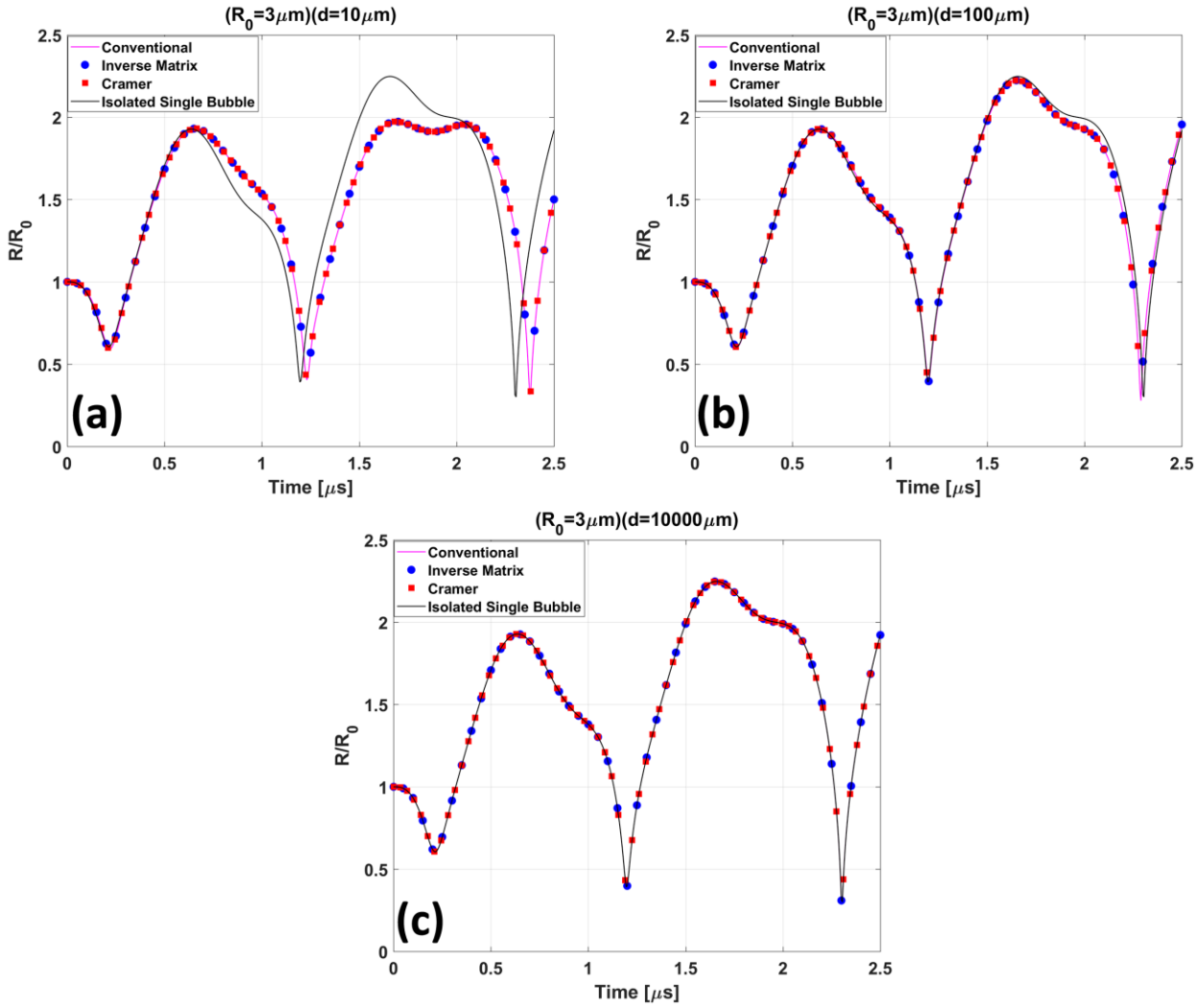

Figure 4.2- Radial oscillations of a MB with initial radius of 2μm in proximity of a MB with initial radius of 3μm with inter-bubble distance of (a) 10μm, (b) 100μm and (c) 10000μm sonicated with 5 ultrasound cycles with a frequency of 2MHz and pressure amplitude of 300kPa

The next set of simulations involve the previous two MBs with the addition of a third MB with an initial radius of 4µm. MBs are placed at the vertices of an equilateral triangle formation shown in Fig. 4.2. Spacing between MBs were set at 10µm, 100µm and 1mm.

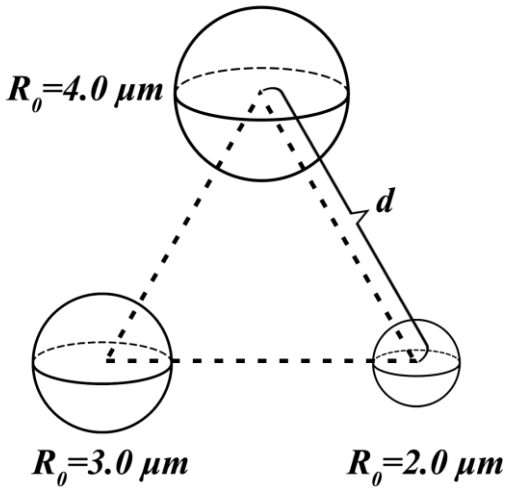

Figure 4.3- Equilateral triangle formation for three-MB case. R_{01} *=2.0µm,* R_{02} *=3.0µm,* R_{03} *=4.0µm*

Figs. 4.4, 4.5 and 4.6 respectively plot the radial oscillations of interacting MBs with initial radii of 2µm, 3µm and 4µm. Results produced by both of the proposed methods are in excellent agreement with the conventional approach for the three bubble case (see Appendix-1). Furthermore, a comparison between oscillations of the isolated counterpart of each bubble (see Figs. 4.4(a)(b), 4.5(a)(b), 4.6(a)(b)) shows a notable change in the radial oscillations of the 2µm, 3µm and 3µm MBs, highlighting the importance of inter-bubble interactions when bubbles are in close proximity. Similar to the case of two MBs (see Figs. 4.1 and 4.2), the results for the three MB case shows as inter-bubble distance decreases, the oscillations of interacting MBs more closely resemble the dynamics of their isolated counterparts (see Figs. 4.4, 4.5 and 4.6)

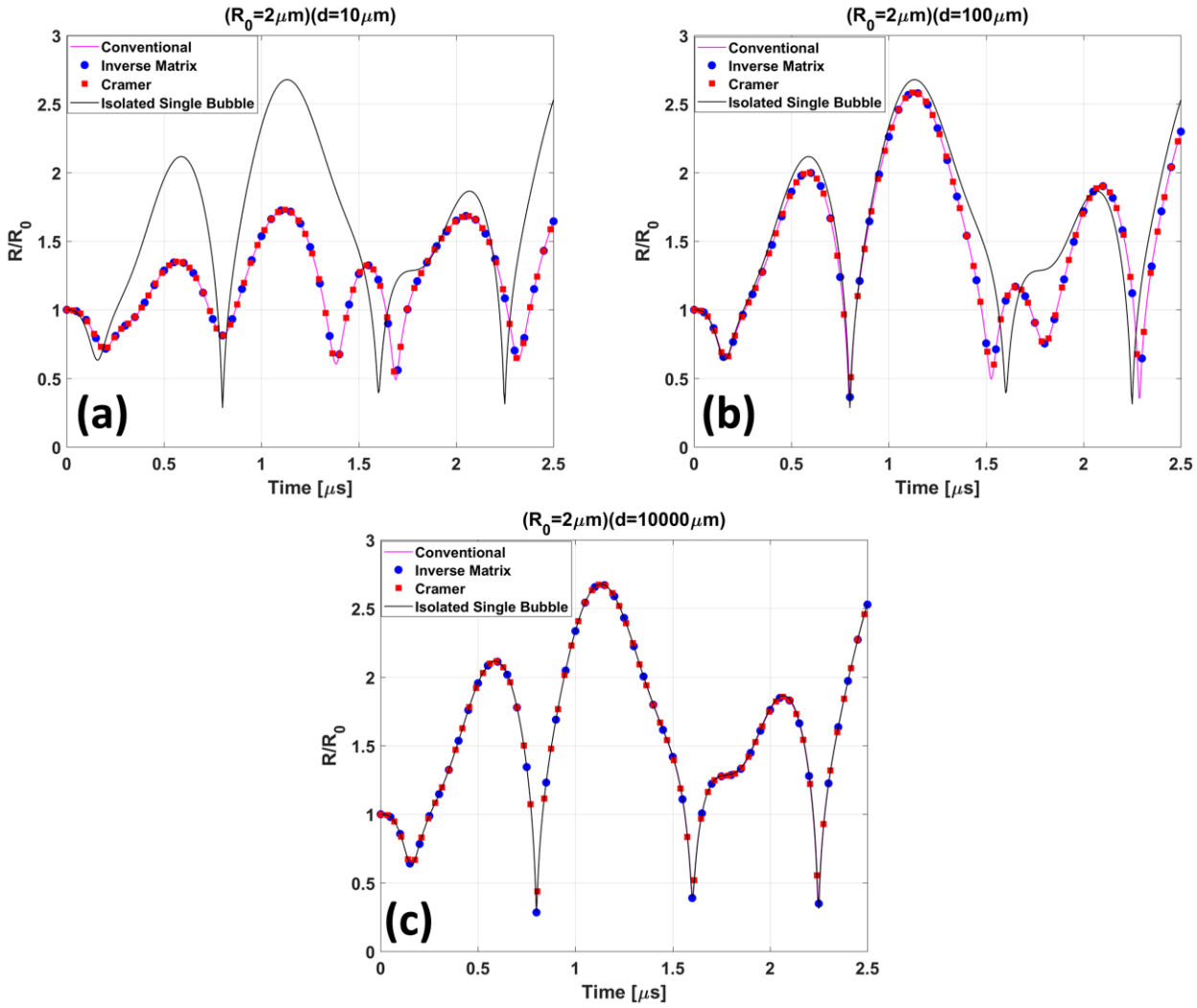

Figure 4.4- Radial oscillations of a MB with initial radius of 2μm in proximity of two MBs with initial radii of 3μm and 4μm with inter-bubble distances of (a) 10μm, (b) 100μm and (c) 10000μm sonicated with 5 ultrasound cycles with a frequency of 2MHz and pressure amplitude of 300kPa

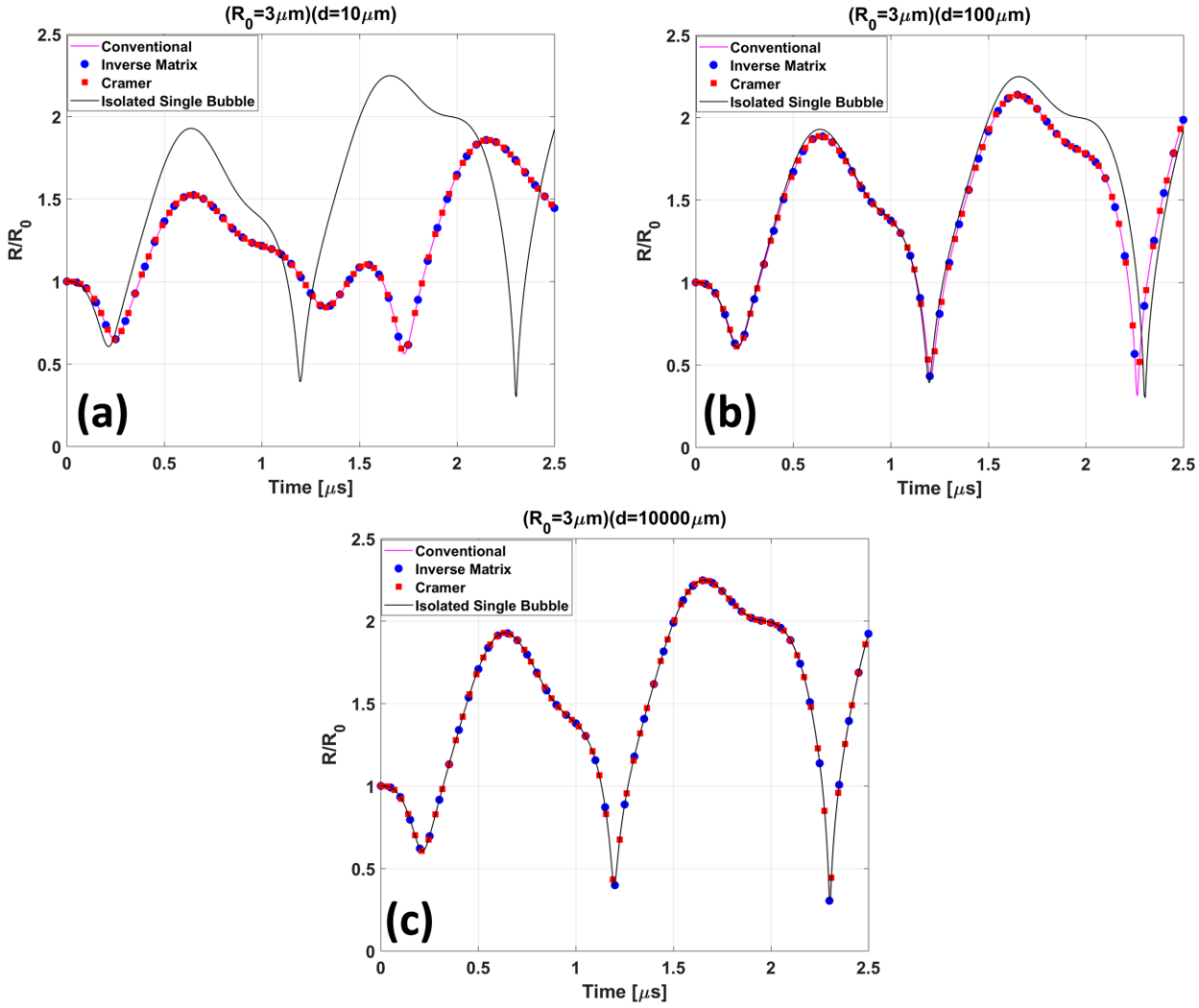

Figure 4.5- Radial oscillations of a MB with initial radius of 3μm in proximity of two MBs with initial radii of 2μm and 4μm with inter-bubble distances of (a) 10μm, (b) 100μm and (c) 10000μm sonicated with 5 ultrasound cycles with a frequency of 2MHz and pressure amplitude of 300kPa

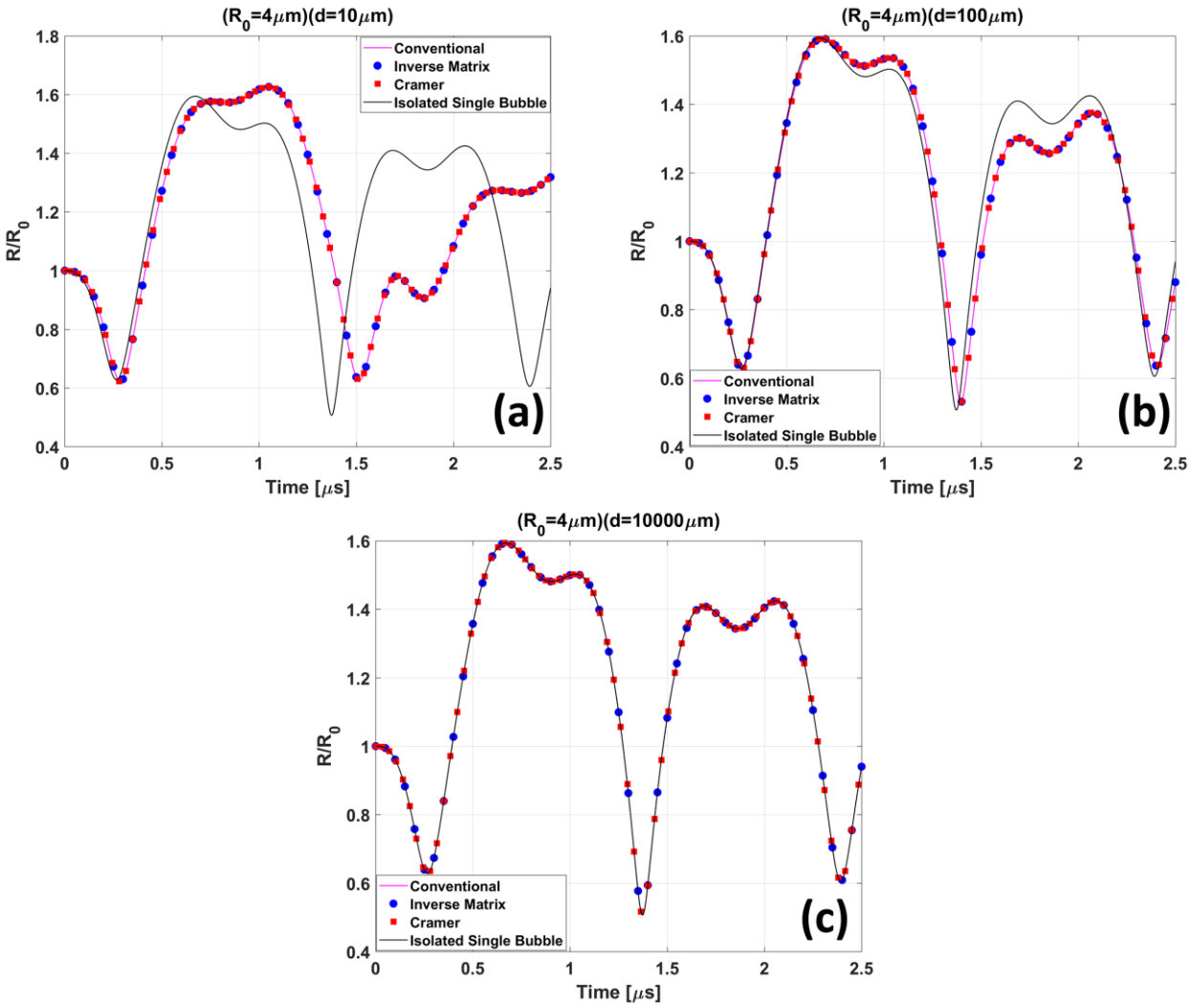

Figure 4.6- Radial oscillations of a MB with initial radius of 4µm in proximity of two MBs with initial radii of 2µm and 3µm with inter-bubble distances of (a) 10µm, (b) 100µm and (c) 10000µm sonicated with 5 ultrasound cycles with a frequency of 2MHz and pressure amplitude of 300kPa

A MB of 5µm radius was added to three-MB configuration presented in Fig. 4.3. The spacing between all of the MBs was kept equal. Hence, the resulting bubbles formed an equilateral tetrahedron (Fig. 4.7). Three tetrahedra were simulated with sides of 10µm, 100µm and 1mm.

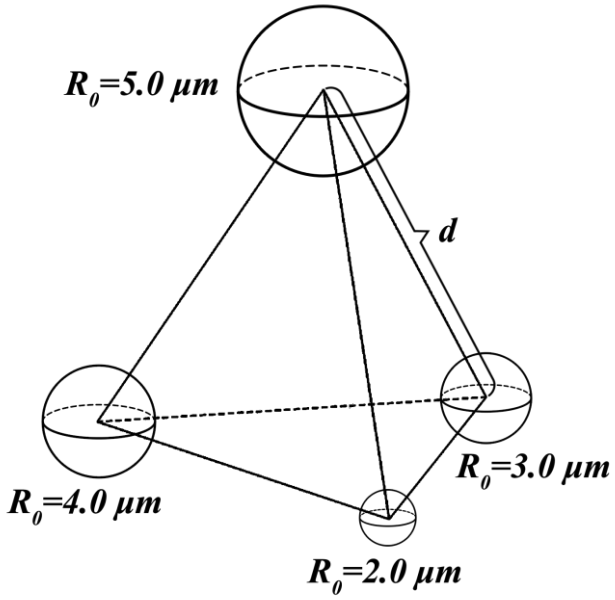

Figure 4.7- Equilateral tetrahedron formation for the 4-MB case. R_{01} *=2.0μm,* R_{02} *=3.0μm,* R_{03} *=4.0μm,* R_{04} *=5.0μm*

Figs. 4.8, 4.9, 4.10 and 4.11 respectively illustrate the radial oscillations of interacting MBs with initial radii of 2μm, 3μm, 4μm and 5μm in configuration presented in Fig. 4.7. MBs were sonicated with an ultrasound wave with a frequency of 3MHz and pressure amplitude of 300kPa for 5 cycles. Radial dynamics from solutions using the conventional method for four bubbles (see Appendix-2) are in excellent agreement with the results generated with proposed Cramer and Inverse Matrix methods. A comparison between Figs 4.4, 4.5 and 4.6 with Figs 4.8, 4.9, 4.10 and 4.11 shows that addition of a fourth bubble to the three-MB cluster changes the oscillations of all of the MBs, again demonstrating the importance of inter-bubble interactions in multi-bubble systems. Results show that when inter-bubble distances are large compared to the size of MBs (spacing > 100μm), dynamics of interacting MBs converge to the dynamics of isolated MBs.

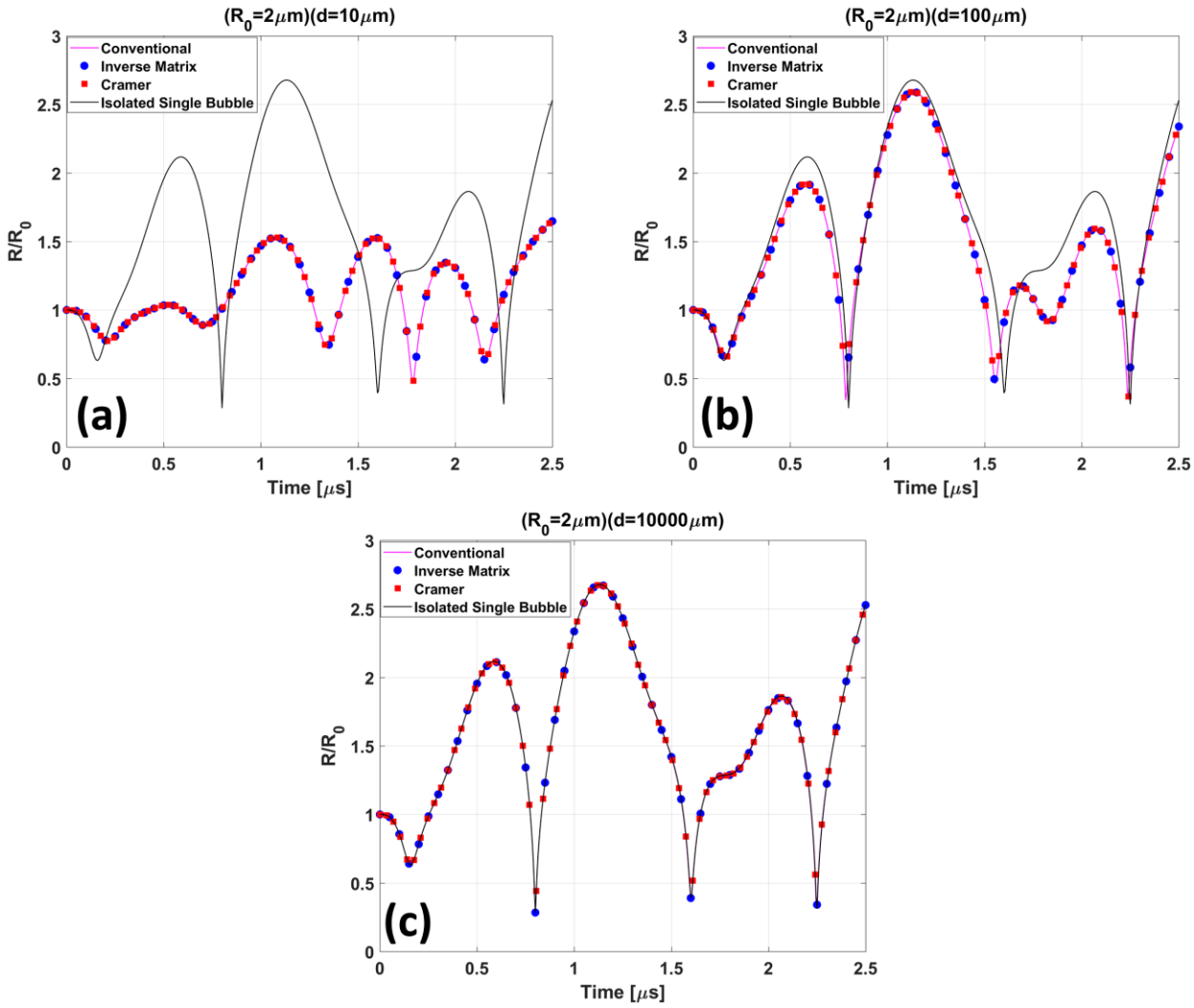

Figure 4.8- Radial oscillations of a MB with initial radius of 2μm in proximity of three MBs with initial radii of 3μm, 4μm and 5μm with inter-bubble distances of (a) 10μm, (b) 100μm and (c) 10000μm sonicated with 5 ultrasound cycles with a frequency of 2MHz and pressure amplitude of 300kPa

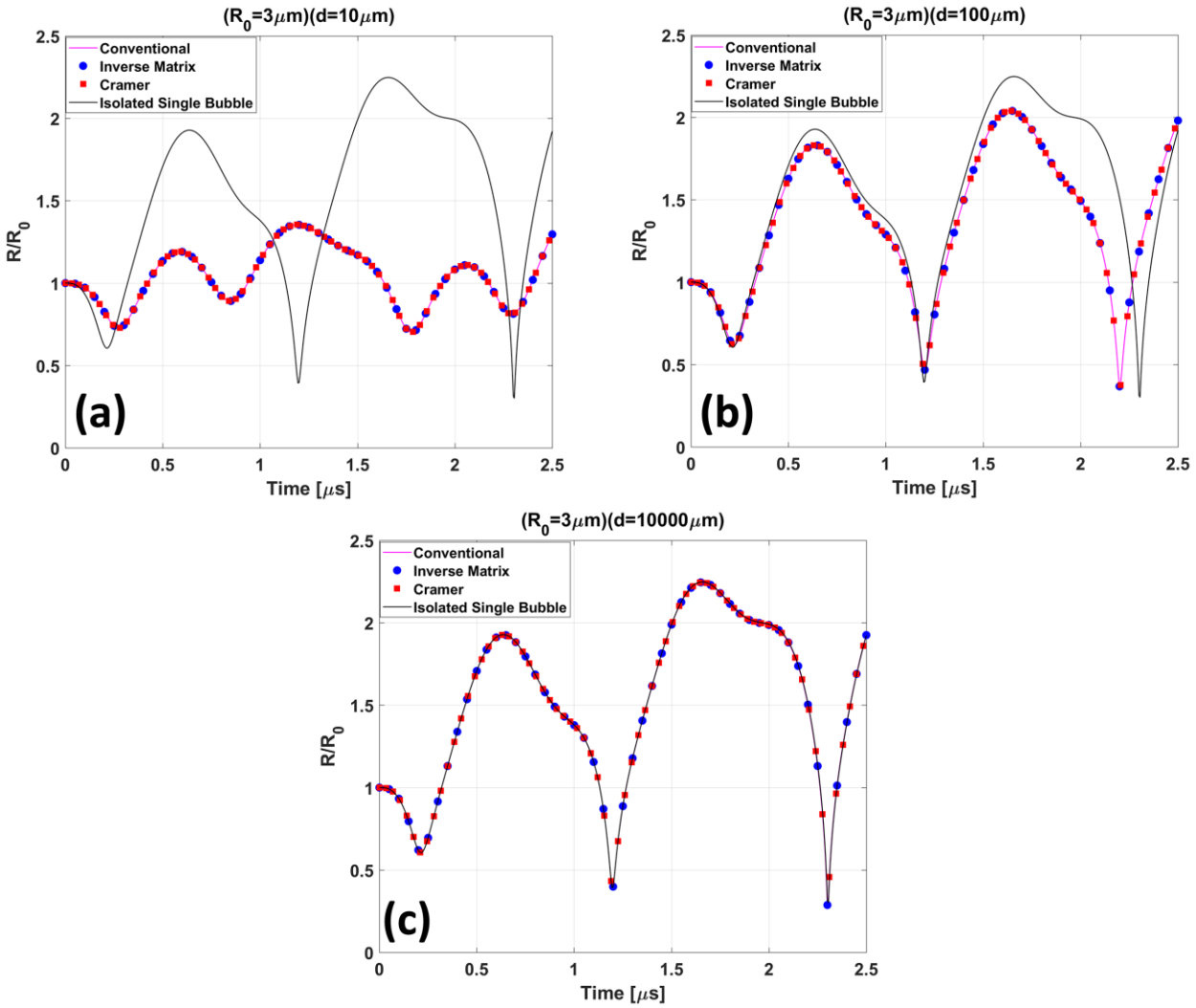

Figure 4.9- Radial oscillations of a MB with initial radius of 3μm in proximity of three MBs with initial radii of 2μm, 4μm and 5μm with inter-bubble distances of (a) 10μm, (b) 100μm and (c) 10000μm sonicated with 5 ultrasound cycles with a frequency of 2MHz and pressure amplitude of 300kPa

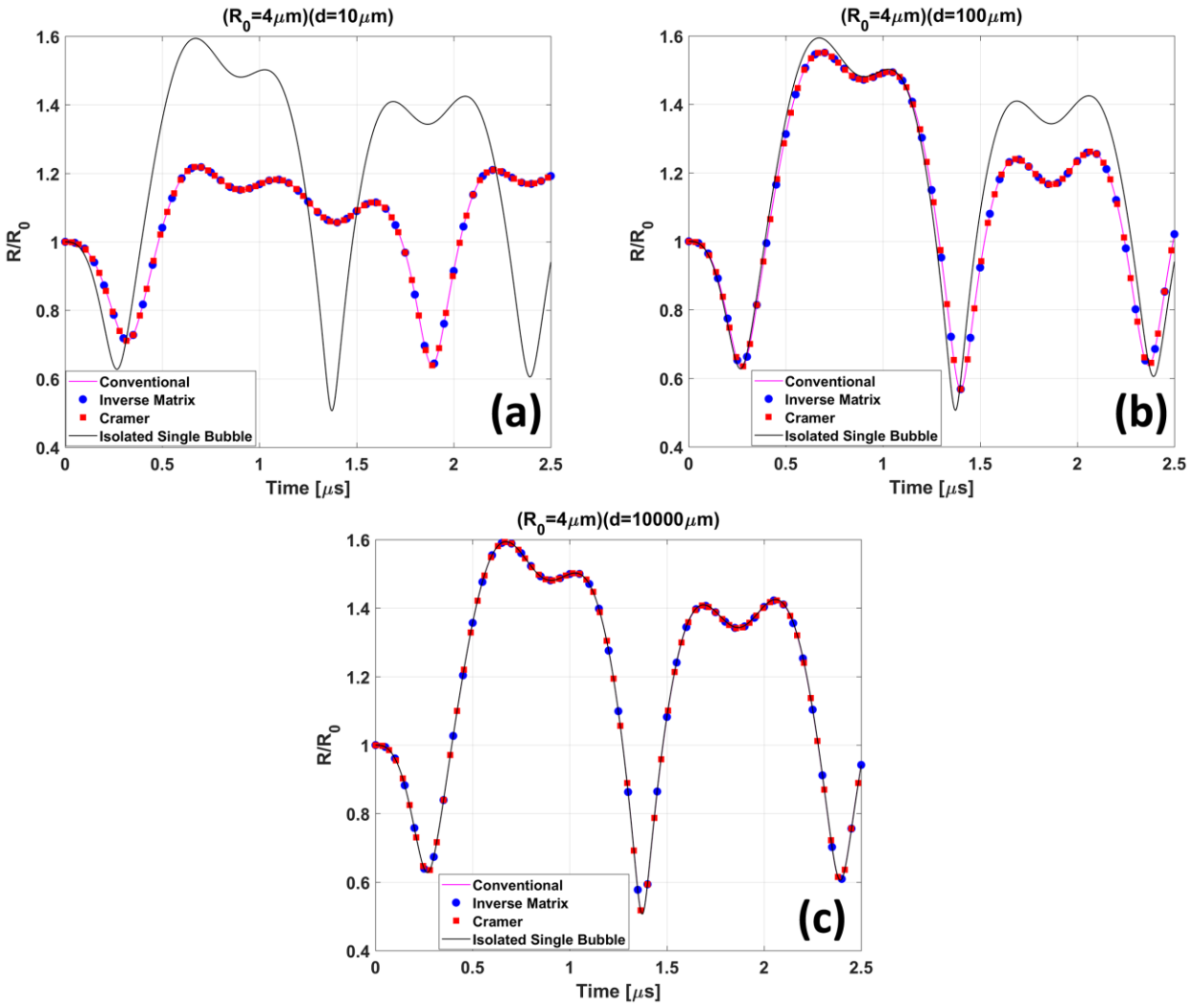

Figure 4.10- Radial oscillations of a MB with initial radius of 4μm in proximity of three MBs with initial radii of 2μm, 3μm and 5μm with inter-bubble distances of (a) 10μm, (b) 100μm and (c) 10000μm sonicated with 5 ultrasound cycles with a frequency of 2MHz and pressure amplitude of 300kPa

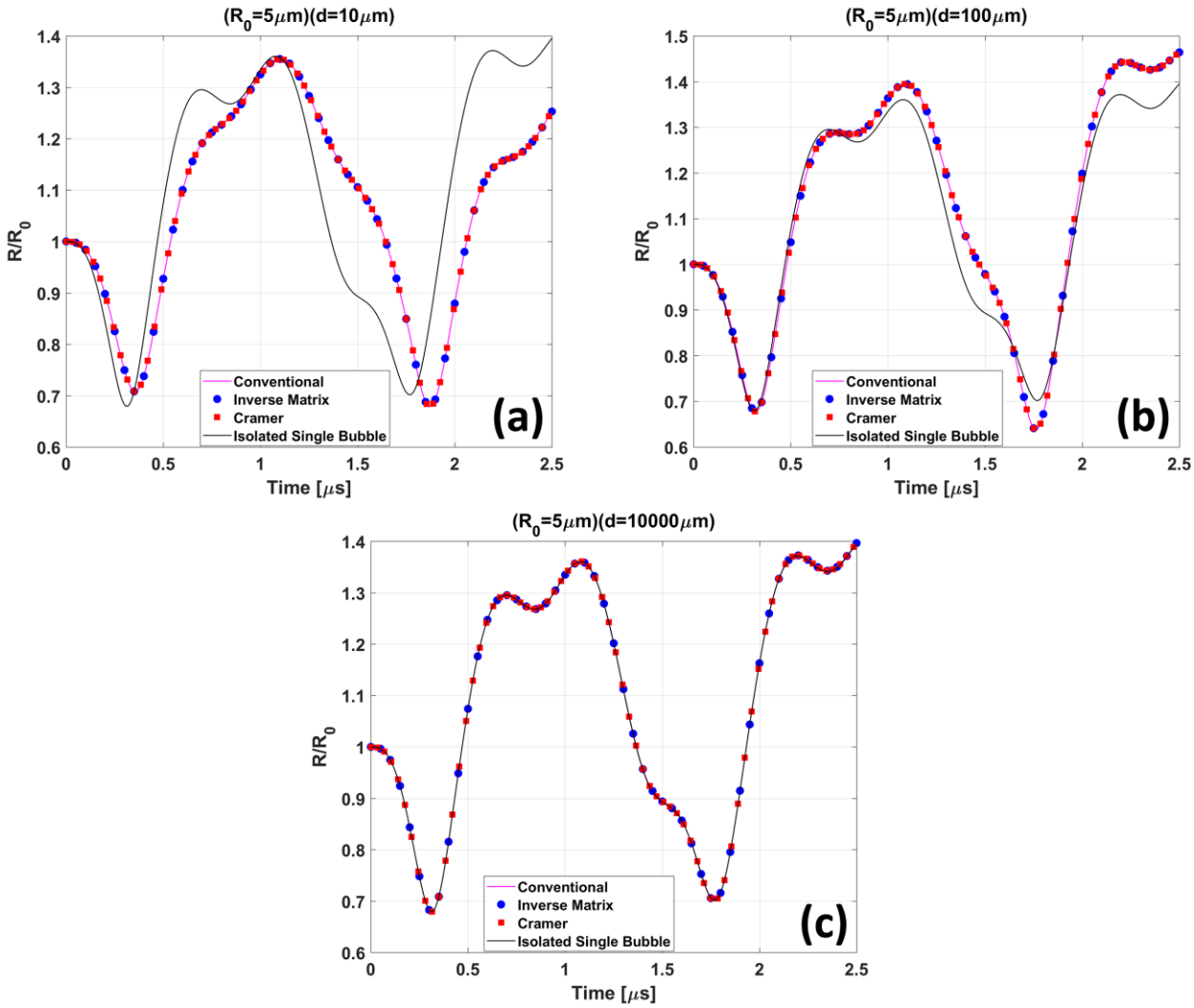

Figure 4.11- Radial oscillations of a MB with initial radius of 5μm in proximity of three MBs with initial radii of 2μm, 3μm and 4μm with inter-bubble distances of (a) 10μm, (b) 100μm and (c) 10000μm sonicated with 5 ultrasound cycles with a frequency of 2MHz and pressure amplitude of 300kPa

Our analysis shows the capabilities of both of the proposed methods to replicate the results of conventional methods while maintaining a degree of simplicity. Both of the methods enable the user to use arbitrary number of bubbles. In previous approaches, separate analytical expressions had to be derived for each bubble coupling. The complexity of the solution to the coupled equations of multiple interacting bubbles were simplified with rewriting the equations in matrix form. This enabled efficient numerical solutions to be implemented.

5. Numerical Analysis Techniques

Since analytical expressions are not available for Eqq. 3.13 and 3.16, to analyze the effect of each parameter, we need to investigate large datasets of numerical solutions where all of the parameters are kept constant except the one we are interested in. Numerical solutions of Eqq 3.13 and 3.16 consist of times series of the radius and wall velocity of each of the simulated bubbles. Bifurcation and frequency response analysis are employed to analyze the numerical solutions.

5.1. Bifurcation Analysis

Lauterborn is one of the firsts to use methods of nonlinear physics to investigate the complex dynamics of acoustically driven MBs (47) (16) (12). Stroboscopic maps, based on mapping the radius of a MB after each forcing period has been used extensively by researchers to evaluate the dynamics of MBs. After the dynamic system reaches its steady state, the radii of the MBs are sampled and plotted in a Poincare plot as a function of the controlling parameter. The procedure continues by increasing the controlling parameter and obtaining a new set of points to be plotted against the control parameter. For instance, consider a MB with an initial radius of 2μm sonicated with ultrasound waves with a frequency of 2MHz and pressures ranging from 1kPa up to 400kPa. If we look at the radial oscillations of the bubble at lower pressures, a trend similar to that of the Fig. 5.1(a) can be observed. Sampling of points (see red dots) after every period and plotting them as a function of the control parameter (pressure in this example) results in a single point as shown in Fig. 5.1(d). For pressures up to 210 kPa in this example, the points cluster in a region of the graph we label period-1 (P-1). After a certain pressure

threshold, further increasing the pressure forces the MB to radially oscillate with different dynamics, similar to the ones presented in Fig. 5.1(b). Sampling points after every forcing period and plotting them as a function of pressure results in two discrete points depicted in Fig. 5.1(d), and the points cluster in region of the graph we define as period-2 (P-2). Further increasing the pressure may result in chaotic oscillations illustrated in Fig. 5.1(c). In this instance, sampling of points does not result in any trend as observed at the lower pressure exposures. Plotting the sampled points as a function of the control parameter in this case results in the region we label as Chaos (Fig. 5.1(d)).

Similar analysis can be done with any other control parameter in the study (e.g. frequency). In this case, all of the other control parameters (e.g. pressure) are kept constant. This allows the investigation of the changes of the MB oscillations as a function of one of the control parameters.

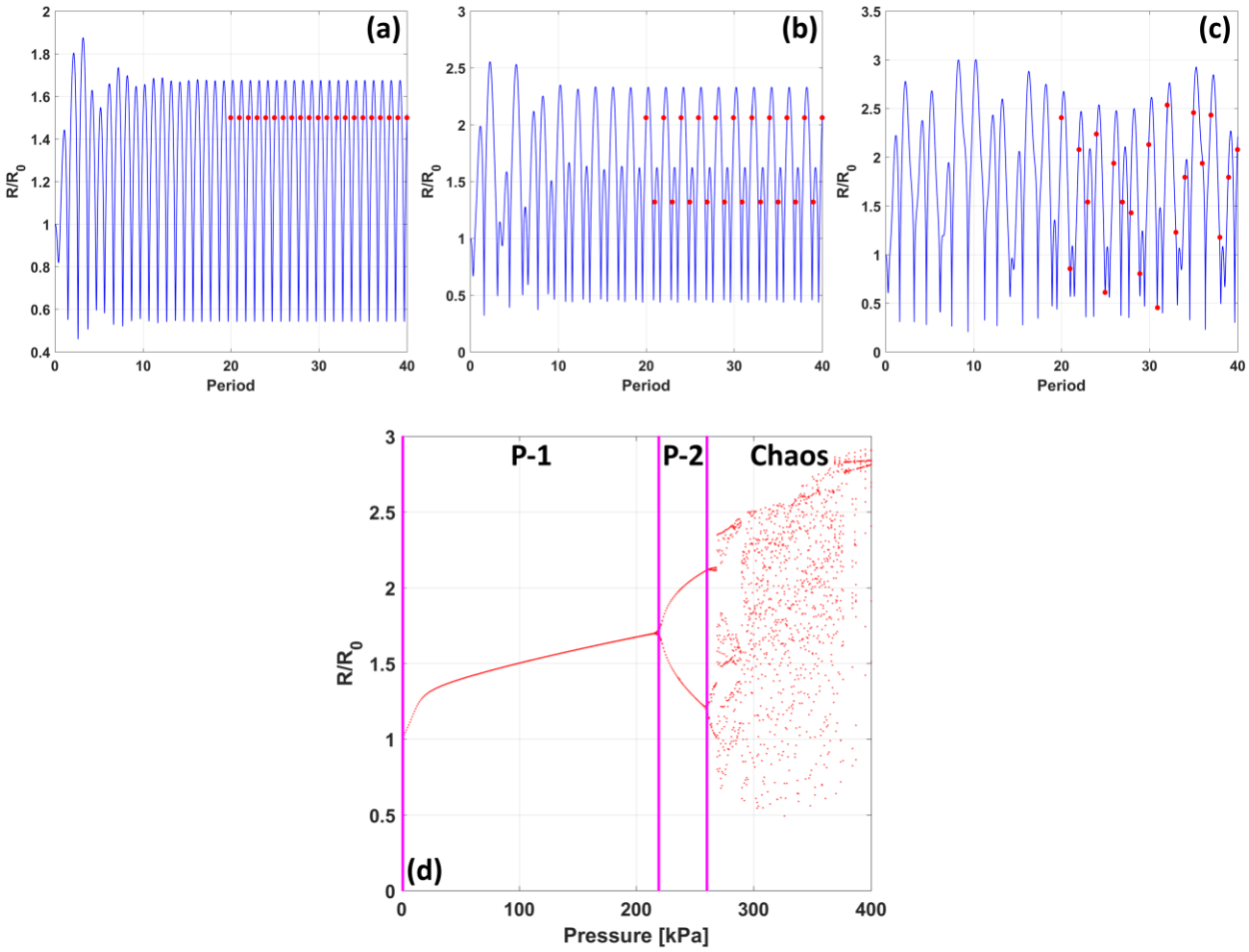

Figure 5.1- Radial Oscillations of a 2μm MB excited with an ultrasound wave of 2MHz (a) Period-1 oscillation (Pa=100kPa), (b) Period-2 oscillations (Pa=250kPa), Chaotic oscillations (Pa=350kPa). (d) Pressure dependent bifurcation diagram of a 2μm MB excited with an ultrasound wave with a frequency of 2MHz.

5.2. Frequency Response Analysis

Frequency response graphs plot the maximum of radial oscillations of a MB at a fixed pressure. They are generated through the following steps

- Radial oscillations of a MB are generated using a large number of ultrasound periods (e.g. 40)of fixed pressure amplitude between two frequencies of f_{min} and f_{max} with steps of f_{step}.
- The steady state portion of the radial oscillation graphs (typically the second half) are selected for all of the frequencies selected (of f_{min} and f_{max})
- The maximum R/R_0 within each selected window is plotted as a function of frequency in a separate graph

Fig. 5.2 illustrates this process for a 2μm MB excited at 1 kPa. In this case the normalized oscillations do not extend beyond 5% of the initial radius and the MB oscillations are linear. The frequency of the maximum in Fig. 5.2(d), in which the radial oscillations are maximized, is the linear resonance frequency F_r of the oscillation.

Increasing the pressure further will result in formation of secondary peaks (resonances) in the frequency response graphs. These secondary peaks are referred to as nonlinear pressure dependent resonances (47).

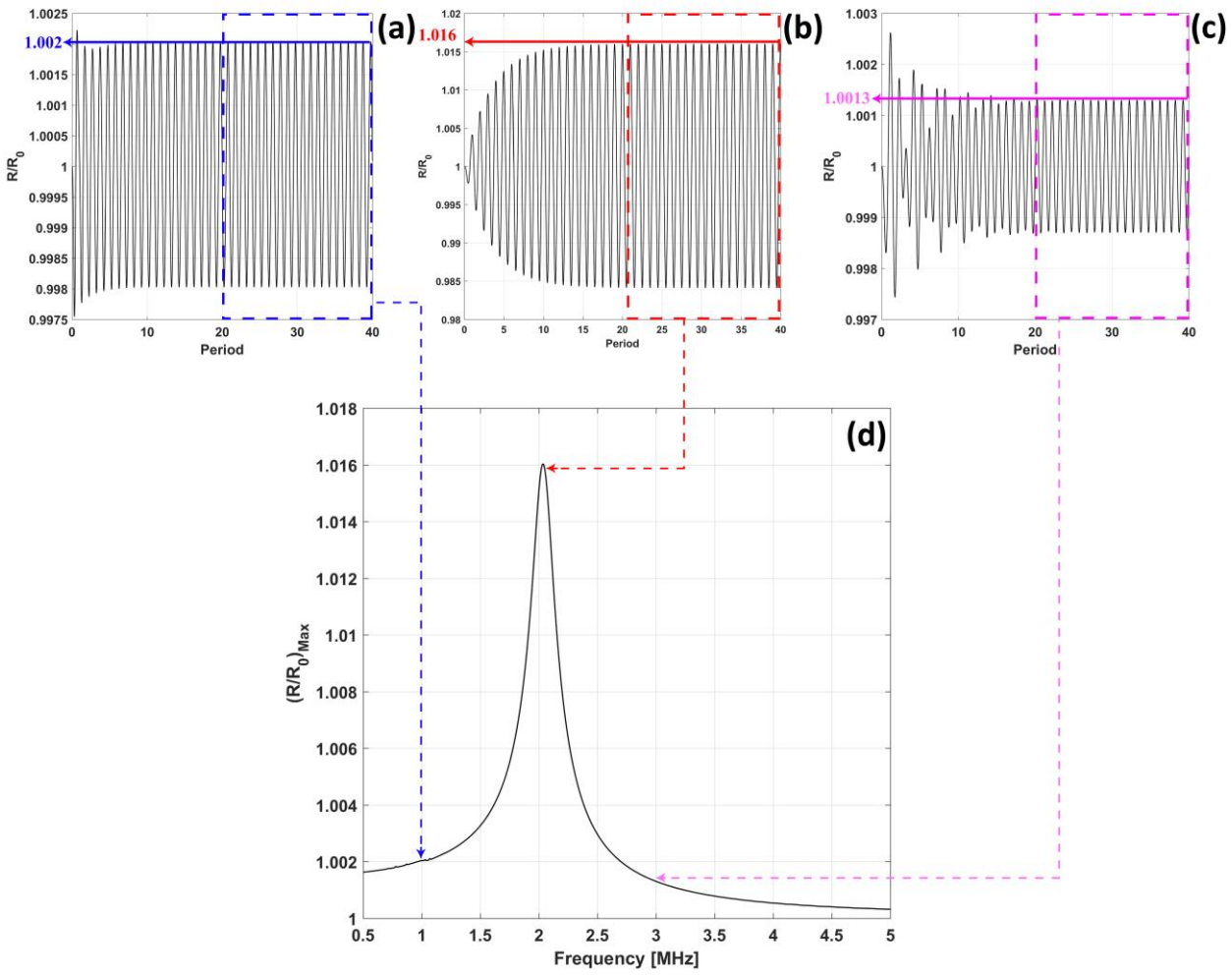

Figure 5.2- Radial Oscillations of a 2µm MB excited with an ultrasound wave of 1kPa amplitude (a) below resonance oscillation (f= 1MHz), (b) Resonant oscillations (f=2.04 MHz), (c) Above Resonance oscillation (f= 3MHz). (d) Frequency response graph of a 2µm MB excited with an ultrasound wave of 1kPa

6. Collective Behavior of Interacting MBs

In this Chapter the effects of inter-bubble interactions in a polydisperse MB cluster are investigated. Takahira et al (1995) have shown that independent oscillations of MBs are suppressed due to inter-bubble interactions when the MBs are in close proximity. This results in a collective behavior within a MB cluster (42). Furthermore, Retkute et al. (2010) have shown that inter-bubble interactions can increase the maximum radius of MB oscillations, resulting in a subharmonic response from MBs at lower frequencies (41). The results presented in this Chapter explain previously observed effects and enables us to predict collective behavior within a MB cluster. Moreover, suppression of radial oscillations is observed and described.

Oscillations of individual interacting MBs under ultrasonic excitation within a cluster is analyzed through numerical solutions for the presented approach (Inverse matrix method is going to be used for our analysis since it is faster in simulations). The simulations are based on various scenarios including a wide range of ultrasonic parameters and MB spatial formations. Spatial formations of equilateral triangle (3-MB cases) and equilateral tetrahedron (4-MB cases) were used to form the geometry of the cluster. Numerical solutions are analyzed via techniques adapted from nonlinear dynamics such as resonance analysis. Pressure dependent frequency response curves, frequency and distance dependent bifurcation diagrams were employed to examine the numerical solutions.

6.1. Resonance Formation, Enhancement and Suppression

Here we are aiming to examine the contribution of smaller and larger MBs to the overall collective behavior of a MB cluster using bifurcation analysis. Previous studies (41) (40) have concluded that larger MBs generally have a significant effect on the dynamics of smaller ones. However, the extent of their influence is yet to be addressed. For instance, previous findings do not predict the collective behavior of a bubble in an arbitrary bubble cluster. Moreover, previous findings indicate that larger MBs can enhance the radial oscillation of smaller MBs, however they do not provide specific conditions required for this to occur. Results presented in this chapter not only reinforce previous observations (e.g. emergent collective behavior, influence of large MBs etc.) but they provide a simple yet effective method to predict collective behavior within polydisperse MB clusters. Here we design a set of numerical studies to investigate the interaction of MBs. A set of 3-MB and 4-MB polydisperse clusters are simulated for a range of ultrasonic and geometric arrangements. MBs of initial radii of 0.5μm, 0.8μm, 1.0μm and 1.5μm are chosen to represent a wide range of MB sizes of interest in biomedical applications (48) (49). Since the purpose of this study is to investigate the nonlinear effects of inter-bubble interactions between MBs, secondary nonlinearities such as the enclosing shell (50) (51) for the MBs are not considered here and are a part of future work. To further reduce the problem uncertainty , we chose symmetrical spatial formations ($d_{ij} = d$) for the problem geometry. This constraint limits to a maximum of 4 MBs per cluster. 3-MB clusters are formed by placing MBs on the vertices of an equilateral triangle of side d illustrated in Fig. 6.1(a). Equilateral tetrahedrons of side d illustrated in Fig. 1.3(b) were chosen to form the geometry of the problem for the 4-MB cases. The 3-MB cases are generated with removal of the largest MB

from the 4-MB cluster simulations. This enables us to examine the influence of the largest MB in the cluster. In the 4-MB cluster the largest MB is the one with initial radius of 1.5μm and in the 3-MB configuration the MB with initial radius 1.0μm.

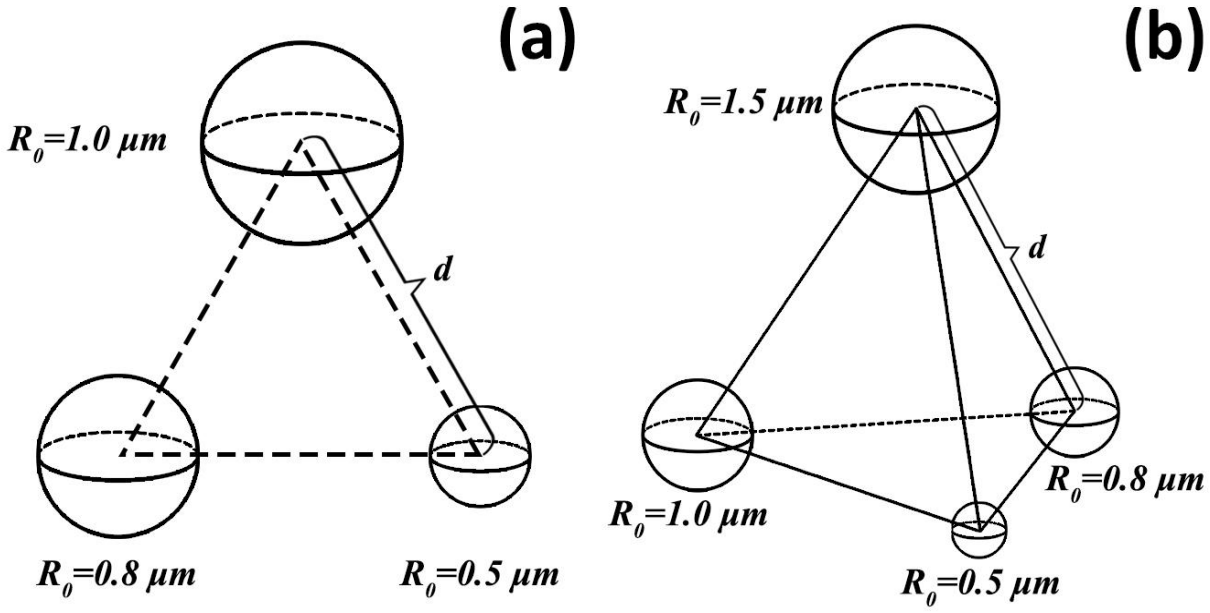

Figure 6.1- (a) equilateral spatial formation for 3-MB case, (b) equilateral tetrahedron formation for 4-MB case

The distances between MBs, d range from 5μm up to 300μm for the largest separation distance. The distances were increased from 5μm up to 20μm in steps of 0.1μm. Beyond d=20μm steps of 0.5μm were applied. The ultrasound frequency ranged from 0.5MHz up to 15 MHz in 2KHz steps with pressure amplitude of 120kPa. A pressure amplitude of 120kPa was chosen since only the largest MB within the cluster exhibits subharmonic resonance behavior in the examined frequency ranges. This parameter set results in 784,080 simulations. The radial oscillation time series were then analyzed using bifurcation and frequency response analysis.

Fig. 6.2(a) illustrates the frequency response of the 4 MB cluster without interaction ($d \to \infty$) and Fig. 6.2(b) depicts the frequency response graph of interacting MBs at a separation distance of 5µm. Removal of the largest MB in the 4 MB cluster results in the frequency response graph shown in Fig. 6.3(c). The MB interaction has significant impact on the MB dynamics which is discussed in the following sections.

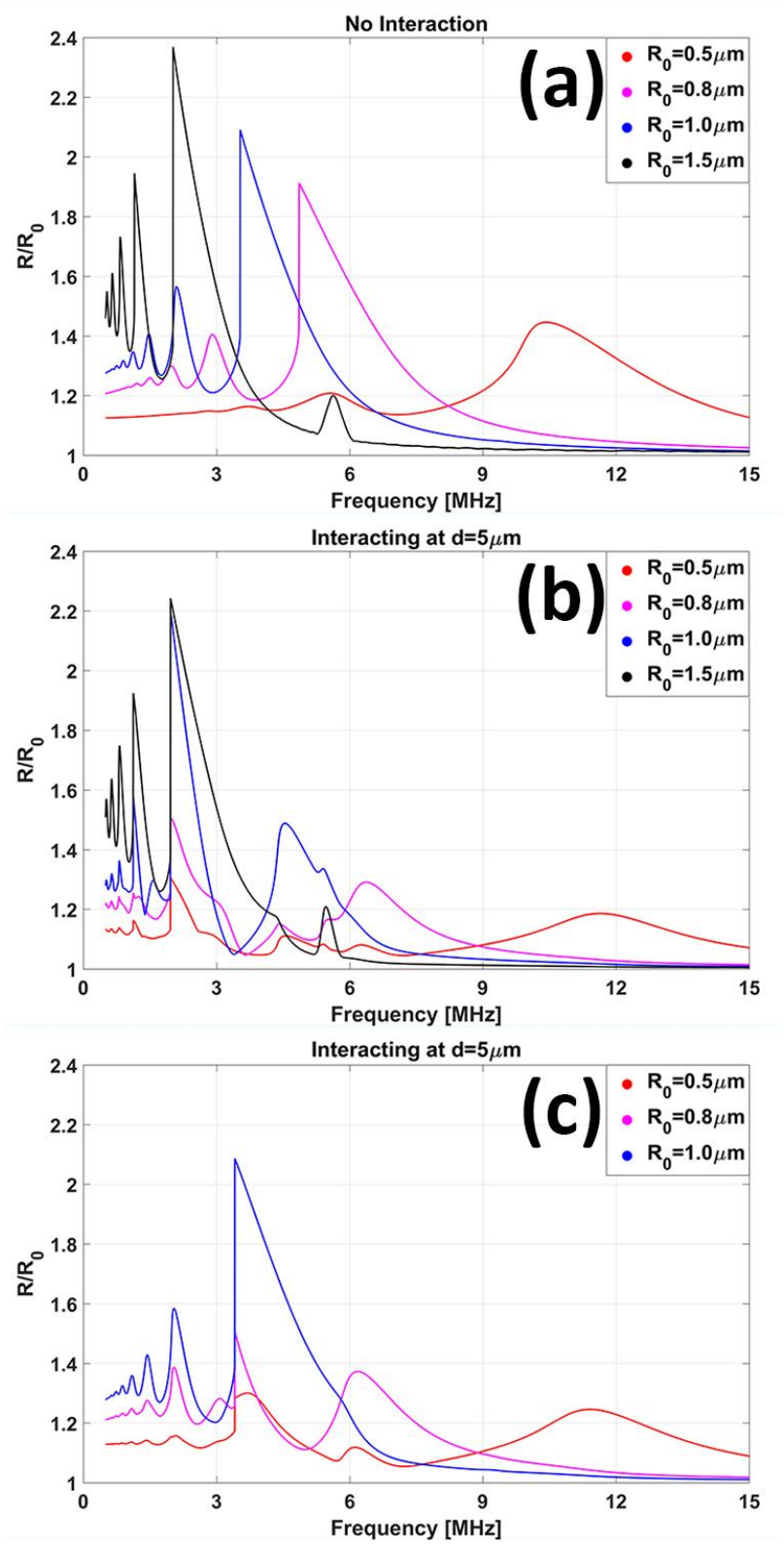

Figure 6.2- Frequency response graphs of 4 non-interacting MBs (a), 4 interacting MBs at d=5μm (b), 3 interacting MBs at d=5μm at a pressure of P_a=120kPa

Figs 6.3(a) and 6.3(b), respectively, show the frequency response diagrams of isolated non-interacting and interacting MBs at a separation distance of 5µm. In Fig. 6.3(a), the 1/1 harmonic resonance peak of the 1.5µm MB is aligned (similar frequencies) with 2/1 order resonance peak of the 1.0µm MB as well as the 3/1 order resonance peak of the 0.8µm MB (resonance naming based on (47)). Moreover, Fig. 6.3(a) shows that 2/1 order resonance mode of the largest MB is aligned with 4/1 order mode of the 1.0µm MB. Furthermore, Fig. 6.3(a) shows that the smallest isolated MB does not have any resonance modes in frequencies lower than 3.5MHz (its 1/1 harmonic resonance mode occurs at approximately 11 MHz (Fig. 6.2(a)).

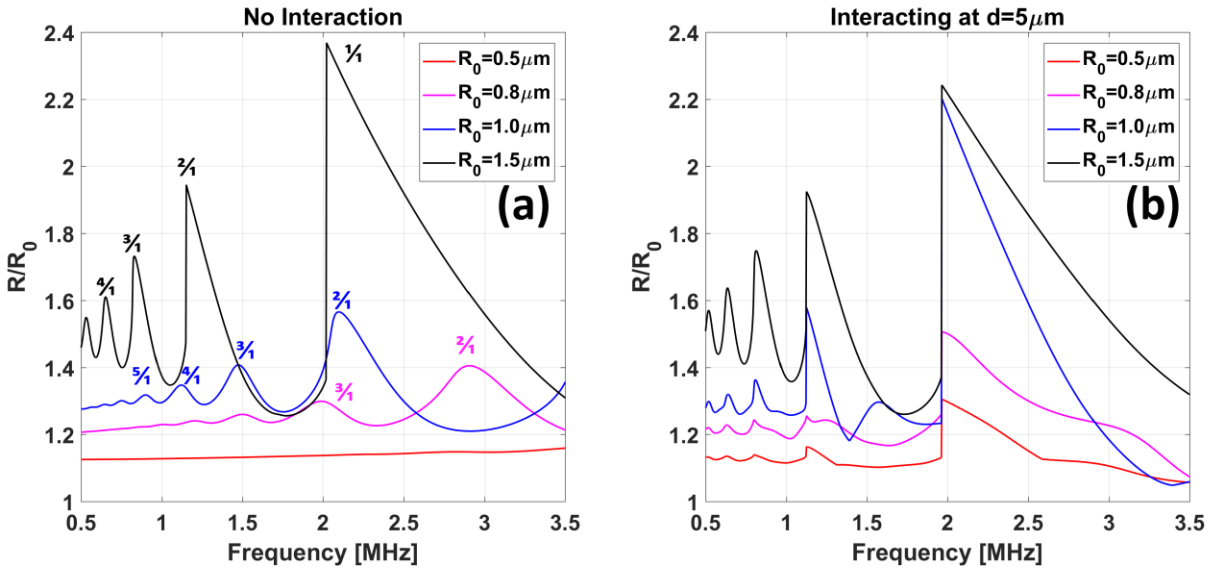

Figure 6.3- Frequency response graph of (a) non-interacting 4-MB cluster (b) Interacting 4-MB cluster at d=5µm using 60 ultrasound cycles of P_a=120kPa

Fig. 6.3(b) shows how the frequency response graphs are modified when the MBs interact (separation 5µm). The figure illustrates a noteworthy enhancement in aligned peaks highlighted in the previous paragraph and also formation of new resonance modes for the 0.5µm MB. There is a negligible weakening (less than 1%) in the resonance amplitudes of the largest MB. Moreover, Fig. 6.3(a) shows that all of the resonance modes of smaller MBs that are

not aligned with any of the resonance modes of the largest MB are suppressed when the MBs are interacting. For instance, the 3/1 order resonance mode of the 1µm MB and 2/1 order resonance mode of the 0.8µm MB in Fig. 6.3(a), as well as the 1/1 harmonic resonance mode of the 0.5µm MB, are suppressed notably when MBs are interacting (Fig. 6.2).

The resonance analysis is then repeated when the largest MB (R_0=1.5µm) from the 4 MB cluster is removed to form a 3 MB cluster. The resulting frequency response diagrams for the non-interacting and interacting 3 MB clusters are illustrated respectively in Fig. 6.4(a) and Fig. 6.4(b).

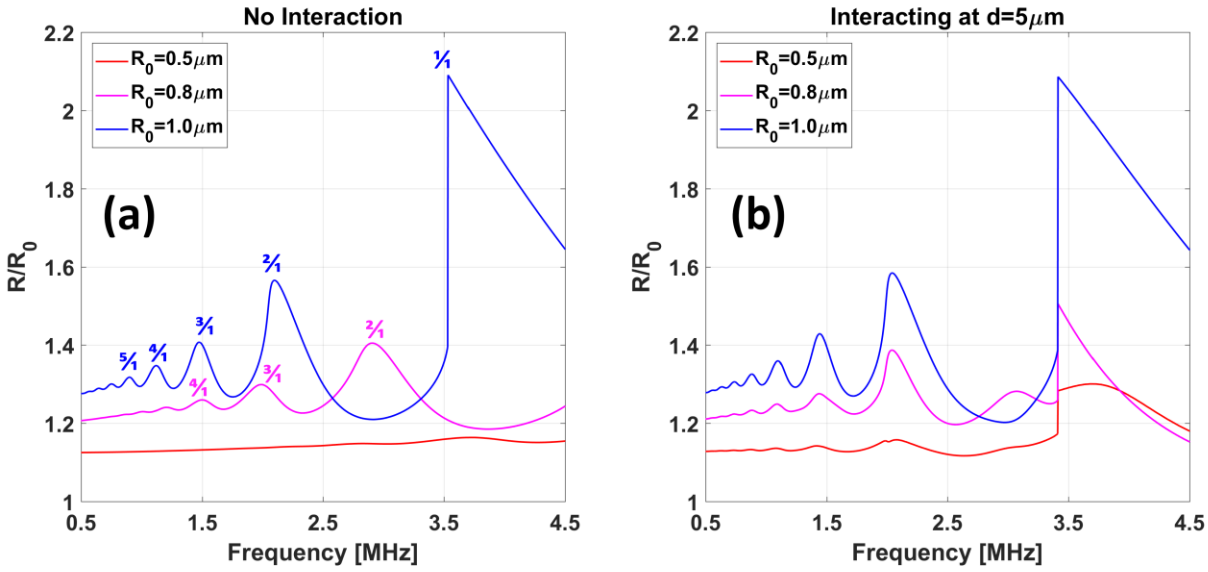

Figure 6.4- Frequency response graph of (a) non-interacting 3-MB cluster (b) Interacting 3-MB cluster at d=5µm using 60 ultrasound cycles of P_a=120kPa

A trend similar to the one observed in the 4-MB case is also present in the 3-MB case. In the 3-MB configuration the largest MB in the cluster has an initial radius of 1µm. Fig. 6.4(a) shows that 3/1 and 4/1 order mode of the 0.8µm MB (which are aligned respectively with 2/1 and 3/1 order modes of the 1.0µm MB) are enhanced in Fig. 6.4(b) when the MBs are interacting.

Moreover, similar to the 4 MB case, Fig. 6.4(a) shows that 2/1 ultraharmonic resonance peak of the 0.8μm MB (not aligned with any of the peaks of the largest MB) is weakened in Fig. 6.4(b) when MBs are interacting. Formation of new peaks due to the interaction are also evident in Fig. 6.4(b), similar to the ones formed under the 1/1 harmonic resonance mode of the largest MB.

6.2. Forced Subharmonic Resonance and Period Doubling

Fig. 6.2(a), illustrates a subharmonic resonance at approximately 5.6MHz in the frequency response of the 1.5μm (largest) isolated MBs. The smaller MBs do not exhibit any subharmonic response in any of the examined ultrasonic frequencies with a pressure amplitude of 120kPa. However, in Fig. 6.2(b) where MBs are interacting at a separation distance of 5μm, all of the MBs exhibit (1/2 subharmonic) resonances at similar frequencies. Furthermore, Fig. 6.2(c) shows removal of the 1.5μm from the cluster eliminates the subharmonic resonance behavior of the smaller MBs. This phenomenon is discussed in more detail in this section with the aid of frequency and distance dependent bifurcation analysis.

Fig. 6.5(a), (b) and (c) shows in greater detail the frequency dependent bifurcation structures of a non-interacting 4 MB cluster, interacting 4 MB cluster (at d=5μm) and an interacting 3 MB cluster (at d=5μm) where the largest MB (R_0=1.5μm) is removed from the cluster. The region between 5-6.2 MHz was chosen. In all these simulations the pressure amplitude was set to 120kPa. Fig. 6.5(a) shows that when MBs are not interacting ($d \to \infty$), only the largest MB is capable of exhibiting P-2 oscillations. However, Fig. 6.5(b) demonstrates that when MBs are oscillating in proximity of each other at a separation distance of $5\mu m$, smaller MBs undergo

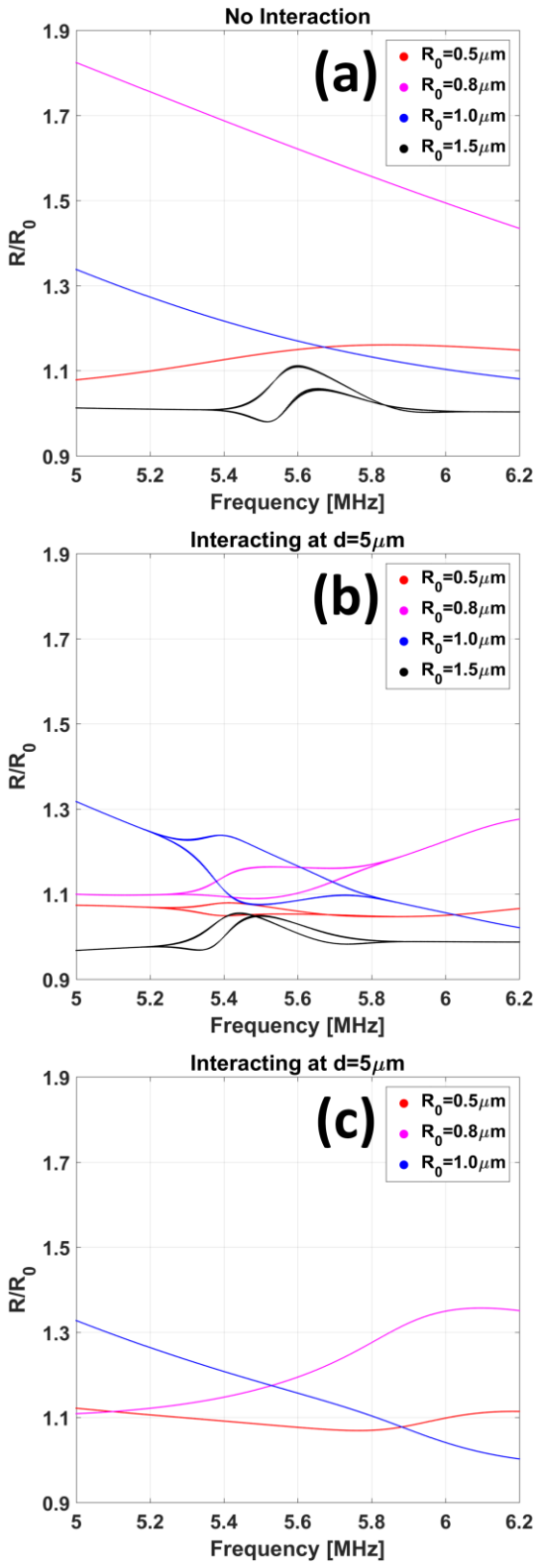

Figure 6.5- Frequency dependent bifurcation structures of non-interacting 4-MBs (a), Interacting 4-MB at $\dot{d}$=5μm (b), interacting 3-MB at $\dot{d}$=5μm using 60 ultrasound cycles of P_a=120kPa

period doubling as well. Furthermore, Fig. 6.5(c) shows that removal of the 1.5µm MB from the cluster, reverts the oscillations of smaller MBs back to their P-1 mode.

For further investigation of this phenomenon, Fig. 6.6 shows a separation distance dependent bifurcation diagram. Here, the frequency and the pressure amplitude of the ultrasound wave were kept at constants of respectively 5.4MHz and 120kPa and the geometry of the problem was considered as the control parameter. More specifically, the size of the sides of the equilateral tetrahedron illustrated in Fig. 6.1(b) was changed to investigate the influence of inter-bubble distances on forced period doubling.

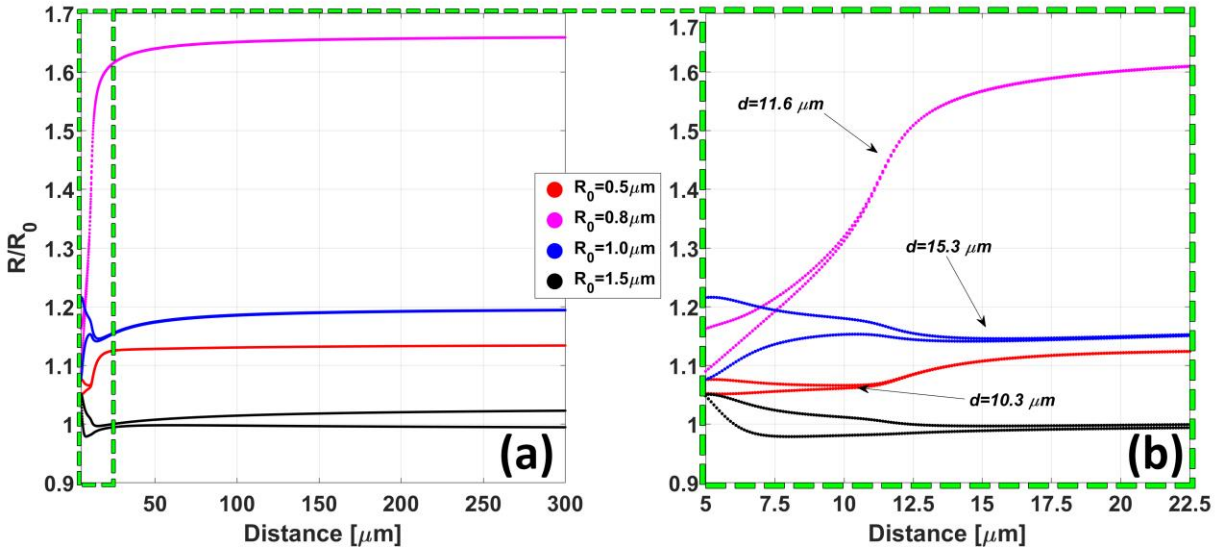

Figure 6.6- Distance dependent bifurcation diagram of the 4-MB cluster excited with an ultrasonic wave [f=5.4 MHz P_a= 120 kPa] (a) d= 5µm - 300µm (b) region zoomed to the subset d= 5µm – 22.5µm

Fig. 6.6 illustrates a distance dependent bifurcation diagram where the ultrasonic frequencies and pressures were kept constant. Fig. 6.6(a) shows that when MBs are sufficiently far apart from each other, none of the smaller MBs undergo period doubling. Fig. 6.6(b) shows that at smaller inter-bubble distances, all of the smaller MBs undergo period doubling. However,

Figure 6.6(b) also shows that the closer the size of a MB to the largest MB, it can be forced into P-2 oscillations at larger separation distances when compared to other MBs of smaller size. The 1.0µm MB was forced into period doubling at a separation distance of 15.3µm when rest of the smaller MB within the cluster were maintaining their P-1 mode. Further shrinking the cluster size results in period doubling of the 0.8µm and 0.5µm MBs at distances of 11.6µm and 10.3µm respectively.

6.3. Classification of Inter-Bubble Interactions

Here, it was shown that interactions of MBs under ultrasonic excitation can be classified into "constructive" and "destructive" interactions. We define constructive interactions as resonance enhancement and formation. It was shown that when the resonance mode of a smaller MB within a cluster is aligned (similar frequency) with a larger MB, it will be enhanced upon interaction under ultrasonic excitation. Furthermore, if smaller MBs do not exhibit any resonance mode in a frequency where a larger MB has a resonance mode, the largest MB can form resonance modes in the frequency response diagram of smaller MBs. Moreover, we define destructive inter-bubble interactions as follows; if a resonance mode of a smaller MB is not aligned with any of the largest MB, it will be weakened in amplitude when they are interacting under ultrasonic excitation. Additionally, it was shown that constructive interactions, followed by formation of secondary resonances in smaller MBs, can force the smaller MBs to change their mode of oscillations completely. For instance, it was shown that the largest MB within the cluster can force smaller MBs to undergo period doubling and force them to change their modes of oscillations from P-1 into P-2. It was shown that the largest MB within the cluster dictates the collective behavior of MBs within the cluster: it can force smaller

MBs to oscillate with similar dynamics. Smaller MBs within the cluster have negligible influence on the dynamics of the largest MB within the cluster. In Eq. 2.56, the backscattered pressure field of each bubble is dependent on its instantaneous radius. Therefore, it is expected that scatter from smaller MBs results in weaker pressure fields that do not significantly perturb the dynamics of larger MBs.

7. Large Bubble Clusters

In the previous chapter, we expanded on previous work (40) (41) (42) and unified their conclusions and our observations under the proposed classification for inter-bubble interactions. In this chapter, we are going to employ the capabilities of our method to investigate the dynamics of large bubble cluster consisting of many (>10) bubbles. Limitations of previous methods simply did not allow us to conduct studies on the inter-bubble interactions on a large scale. Here our results show that some common assumptions are not correct. For instance, the assumption that identical bubbles (e.g. same size, shell composition and etc.) will exhibit similar dynamics under ultrasonic excitation. In this Chapter, I start by introducing the method by which I defined the geometry of the large bubble cluster problem (their spatial locations). Next, I analyze the linear resonance frequency of individual MBs within monodisperse clusters of different concentrations. Moreover, nonlinear dynamics of interacting monodisperse MBs are investigated through frequency response diagrams for multiple bubble concentrations, followed by the analysis of polydisperse clusters (here I only use two sizes) to investigate the extent of constructive and destructive interactions in large bubble clusters.

7.1. Random Spatial Formations

Spatial formations of MBs within a cluster can be described as randomly positioned. To generate the large cluster of MBs, three random numbers between zero and the size of the defined cube are generated and used as Cartesian coordinates for the first bubble within the cube. Next, a second set of random numbers for the second point are generated but its distance from the first point is checked to ensure that bubbles do not collide during oscillations. A minimum distance is defined, and if the generated points are closer than the minimum allowed distance, the coordinates are dismissed and a new set is generated. This process is repeated for every point. The distance between all of the points are checked to ensure they are larger than the minimum allowed distance. Fig. 7.1 shows an example of 50

bubbles within a cube with a side of 400µm. The walls of the generated cube are not considered solid boundaries; the defined cube is essentially a volume within an infinite domain of liquid where bubbles are allowed in.

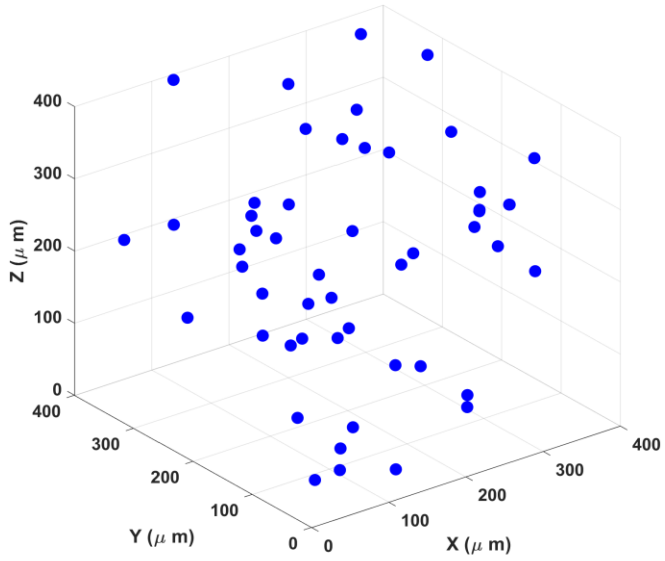

Figure 7.1- Random formation of 50 MBs within a 400µm cube with an allowed minimum distance of 10µm

7.2. Linear Resonance Frequency of Interacting Monodisperse Bubbles

In this section, the linear resonance frequency of large number of MBs within a cluster is analyzed. The effects of different random formations of equal number density MBs on the linear resonance frequency of MBs is examined. Initially, the linear resonance frequencies of each MB within a monodisperse bubble cluster is analyzed to ensure that all the MBs have the same resonance frequencies.

A cube with a side of 300µm is defined. Ten different random formations for each number of bubbles starting from 2 bubbles up to 170 bubbles (in increments of 2) are generated. MBs are chosen to have initial radii of 2µm. Frequency response graphs similar to those of Fig. 5.2(d) are

generated for each MB within the cluster and the peak of each curve is recorded as the linear resonance frequency of each MB within the cluster.

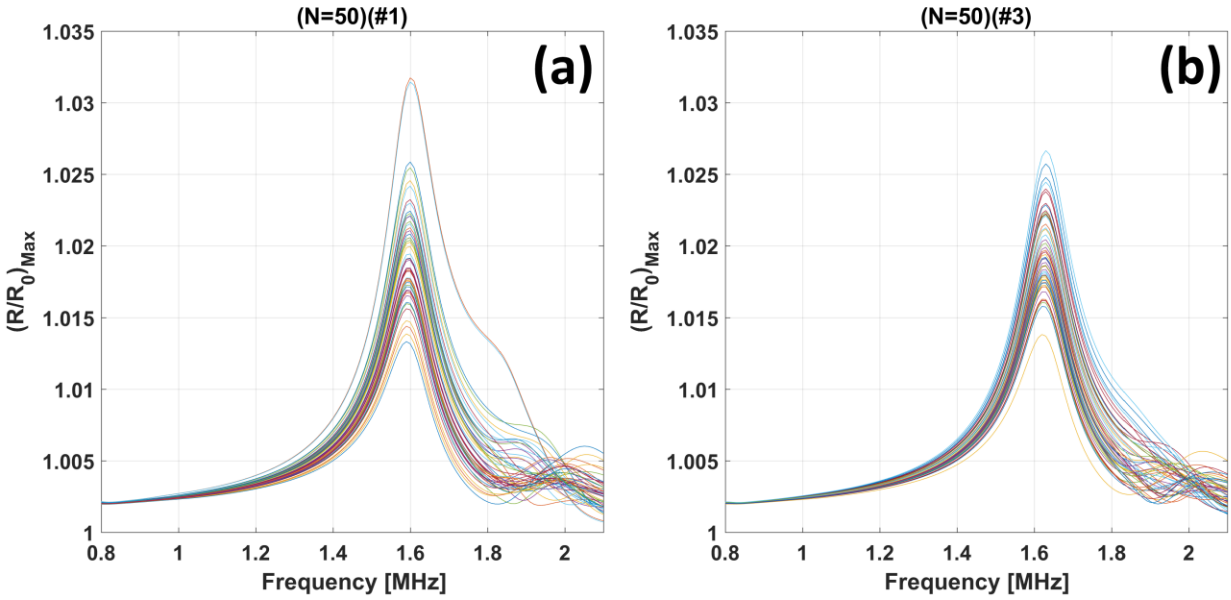

Figure 7.2- Frequency response diagram of 50 MBs (R_0=2μm, P_a=1kPa) randomly placed within a cube with a side of 300μm (a) Random formation #1 (b) Random formation #2

Fig. 7.2 illustrates the frequency response diagram of 50 MBs of initial radii of 2μm. Observations of 850 cases (N=2, 4, …,170 – with 10 random formations for each N) indicate that monodisperse MBs within a cluster have the same linear resonance frequency. The MB linear resonance frequencies in Figure 7.2(a), for one random formation, are also similar for all MBs, even though there appears to be a small deviation of linear resonance frequencies among different random formations (e.g. Fig. 7.2(b)).

Linear resonance frequencies for a range of MB number densities were averaged for 10 random formations and the average and the standard deviations were calculated. The deviation is representative of the differences in resonance frequencies for the different spatial formations.

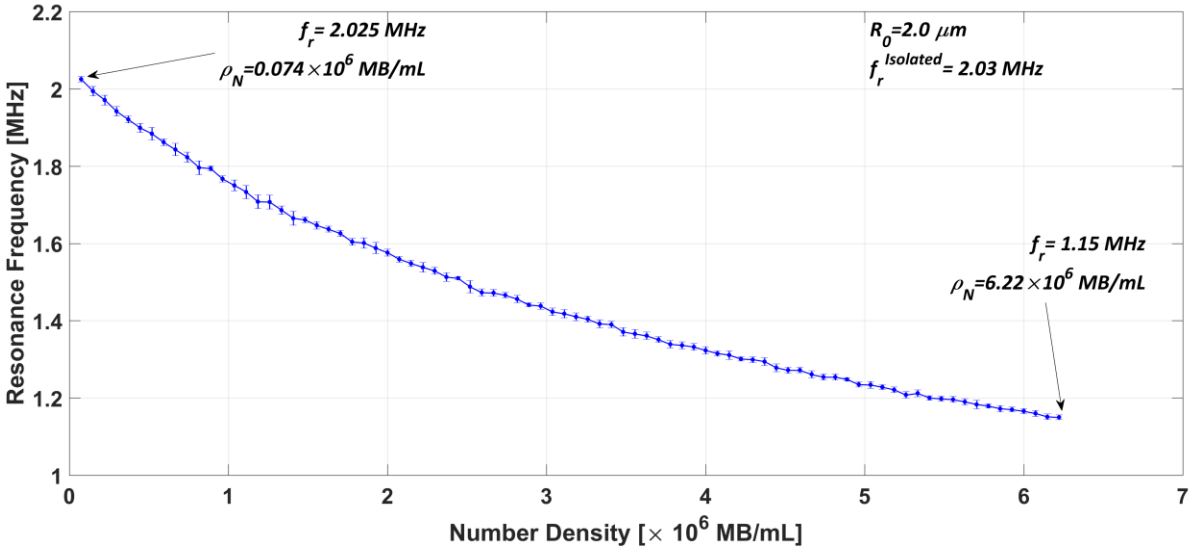

Figure 7.3 – Plot of linear resonance frequency of 2µm MBs as a function of number density, error-bars represent average deviation from average value among 10 different random spatial formations

Fig 7.3 shows the average resonance frequency of monodisperse 2µm MB clusters as a function of number density. The size of the error-bars in Fig. 7.3 demonstrates the fact that the linear resonance frequency of MBs within a monodisperse cluster is minimally dependent on the spatial distribution of the multiple realization of randomly distributed MBs. Practically, the difference is small, so that it can be argued that the linear resonance frequency of MBs is independent of their spatial distribution (for the same number density). Fig. 7.3 also illustrates the dependence of linear resonance frequency of MBs on their number density within a cluster. The higher the MB number density, the lower the linear resonance frequency. For very low number densities (left portion of Fig. 7.3), the MB linear resonance frequency converges to that of an isolated MB. For high number densities, for instance 6 million bubbles per mL, the linear resonance frequency decreases to about 40% compared to that of an isolated MB. Note that these calculations do not take into account the attenuation of the ultrasound beam in the bubbly medium.

7.3. Nonlinear (Pressure Dependent) Resonance Frequency of Monodisperse Bubble Clusters

When isolated MBs are exposed to high pressures (typically > 10 kPa), they oscillate non-linearly. In this section, we examine the pressure dependent resonance frequency of monodisperse bubble clusters. Previous studies have shown the dependence of the resonance frequency of isolated MBs on the pressure amplitude of the acoustic field (47). The resonance frequency of isolated MBs decreases with the increasing pressure amplitude of the ultrasound beam.

In this section numerical simulations are used to study the pressure dependent resonance frequency of interacting MBs on: a) the pressure amplitude of the driving acoustic field and b) the number density of MBs within a defined MB cluster. Five cubes each with a dimensions of 300µm x 300µm x 300µm containing 10, 20, 40, 60 and 80 randomly distributed MBs with initial radii of $2\mu m$ were examined. This resulted in 5 random spatial distributions of MBs with number densities of 0.370×10^6 MBs/mL, 0.740×10^6 MBs/mL, 1.481×10^6 MBs/mL, 2.223×10^6 MBs/mL and 2.963×10^6 MBs/mL that represent a wide range of relevant number densities. The frequency response of each MB within each cluster was numerically evaluated. 60 cycles of ultrasound waves, with pressure amplitudes ranging from 1kPa up to 101kPa (in 2kPa increments) and frequencies ranging from 0.5MHz up to 5MHz (in 15kHz increments) were chosen to excite the MBs.

Fig. 7.4 shows the frequency response of each individual 2µm MB within the cluster excited with ultrasound waves with a pressure amplitude of 9kPa for different number densities. MB clusters with higher number density exhibit lower pressure dependent resonance frequencies.

This result may be expected following their lower linear resonance frequencies discussed in previous section.

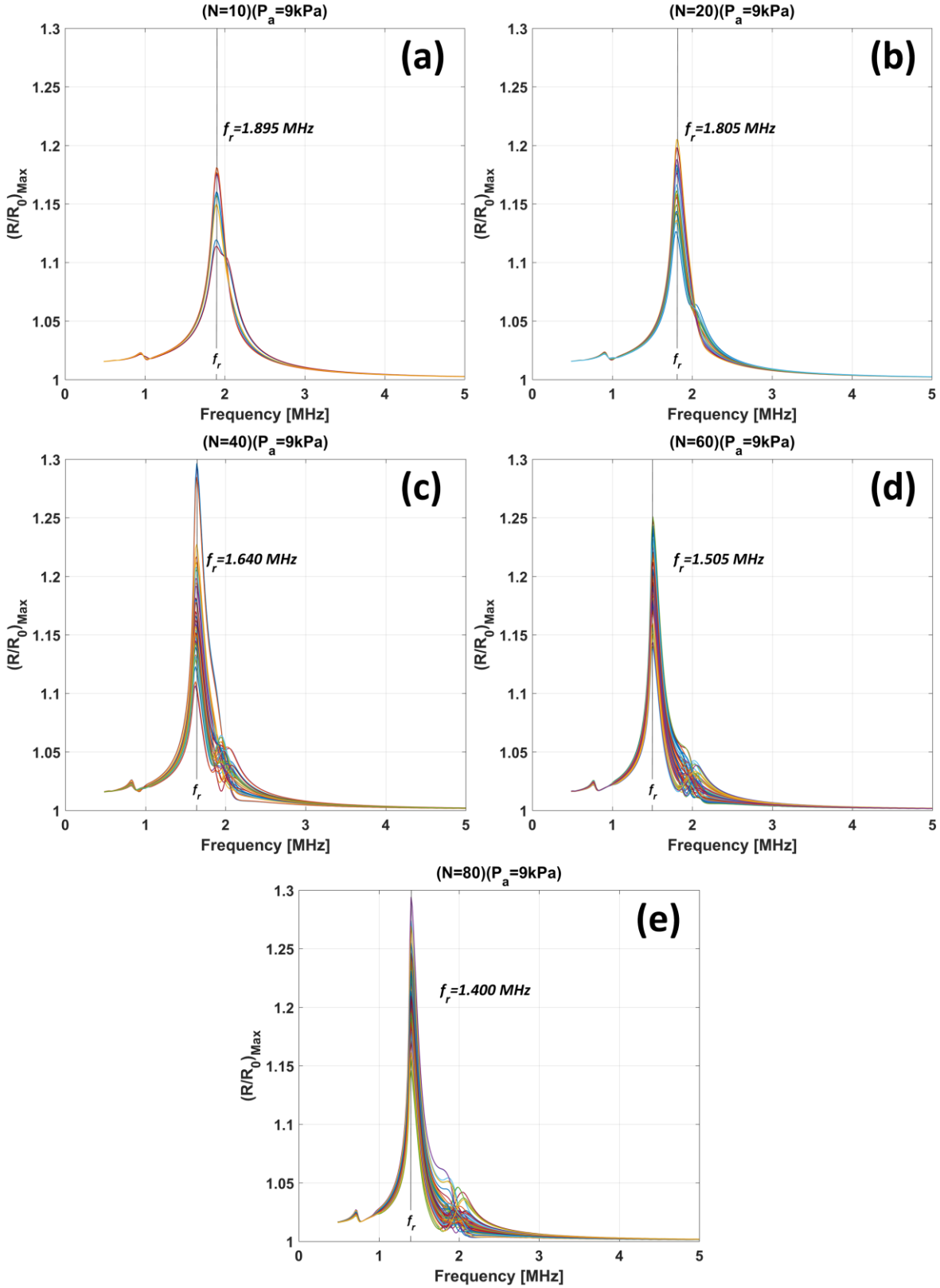

Figure 7.4- Frequency response diagram of 2μm MBs within cluster of (a) N=10, (b) N=20, (c) N=40, (d) N=60, (e) N=80 in a cube with a side of 300μm excited with ultrasonic waves with pressure amplitudes of 9kPa

At relatively low pressure amplitudes the monodisperse MB clusters maintain similar resonance frequencies. This is not the case at higher pressures. Fig. 7.5 shows frequency response diagram of each individual 2μm MB excited at a pressure amplitude of 101 kPa. For these conditions, there is a noteworthy deviation between behavior of the 2μm MBs within the cluster. As the pressure amplitude of ultrasonic excitation increases, the backscattered pressure from each MB increases as well. Therefore, the contribution of other MBs to the pressure incident on adjacent MBs (the summation term in Eq. 3.3) heavily influences the MB dynamics. Furthermore, since MBs are located at random locations within the pre-defined cube, the backscattered pressure received by each bubble is different. This results in increasingly distinct behavior as the pressure amplitude of the ultrasonic wave increases. Fig. 7.5 also shows that the MB dynamics for the MB within same cluster diversify with increasing MB number density. The differences of MB dynamics of MBs of the same size is due to the fact that the probability of receiving a greater range of backscattered pressures by each MB increases with increasing number of MBs. Furthermore, Fig. 7.5 shows that each resonance mode is pushed to lower frequencies with increasing number density. This is a result of the lower linear resonance frequency of MBs with increasing number density.

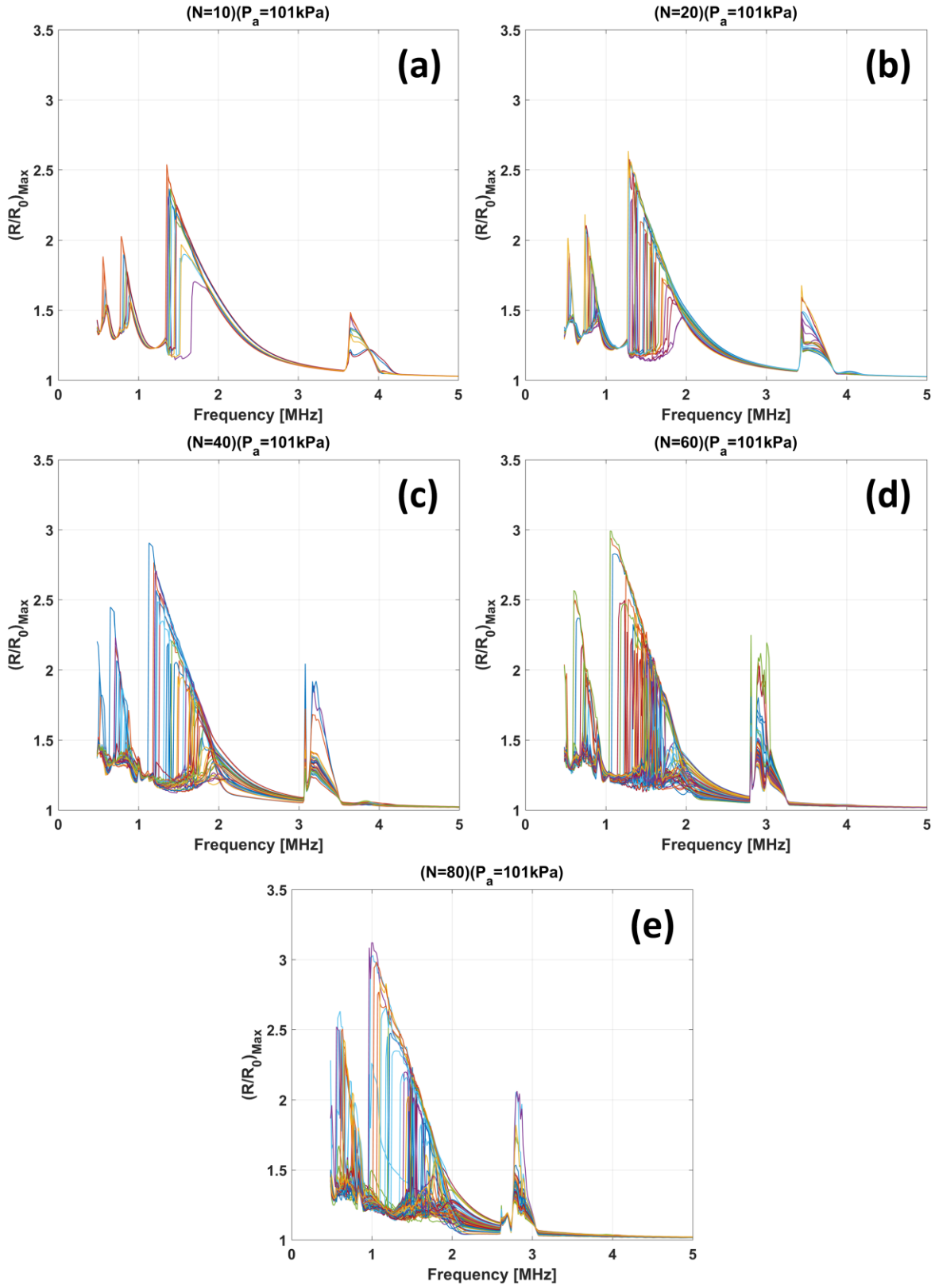

Figure 7.5- Frequency response diagram of 2μm MBs within cluster of (a) N=10, (b) N=20, (c) N=40, (d) N=60, (e) N=80 in a cube with a side of 300μm excited with ultrasonic waves with pressure amplitudes of 101kPa

For isolated MBs, increasing the ultrasound pressure amplitude forms secondary resonance modes along with the main 1/1 harmonic resonance mode (47). Similar phenomena occur for interacting MBs. Fig. 7.6 depicts the frequency response of each individual 2μm MB excited with acoustic fields of pressure amplitude of 39kPa. In this case, all of the MBs exhibit 2/1 ultraharmonic resonance modes. Moreover, Fig. 7.6 demonstrates a lower 2/1 ultraharmonic resonance frequency mode for MBs in clusters of higher number density. At lower pressure amplitudes of ultrasonic excitation (Fig. 7.4) MBs have the same 1/1 harmonic resonance frequency. For high pressure amplitudes (Figs. 7.5 and 7.6) the 1/1 harmonic resonance of the of individual MBs is not at the same frequency. At higher pressures, defining resonance becomes difficult, since MBs are resonant in the same mode (for instance 1/1 harmonic) for a wide range of frequencies (e.g. 1-2MHz in figure 7.5(e)).

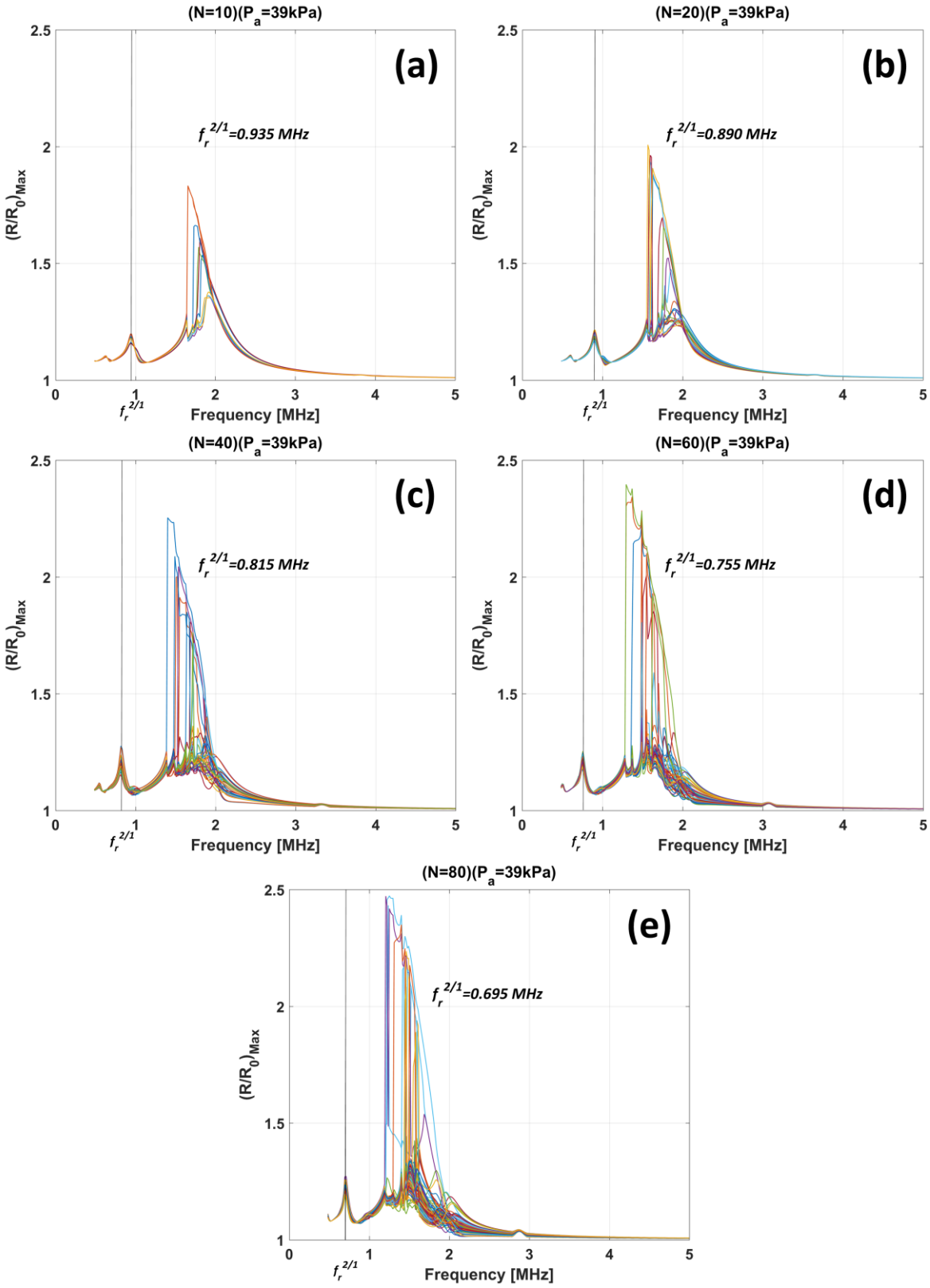

Figure 7.6- Frequency response diagram of 2μm MBs within cluster of (a) N=10, (b) N=20, (c) N=40, (d) N=60, (e) N=80 in a cube with a side of 300μm excited with ultrasonic waves with pressure amplitudes of 39kPa

Increasing the pressure amplitude of the ultrasonic waves from very low values (~1kPa) results in the formation of secondary resonance peaks (e.g. subharmonics). Initially, and for a specific range of pressure amplitudes, these peaks are at the same frequencies for all the MBs within the cluster (Fig. 7.4). However, further increasing the pressure results in spreading of the resonance frequencies of the same resonant mode for MBs within the cluster. This change in behavior is a result of inter-bubble interactions that occur at lower pressure amplitude ultrasound exposures for clusters with a higher MB number density. This is shown in Fig. 7.6, which depicts the frequency response of each individual MBs at the highest pressure amplitude of ultrasonic excitation for which all of the MBs maintain equal subharmonic frequencies (rightmost peak in Fig. 7.6). The pressure threshold for maintaining the same subharmonic frequency for all MBs decreases with increasing number density of MBs (from 91 kPa for 10 MBs to 63 kPa for 80 MBs).

These results show that monodisperse MB only behave similarly for a range of exposure parameters and this depends on the number density of MBs. The higher the number density of MBs, the narrower the control parameter range becomes in which monodisperse MBs oscillate similarly. Dissimilar oscillations may result in cancellation of collective effects of bubbles and suppression of their backscattered signals due to destructive interference (out of phase oscillations compared to scattered waves). Therefore, it is crucial to identify the ranges at which MBs oscillate similarly.

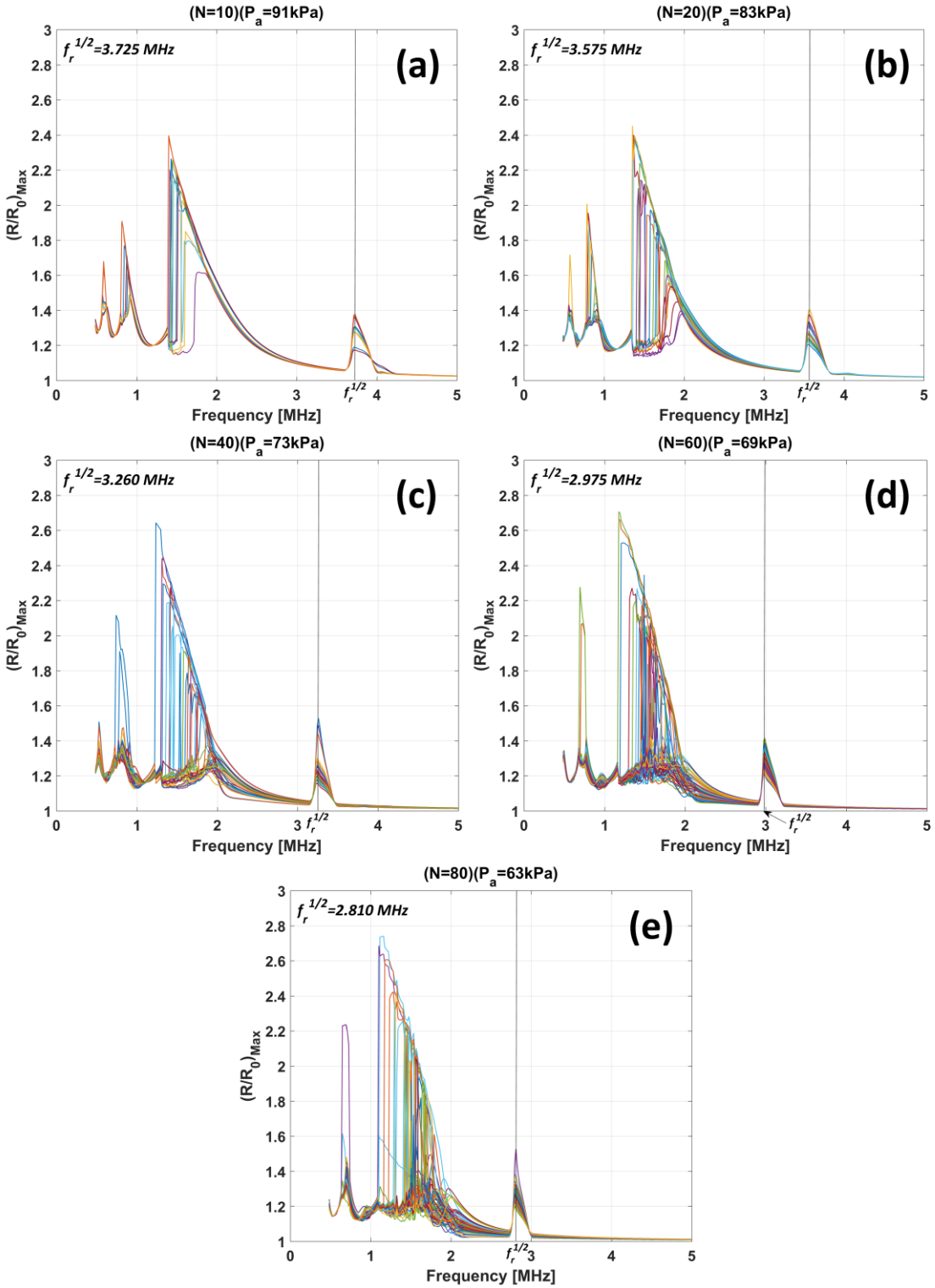

Figure 7.7- Frequency response diagram of 2µm MBs within cluster of (a) N=10 - P_a=91kPa, (b) N=20 - P_a=83kPa, (c) N=40 - P_a=73kPa, (d) N=60 - P_a=69kPa, (e) N=80 - P_a=63kPa in a cube with a side of 300µm excited with highest ultrasonic pressure at which equal subharmonic resonance (1/2 order resonance) frequencies among MBs within each cluster was maintained

7.4. Large Polydisperse Bubble Clusters

It is difficult to practically realize monodisperse clusters of MBs. Therefore, in most applications MB clusters are polydisperse. In this section inter-bubble interactions are examined for large polydisperse MB clusters. Polydisperse MB clusters consisting of 20 bubbles are formed. The number density of the MBs within the cube was chosen to be 0.6×10^6 MBs/mL. One random formation was generated and used for all three cases of 20 2µm MBs, 20 1µm MBs and a population consisting of 15 1µm and 5 2µm MBs. Fig. 7.7 illustrates the frequency response and frequency dependent bifurcation diagrams of all individual MBs excited within ultrasound waves of 100kPa amplitude. Fig. 7.7(e) and Fig. 7.7(f) show that, similar to previous cases studied in chapter 6, the largest MBs within the cluster dominate the dynamics of the MB cluster: the 2/1 order response of smaller MBs are amplified and their 3/1 order is weakened significantly. Fig. 7.7(c) and Fig. 7.7(f) demonstrate that the largest MBs in the cluster, even when in lower numbers compared to the smaller MBs, can modify and dominate the collective behavior of the MB cluster. The larger MBs are largely uninfluenced by smaller MBs. Moreover, Fig. 7.7(d) shows that a cluster consisting solely of large MBs will not have unique pressure dependent resonance modes among MBs. However, Fig. 7.7(f) shows that when combined with smaller MBs, large MBs maintain their unique pressure dependent resonance frequencies in different modes while enhancing resonances of smaller MBs in those modes. The simulations indicate that large MBs are mostly unaffected by the dynamics of smaller MBs. In section 7.3 we have shown that small numbers of same sized MBs tend to maintain similar dynamics at

higher pressures. This can be one of the reasons that larger MBs in the mixed cluster maintain similar dynamics.

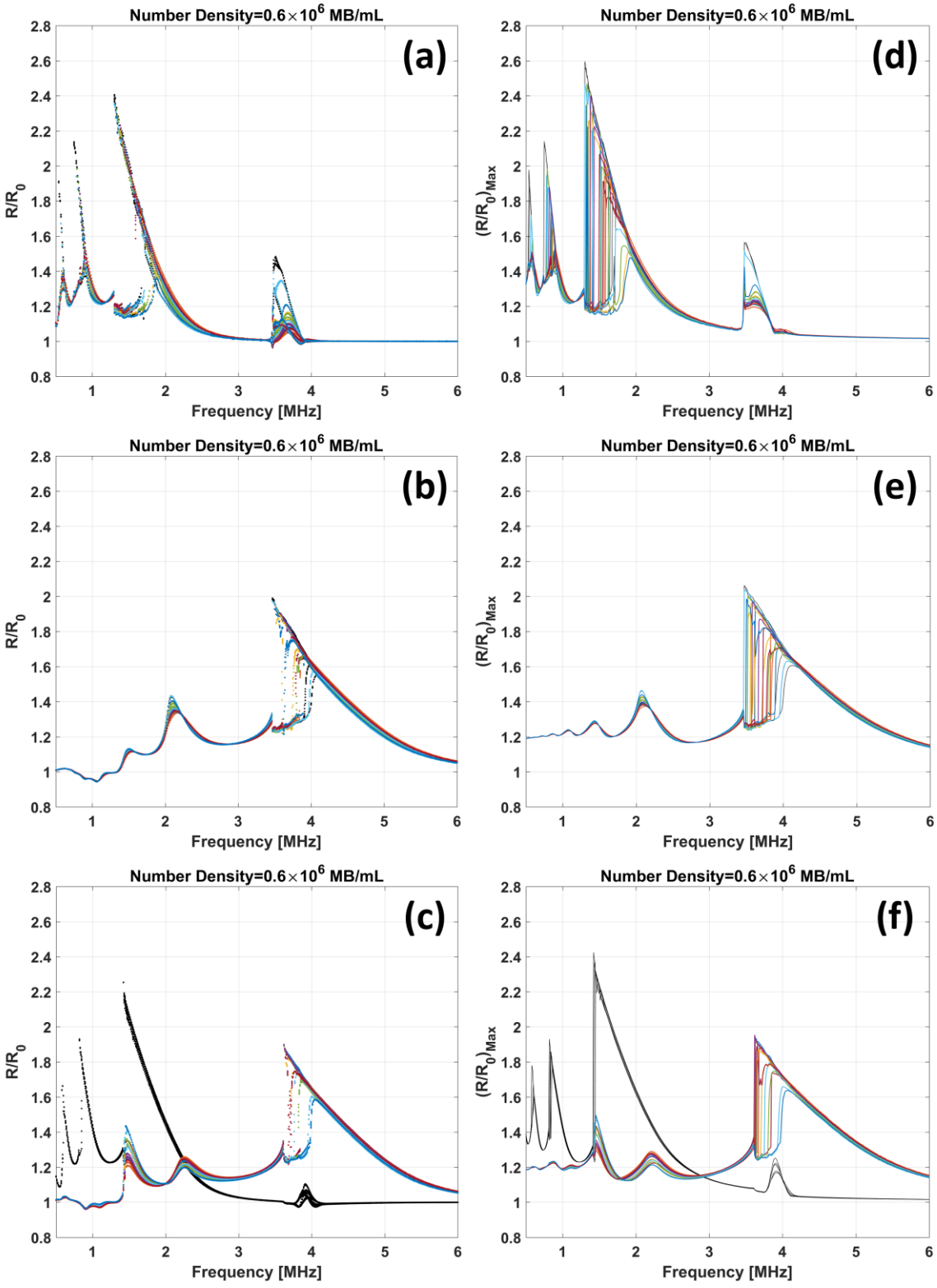

Figure 7.8- Bifurcation (a, b, c) and frequency response diagrams of polydisperse bubble clusters consisting of (a, d) 20-2μm MB (b, e) 20-1μm MB (c, f) 15-1μm + 5-2μm MB randomly distributed within a cube with a side of 300μm and sonicated with ultrasound waves of P_a=100 kPa [Black lines and dots in (c) and (f) represent 2μm MBs]

8. Conclusions and Future Directions

8.1. Summary and Conclusions

Relations governing the dynamics of multiple interacting bubbles in an infinite domain of liquid consist of a system of linearly coupled, nonlinear second order differential equations. Since analytical solutions are not available (or even possible without compromising simplifications), numerical methods were used to examine the dynamics of interacting bubbles. Conventional methods could not be used due to the increased complexity resulting from very large systems of coupled ODEs. Two methods to solve the large number of coupled differential equations without the introduction of limiting assumptions were proposed. Comparisons of solutions based on this method were found to be in excellent agreement with analytical solutions to simple systems of 2, 3 and 4 bubbles. It is important to note that one of the main assumptions made in the used model is that the cluster is small enough that the travel time of the acoustic waves within the cluster is smaller than the time scale of the oscillations and can be neglected.

Previous works (42) (41) (40) suggest emergent collective MB dynamics within bubble clusters. A small cluster of 3-4 MBs was used in this thesis to probe these interactions (the largest number of MBs in a cluster for which each MB can be equidistant from each other is 4. The inter-bubble interactions were classified into two major categories of interactions: constructive and destructive.

Destructive interactions were defined as the ones resulting in a weakening of the resonant oscillations of smaller bubbles by the largest bubble within the cluster. This happens when a resonance mode of a smaller MB (calculated when isolated) within a cluster does not align (i.e.

does have a similar frequency) with the resonance modes of largest MBs within the cluster. On the other hand, constructive interactions result in strengthening the resonant oscillations of smaller bubbles by the largest bubble(s). It was found that the largest MB within a cluster can force smaller MBs into P-2 oscillations. Moreover, the closer the size of the smaller MB to the largest MB within the cluster, the larger the distance between the bubbles that can still result in forced oscillations (e.g. into P-2 oscillations at larger distances in the simulations presented).

These findings further illustrate the importance of inter-bubble interactions in designing and optimizing applications employing MBs. Most MB applications use MBs in polydisperse clusters. Our findings indicate that using non-interacting bubble approximations to predict and optimize dynamics of bubbles can lead to erroneous conclusions due to ignoring the inter-bubble interactions. Here we present a simple technique to predict the frequency response of MBs within polydisperse clusters.

The power of the new method developed is the ability to solve large numbers of coupled ODEs. This allowed the study of the dynamics of MBs within large monodisperse clusters. The linear resonance frequency of individual MBs within a cluster was found to be the same and largely independent of their spatial distribution (for equal number densities). The linear resonance frequency of MBs was found to be dependent on their number density: monodisperse MBs in clusters with higher number densities have lower resonance frequencies.

The nonlinear response of monodisperse clusters of MBs to acoustic excitation was investigated with the aid of pressure dependent frequency response curves. At low exposure pressures, the resonance modes have the same frequency for all MBs. Further increasing the pressure

resulted in MBs exhibiting increasingly distinct resonance frequencies (for the same mode) compared to rest of the MBs in the monodisperse cluster. This behavior was found to be amplified when increasing the number density of MBs above a pressure threshold. The pressure at which a resonance mode starts deviating among individual MBs of the same size decreases as the MB number density increases.

For inter-bubble interactions in large polydisperse MB clusters, it was found that larger MBs, even in small numbers, can modify the dynamics of smaller MBs through constructive and destructive interactions while staying largely unaffected by the presence of the smaller MBs.

Theoretical studies on the dynamics of MBs within large clusters were very limited due to lack of available methods to simulate large bubble clusters. Here we presented two simple yet efficient techniques allowing us to examine the behavior of large clusters of MBs under ultrasonic excitation. The proposed approaches build the basis for future investigations into nonlinear and complex yet rich behavior of bubbles. They enable us to obtain a better and deeper understanding into behavior of MBs allowing us to optimize them further in applications and potentially invent new ones that exploit the emergent properties of MB clusters.

8.2. Future Directions

The theoretical framework presented can be used to assist in the interpretation of experimental results. For instance, sub-micron sized bubbles (nanobubbles NB) have been shown to generate strong signal at frequencies much lower than what single bubble studies predict (52). Different explanations have been offered to explain this phenomenon, such as buckling of the shell enclosing the NBs (53). We have shown here that inter-bubble interactions

can decrease the resonance frequency of bubbles with increasing number density and therefore potentially enable NBs to exhibit rich dynamics under lower than previously expected ultrasonic frequencies. A set of controlled studies on monodisperse NB clusters of different concentrations needs to be performed to validate the relevance of inter-bubble interactions to explaining this phenomenon.

In section 7.4 it was shown that large MBs, even in small numbers, can modify the overall dynamics of a MB cluster. This enables us to engineer a MB cluster for specific applications where a large number of larger sized bubbles may be problematic, and smaller MBs do not exhibit the desired properties. For instance, we have shown that larger MBs can force smaller MBs to undergo period doubling and generate subharmonic signals at lower frequencies. This may enable the use of engineered clusters to perform subharmonic ultrasound scans at greater depths since higher frequency ultrasonic beams attenuate faster with depth (54).

A relation for predicting speed of sound and attenuation of acoustic waves in bubbly medium was developed by Sojahrood et. al (55). Previous theoretical models were used to fit their output to experimentally measured data to characterize shelled ultrasound contrast agents (shelled MBs) for which the physical properties of the MB shell are largely unknown. However, previous methods were mostly based on linear oscillations of individual MBs (that are only valid for very small scale bubble oscillations, P_a <5kPa). Pressures are typically higher in the majority of MB applications. Sojahrood's model enables the user to calculate the attenuation and speed of sound in bubbly media while fully incorporating the nonlinear effects that arise from large amplitude bubble oscillations. Since this model requires knowledge of the radial oscillations of MBs to generate accurate results, it is only as accurate as the input data used in the model.

Previous attempts to fit experimental (fitting parameters are the unknown shell properties) data with theoretical predictions have used solutions to radial oscillations of isolated bubble models. This limits the full applicability of Sojahrood's approach to very dilute bubbly media. We have tested Sojahrood's model with our methods to solve large bubble clusters. The MB cluster size distribution was based on the size distribution measured in experiments. Incorporation of cluster dynamics improved the agreement of theory and experiment as shown in Fig. 8.1.

Our proposed approach, combined with Sojarhrood's approach, can be used to characterize MBs and nanobubbles (NBs). Due to the large number of input parameters, it has been difficult to character the shell properties of microbubbles and nanobubbles. Bubbles will be sorted by their sizes through advanced centrifugation (56) and by their resonance frequencies through resonance sorting (57). Sorted bubbles will be used to construct custom bubble cluster optimized for different applications.

Ultimately, having a good understanding of shell characteristics of MBs and NBs, controlling their sizes through aforementioned techniques and knowing the fundamentals of inter-bubble interactions and speed of sound and attenuation in bubbly media, will address most uncertainties of related experiments. This will help us optimize and enhance applications employing bubbles such as in contrast enhanced ultrasound imaging and drug delivery. Moreover, this will enable us to explore the potential use of NBs in different applications, and potentially invent new ones.

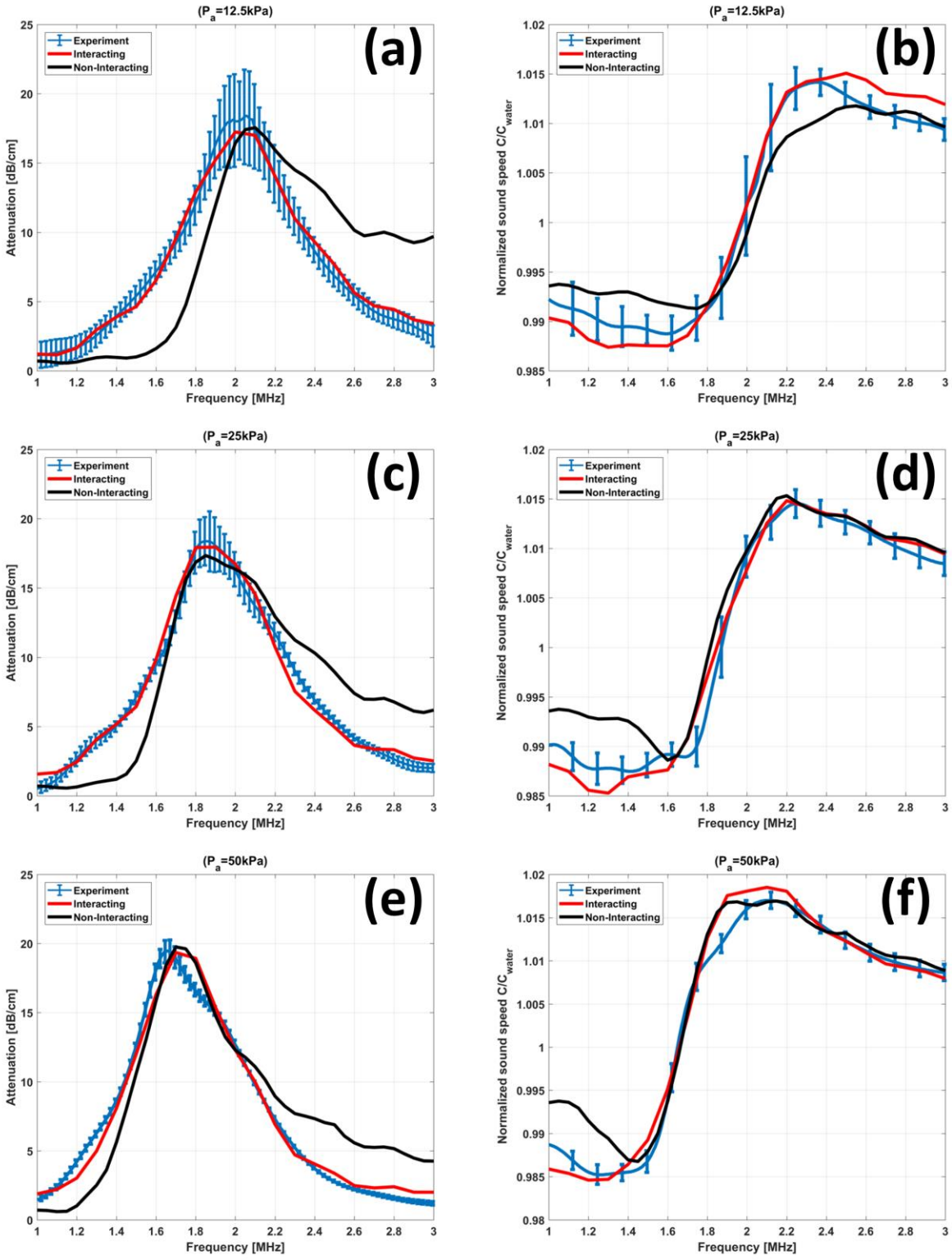

Figure 8.1- Attenuation and speed of sound measurements and simulations using Inverse Matrix method in conjunction with Sojarhood's approach (a, b) P_a=12.5kPa, (c,d) P_a=25kPa (e,f) P_a=50kPa

Appendices

Appendix-1 (Conventional Expression for 3-MB Case)

Here we are presenting the conventional expression needed to simulate a 3 MB cluster using Runge-Kutta methods. Using previous methods to isolate for the highest order of differentiations ($\ddot{R}_i$s) in Eq. 3.4 results in the following expressions for N=3:

$$\ddot{R}_1 = \left\{\left(A_1 - \frac{3}{2}\left[1 - \frac{\dot{R}_1}{3c}\right]\dot{R}_1^2 - \frac{2R_2\dot{R}_2^2}{d_{12}} - \frac{2R_3\dot{R}_3^2}{d_{13}}\right)\left[\left(\left[1 - \frac{\dot{R}_2}{c}\right]R_2 + \frac{4\mu}{\rho c}\right)\left(\left[1 - \frac{\dot{R}_3}{c}\right]R_3 + \frac{4\mu}{\rho c}\right) - \frac{R_3^2R_2^2}{d_{23}d_{32}}\right] - \left(\frac{R_2^2}{d_{12}}\right)\left[\left(\left[1 - \frac{\dot{R}_3}{c}\right]R_3 + \frac{4\mu}{\rho c}\right)\left(A_2 - \frac{3}{2}\left[1 - \frac{\dot{R}_2}{3c}\right]\dot{R}_2^2 - \frac{2R_1\dot{R}_1^2}{d_{21}} - \frac{2R_3\dot{R}_3^2}{d_{23}}\right) - \left(\frac{R_3^2}{d_{23}}\right)\left(A(3) - \frac{3}{2}\left[1 - \frac{\dot{R}_3}{3c}\right]\dot{R}_3^2 - \frac{2R_1\dot{R}_1^2}{d_{31}} - \frac{2R_2\dot{R}_2^2}{d_{32}}\right)\right] + \left(\frac{R_3^2}{d_{13}}\right)\left[\left(\frac{R_2^2}{d_{32}}\right)\left(A_2 - \frac{3}{2}\left[1 - \frac{\dot{R}_2}{3c}\right]\dot{R}_2^2 - \frac{2R_1\dot{R}_1^2}{d_{21}} - \frac{2R_3\dot{R}_3^2}{d_{23}}\right) - \left(\left(\left[1 - \frac{\dot{R}_2}{c}\right]R_2 + \frac{4\mu}{\rho c}\right)\right)\left(A_3 - \frac{3}{2}\left[1 - \frac{\dot{R}_3}{3c}\right]\dot{R}_3^2 - \frac{2R_1\dot{R}_1^2}{d_{31}} - \frac{2R_2\dot{R}_2^2}{d_{32}}\right)\right]\right\} / \left\{\left(\left[1 - \frac{\dot{R}_1}{c}\right]R_1 + \frac{4\mu}{\rho c}\right)\left[\left(\left[1 - \frac{\dot{R}_2}{c}\right]R_2 + \frac{4\mu}{\rho c}\right)\left(\left[1 - \frac{\dot{R}_3}{c}\right]R_3 + \frac{4\mu}{\rho c}\right) - \left(\frac{R_2^2R_3^2}{d_{32}d_{23}}\right)\right] - \left(\frac{R_2^2}{d_{12}}\right)\left[\left(\frac{R_1^2}{d_{21}}\right)\left(\left[1 - \frac{\dot{R}_3}{c}\right]R_3 + \frac{4\mu}{\rho c}\right) - \left(\frac{R_3^2R_1^2}{d_{23}d_{31}}\right)\right] + \left(\frac{R_3^2}{d_{13}}\right)\left[\left(\frac{R_1^2R_2^2}{d_{21}d_{32}}\right) - \left(\frac{R_1^2}{d_{31}}\right)\left(\left(\left[1 - \frac{\dot{R}_2}{c}\right]R_2 + \frac{4\mu}{\rho c}\right)\right)\right]\right\}$$

$$\ddot{R}_2 = \left\{\left(\left[1 - \frac{\dot{R}_1}{c}\right]R_1 + \frac{4\mu}{\rho c}\right)\left[\left(\left(\left[1 - \frac{\dot{R}_3}{c}\right]R_3 + \frac{4\mu}{\rho c}\right)\right)\left(A_2 - \frac{3}{2}\left[1 - \frac{\dot{R}_2}{3c}\right]\dot{R}_2^2 - \frac{2R_1\dot{R}_1^2}{d_{21}} - \frac{2R_3\dot{R}_3^2}{d_{23}}\right) - \left(A_3 - \frac{3}{2}\left[1 - \frac{\dot{R}_3}{3c}\right]\dot{R}_3^2 - \frac{2R_1\dot{R}_1^2}{d_{31}} - \frac{2R_2\dot{R}_2^2}{d_{32}}\right)\left(\frac{R_3^2}{d_{23}}\right)\right] - \left(A_1 - \frac{3}{2}\left[1 - \frac{\dot{R}_1}{3c}\right]\dot{R}_1^2 - \frac{2R_2\dot{R}_2^2}{d_{12}} - \frac{2R_3\dot{R}_3^2}{d_{13}}\right)\left[\left(\frac{R_1^2}{d_{21}}\right)\left(\left[1 - \frac{\dot{R}_3}{c}\right]R_3 + \frac{4\mu}{\rho c}\right) - \left(\frac{R_3^2R_1^2}{d_{23}d_{31}}\right)\right] + \left(\frac{R_3^2}{d_{13}}\right)\left[\left(A_2 - \frac{3}{2}\left[1 - \frac{\dot{R}_2}{3c}\right]\dot{R}_2^2 - \frac{2R_1\dot{R}_1^2}{d_{21}} - \frac{2R_3\dot{R}_3^2}{d_{23}}\right)\left(\frac{R_1^2}{d_{31}}\right) - \left(\frac{R_1^2R_2^2}{d_{21}d_{32}}\right)\right]\right\} / \left\{\left(\left[1 - \frac{\dot{R}_1}{c}\right]R_1 + \frac{4\mu}{\rho c}\right)\left[\left(\left[1 - \frac{\dot{R}_2}{c}\right]R_2 + \frac{4\mu}{\rho c}\right)\left(\left[1 - \frac{\dot{R}_3}{c}\right]R_3 + \frac{4\mu}{\rho c}\right) - \left(\frac{R_2^2R_3^2}{d_{32}d_{23}}\right)\right] - \left(\frac{R_2^2}{d_{12}}\right)\left[\left(\frac{R_1^2}{d_{21}}\right)\left(\left[1 - \frac{\dot{R}_3}{c}\right]R_3 + \frac{4\mu}{\rho c}\right) - \left(\frac{R_3^2R_1^2}{d_{23}d_{31}}\right)\right] + \left(\frac{R_3^2}{d_{13}}\right)\left[\left(\frac{R_1^2R_2^2}{d_{21}d_{32}}\right) - \left(\frac{R_1^2}{d_{31}}\right)\left(\left(\left[1 - \frac{\dot{R}_2}{c}\right]R_2 + \frac{4\mu}{\rho c}\right)\right)\right]\right\}$$

$$\ddot{R}_3 = \left\{\left(\left[1-\frac{\dot{R}_1}{c}\right]R_1+\frac{4\mu}{\rho c}\right)\left[\left(\left[1-\frac{\dot{R}_2}{c}\right]R_2+\frac{4\mu}{\rho c}\right)\left(A_3-\frac{3}{2}\left[1-\frac{\dot{R}_3}{3c}\right]\dot{R}_3^2-\frac{2R_1\dot{R}_1^2}{d_{31}}-\frac{2R_2\dot{R}_2^2}{d_{32}}\right)\right.\right.$$
$$\left.-\left(\frac{R_2^2}{d_{32}}\right)\left(A_2-\frac{3}{2}\left[1-\frac{\dot{R}_2}{3c}\right]\dot{R}_2^2-\frac{2R_1\dot{R}_1^2}{d_{21}}-\frac{2R_3\dot{R}_3^2}{d_{23}}\right)\right]$$
$$-\left(\frac{R_2^2}{d_{12}}\right)\left[\left(\frac{R_1^2}{d_{21}}\right)\left(A_3-\frac{3}{2}\left[1-\frac{\dot{R}_3}{3c}\right]\dot{R}_3^2-\frac{2R_1\dot{R}_1^2}{d_{31}}-\frac{2R_2\dot{R}_2^2}{d_{32}}\right)\right.$$
$$\left.-\left(\frac{R_1^2}{d_{31}}\right)\left(A_2-\frac{3}{2}\left[1-\frac{\dot{R}_2}{3c}\right]\dot{R}_2^2-\frac{2R_1\dot{R}_1^2}{d_{21}}-\frac{2R_3\dot{R}_3^2}{d_{23}}\right)\right]$$
$$+\left(A_1-\frac{3}{2}\left[1-\frac{\dot{R}_1}{3c}\right]\dot{R}_1^2-\frac{2R_2\dot{R}_2^2}{d_{12}}-\frac{2R_3\dot{R}_3^2}{d_{13}}\right)\left[\left(\frac{R_1^2R_2^2}{d_{21}d_{32}}\right)\right.$$
$$\left.\left.-\left(\frac{R_1^2}{d_{31}}\right)\left(\left(\left[1-\frac{\dot{R}_2}{c}\right]R_2+\frac{4\mu}{\rho c}\right)\right)\right]\right\}$$
$$/\left\{\left(\left[1-\frac{\dot{R}_1}{c}\right]R_1+\frac{4\mu}{\rho c}\right)\left[\left(\left[1-\frac{\dot{R}_2}{c}\right]R_2+\frac{4\mu}{\rho c}\right)\left(\left[1-\frac{\dot{R}_3}{c}\right]R_3+\frac{4\mu}{\rho c}\right)-\left(\frac{R_2^2R_3^2}{d_{32}d_{23}}\right)\right]\right.$$
$$-\left(\frac{R_2^2}{d_{12}}\right)\left[\left(\frac{R_1^2}{d_{21}}\right)\left(\left[1-\frac{\dot{R}_3}{c}\right]R_3+\frac{4\mu}{\rho c}\right)-\left(\frac{R_3^2R_1^2}{d_{23}d_{31}}\right)\right]$$
$$\left.+\left(\frac{R_3^2}{d_{13}}\right)\left[\left(\frac{R_1^2R_2^2}{d_{21}d_{32}}\right)-\left(\frac{R_1^2}{d_{31}}\right)\left(\left(\left[1-\frac{\dot{R}_2}{c}\right]R_2+\frac{4\mu}{\rho c}\right)\right)\right]\right\}$$

Appendix-2 (Conventional Expression for 4-MB Case)

Here we are presenting the conventional expression needed to simulate a 4 MB cluster using Runge-Kutta methods. Using previous methods to isolate for the highest order of differentiations ($\dot{R}$_is) in Eq. 3.4 results in the following expressions for N=4:

$$\ddot{R}_1 = \Bigg\{\Bigg\{\Bigg[\left(1-\frac{\dot{R}_2}{c}\right)R_2+\frac{4\mu}{\rho c}\Bigg]\Bigg[\left(1-\frac{\dot{R}_3}{c}\right)R_3+\frac{4\mu}{\rho c}\Bigg]\Bigg[\left(1-\frac{\dot{R}_4}{c}\right)R_4+\frac{4\mu}{\rho c}\Bigg]+\frac{{R_3}^2}{d_{23}}\frac{{R_4}^2}{d_{34}}\frac{{R_2}^2}{d_{42}}+\frac{{R_4}^2}{d_{24}}\frac{{R_2}^2}{d_{32}}\frac{{R_3}^2}{d_{43}}$$

$$-\Bigg[\left(1-\frac{\dot{R}_2}{c}\right)R_2+\frac{4\mu}{\rho c}\Bigg]\frac{{R_4}^2}{d_{34}}\frac{{R_3}^2}{d_{43}}-\frac{{R_3}^2}{d_{23}}\frac{{R_2}^2}{d_{32}}\Bigg[\left(1-\frac{\dot{R}_4}{c}\right)R_4+\frac{4\mu}{\rho c}\Bigg]$$

$$-\frac{{R_4}^2}{d_{24}}\Bigg[\left(1-\frac{\dot{R}_3}{c}\right)R_3+\frac{4\mu}{\rho c}\Bigg]\frac{{R_2}^2}{d_{42}}\Bigg\}\Bigg[A_1-\frac{3}{2}\Bigg[1-\frac{\dot{R}_1}{3c}\Bigg]\dot{R}_1^2-\frac{2R_2\dot{R}_2^2}{d_{12}}-\frac{2R_3\dot{R}_3^2}{d_{13}}-\frac{2R_4\dot{R}_4^2}{d_{14}}\Bigg]$$

$$+\Bigg\{\frac{{R_2}^2}{d_{12}}\frac{{R_4}^2}{d_{34}}\frac{{R_3}^2}{d_{43}}+\frac{{R_3}^2}{d_{13}}\frac{{R_2}^2}{d_{32}}\Bigg[\left(1-\frac{\dot{R}_4}{c}\right)R_4+\frac{4\mu}{\rho c}\Bigg]+\frac{{R_4}^2}{d_{14}}\Bigg[\left(1-\frac{\dot{R}_3}{c}\right)R_3+\frac{4\mu}{\rho c}\Bigg]\frac{{R_2}^2}{d_{42}}$$

$$-\frac{{R_2}^2}{d_{12}}\Bigg[\left(1-\frac{\dot{R}_3}{c}\right)R_3+\frac{4\mu}{\rho c}\Bigg]\Bigg[\left(1-\frac{\dot{R}_4}{c}\right)R_4+\frac{4\mu}{\rho c}\Bigg]-\frac{{R_3}^2}{d_{13}}\frac{{R_4}^2}{d_{34}}\frac{{R_2}^2}{d_{42}}-\frac{{R_4}^2}{d_{14}}\frac{{R_2}^2}{d_{32}}\frac{{R_3}^2}{d_{43}}\Bigg\}\Bigg[A_2$$

$$-\frac{3}{2}\Bigg[1-\frac{\dot{R}_2}{3c}\Bigg]\dot{R}_2^2-\frac{2R_1\dot{R}_1^2}{d_{21}}-\frac{2R_3\dot{R}_3^2}{d_{23}}-\frac{2R_4\dot{R}_4^2}{d_{24}}\Bigg]$$

$$+\Bigg\{\frac{{R_2}^2}{d_{12}}\frac{{R_3}^2}{d_{23}}\Bigg[\left(1-\frac{\dot{R}_4}{c}\right)R_4+\frac{4\mu}{\rho c}\Bigg]+\frac{{R_3}^2}{d_{13}}\frac{{R_4}^2}{d_{24}}\frac{{R_2}^2}{d_{42}}+\frac{{R_4}^2}{d_{14}}\Bigg[\left(1-\frac{\dot{R}_2}{c}\right)R_2+\frac{4\mu}{\rho c}\Bigg]\frac{{R_3}^2}{d_{43}}-\frac{{R_2}^2}{d_{12}}\frac{{R_4}^2}{d_{24}}\frac{{R_3}^2}{d_{43}}$$

$$-\frac{{R_3}^2}{d_{13}}\Bigg[\left(1-\frac{\dot{R}_2}{c}\right)R_2+\frac{4\mu}{\rho c}\Bigg]\Bigg[\left(1-\frac{\dot{R}_4}{c}\right)R_4+\frac{4\mu}{\rho c}\Bigg]-\frac{{R_4}^2}{d_{14}}\frac{{R_3}^2}{d_{23}}\frac{{R_2}^2}{d_{42}}\Bigg\}\Bigg[A_3-\frac{3}{2}\Bigg[1-\frac{\dot{R}_3}{3c}\Bigg]\dot{R}_3^2-\frac{2R_1\dot{R}_1^2}{d_{31}}$$

$$-\frac{2R_2\dot{R}_2^2}{d_{32}}-\frac{2R_4\dot{R}_4^2}{d_{34}}\Bigg]$$

$$+\Bigg\{\frac{{R_2}^2}{d_{12}}\frac{{R_4}^2}{d_{24}}\Bigg[\left(1-\frac{\dot{R}_3}{c}\right)R_3+\frac{4\mu}{\rho c}\Bigg]+\frac{{R_3}^2}{d_{13}}\Bigg[\left(1-\frac{\dot{R}_2}{c}\right)R_2+\frac{4\mu}{\rho c}\Bigg]\frac{{R_4}^2}{d_{34}}+\frac{{R_4}^2}{d_{14}}\frac{{R_3}^2}{d_{23}}\frac{{R_2}^2}{d_{32}}-\frac{{R_2}^2}{d_{12}}\frac{{R_3}^2}{d_{23}}\frac{{R_4}^2}{d_{34}}$$

$$-\frac{{R_3}^2}{d_{13}}\frac{{R_4}^2}{d_{24}}\frac{{R_2}^2}{d_{32}}-\frac{{R_4}^2}{d_{14}}\Bigg[\left(1-\frac{\dot{R}_2}{c}\right)R_2+\frac{4\mu}{\rho c}\Bigg]\Bigg[\left(1-\frac{\dot{R}_3}{c}\right)R_3+\frac{4\mu}{\rho c}\Bigg]\Bigg\}\Bigg[A_4-\frac{3}{2}\Bigg[1-\frac{\dot{R}_4}{3c}\Bigg]\dot{R}_4^2-\frac{2R_1\dot{R}_1^2}{d_{41}}$$

$$-\frac{2R_2\dot{R}_2^2}{d_{42}}-\frac{2R_3\dot{R}_3^2}{d_{43}}\Bigg]\Bigg\}$$

$$/\Bigg\{\Bigg[\left(1-\frac{\dot{R}_1}{c}\right)R_1+\frac{4\mu}{\rho c}\Bigg]\Bigg(\Bigg[\left(1-\frac{\dot{R}_2}{c}\right)R_2+\frac{4\mu}{\rho c}\Bigg]\Bigg[\left(1-\frac{\dot{R}_3}{c}\right)R_3+\frac{4\mu}{\rho c}\Bigg]\Bigg[\left(1-\frac{\dot{R}_4}{c}\right)R_4+\frac{4\mu}{\rho c}\Bigg]$$

$$+\frac{{R_3}^2}{d_{23}}\frac{{R_4}^2}{d_{34}}\frac{{R_2}^2}{d_{42}}+\frac{{R_4}^2}{d_{24}}\frac{{R_2}^2}{d_{32}}\frac{{R_3}^2}{d_{43}}-\Bigg[\left(1-\frac{\dot{R}_2}{c}\right)R_2+\frac{4\mu}{\rho c}\Bigg]\frac{{R_4}^2}{d_{34}}\frac{{R_3}^2}{d_{43}}-\frac{{R_3}^2}{d_{23}}\frac{{R_2}^2}{d_{32}}\Bigg[\left(1-\frac{\dot{R}_4}{c}\right)R_4+\frac{4\mu}{\rho c}\Bigg]$$

$$-\frac{{R_4}^2}{d_{24}}\Bigg[\left(1-\frac{\dot{R}_3}{c}\right)R_3+\frac{4\mu}{\rho c}\Bigg]\frac{{R_2}^2}{d_{42}}\Bigg)$$

$$+\frac{{R_2}^2}{d_{12}}\Bigg(\frac{{R_1}^2}{d_{21}}\frac{{R_4}^2}{d_{34}}\frac{{R_3}^2}{d_{43}}+\frac{{R_3}^2}{d_{23}}\frac{{R_1}^2}{d_{31}}\Bigg[\left(1-\frac{\dot{R}_4}{c}\right)R_4+\frac{4\mu}{\rho c}\Bigg]+\frac{{R_4}^2}{d_{24}}\Bigg[\left(1-\frac{\dot{R}_3}{c}\right)R_3+\frac{4\mu}{\rho c}\Bigg]\frac{{R_1}^2}{d_{41}}$$

$$-\frac{{R_1}^2}{d_{21}}\left[\left(1-\frac{\dot{R}_3}{c}\right)R_3+\frac{4\mu}{\rho c}\right]\left[\left(1-\frac{\dot{R}_3}{c}\right)R_3+\frac{4\mu}{\rho c}\right]-\frac{{R_3}^2}{d_{23}}\frac{{R_4}^2}{d_{34}}\frac{{R_1}^2}{d_{41}}-\frac{{R_4}^2}{d_{24}}\frac{{R_1}^2}{d_{31}}\frac{{R_3}^2}{d_{43}}\Bigg)$$

$$+\frac{{R_3}^2}{d_{13}}\left(\frac{{R_1}^2}{d_{21}}\frac{{R_2}^2}{d_{32}}\left[\left(1-\frac{\dot{R}_4}{c}\right)R_4+\frac{4\mu}{\rho c}\right]+\left[\left(1-\frac{\dot{R}_2}{c}\right)R_2+\frac{4\mu}{\rho c}\right]\frac{{R_4}^2}{d_{34}}\frac{{R_1}^2}{d_{41}}+\frac{{R_4}^2}{d_{24}}\frac{{R_1}^2}{d_{31}}\frac{{R_2}^2}{d_{42}}\right.$$

$$-\frac{{R_1}^2}{d_{21}}\frac{{R_4}^2}{d_{34}}\frac{{R_2}^2}{d_{42}}-\left[\left(1-\frac{\dot{R}_2}{c}\right)R_2+\frac{4\mu}{\rho c}\right]\frac{{R_1}^2}{d_{31}}\left[\left(1-\frac{\dot{R}_4}{c}\right)R_4+\frac{4\mu}{\rho c}\right]-\frac{{R_4}^2}{d_{24}}\frac{{R_2}^2}{d_{32}}\frac{{R_1}^2}{d_{41}}\Bigg)$$

$$+\frac{{R_4}^2}{d_{14}}\left(\frac{{R_1}^2}{d_{21}}\left[\left(1-\frac{\dot{R}_3}{c}\right)R_3+\frac{4\mu}{\rho c}\right]\frac{{R_2}^2}{d_{42}}+\left[\left(1-\frac{\dot{R}_2}{c}\right)R_2+\frac{4\mu}{\rho c}\right]\frac{{R_1}^2}{d_{31}}\frac{{R_3}^2}{d_{43}}+\frac{{R_3}^2}{d_{23}}\frac{{R_2}^2}{d_{32}}\frac{{R_1}^2}{d_{41}}\right.$$

$$\left.\left.-\frac{{R_1}^2}{d_{21}}\frac{{R_2}^2}{d_{32}}\frac{{R_3}^2}{d_{43}}-\left[\left(1-\frac{\dot{R}_2}{c}\right)R_2+\frac{4\mu}{\rho c}\right]\left[\left(1-\frac{\dot{R}_3}{c}\right)R_3+\frac{4\mu}{\rho c}\right]\frac{{R_1}^2}{d_{41}}-\frac{{R_3}^2}{d_{23}}\frac{{R_1}^2}{d_{31}}\frac{{R_2}^2}{d_{42}}\right)\right\}$$

$$
\begin{aligned}
\ddot{R}_2 = \Bigg\{ & \Bigg\{ \frac{{R_1}^2}{d_{21}} \frac{{R_4}^2}{d_{34}} \frac{{R_3}^2}{d_{43}} + \frac{{R_3}^2}{d_{23}} \frac{{R_3}^2}{d_{31}} \left[\left(1 - \frac{\dot{R}_4}{c} \right) R_4 + \frac{4\mu}{\rho c} \right] + \frac{{R_4}^2}{d_{24}} \left[\left(1 - \frac{\dot{R}_3}{c} \right) R_3 + \frac{4\mu}{\rho c} \right] \frac{{R_1}^2}{d_{41}} \\
& - \frac{{R_1}^2}{d_{21}} \left[\left(1 - \frac{\dot{R}_3}{c} \right) R_3 + \frac{4\mu}{\rho c} \right] \left[\left(1 - \frac{\dot{R}_4}{c} \right) R_4 + \frac{4\mu}{\rho c} \right] - \frac{{R_3}^2}{d_{23}} \frac{{R_4}^2}{d_{34}} \frac{{R_1}^2}{d_{41}} - \frac{{R_4}^2}{d_{24}} \frac{{R_1}^2}{d_{31}} \frac{{R_3}^2}{d_{43}} \Bigg\} \Bigg[A_1 \\
& - \frac{3}{2} \left[1 - \frac{\dot{R}_1}{3c} \right] \dot{R}_1^2 - \frac{2R_2 \dot{R}_2^2}{d_{12}} - \frac{2R_3 \dot{R}_3^2}{d_{13}} - \frac{2R_4 \dot{R}_4^2}{d_{14}} \Bigg] \\
& + \Bigg\{ \left[\left(1 - \frac{\dot{R}_1}{c} \right) R_1 + \frac{4\mu}{\rho c} \right] \left[\left(1 - \frac{\dot{R}_3}{c} \right) R_3 + \frac{4\mu}{\rho c} \right] \left[\left(1 - \frac{\dot{R}_4}{c} \right) R_4 + \frac{4\mu}{\rho c} \right] + \frac{{R_3}^2}{d_{13}} \frac{{R_4}^2}{d_{34}} \frac{{R_1}^2}{d_{41}} + \frac{{R_4}^2}{d_{14}} \frac{{R_1}^2}{d_{31}} \frac{{R_3}^2}{d_{43}} \\
& - \left[\left(1 - \frac{\dot{R}_1}{c} \right) R_1 + \frac{4\mu}{\rho c} \right] \frac{{R_4}^2}{d_{34}} \frac{{R_3}^2}{d_{43}} - \frac{{R_3}^2}{d_{13}} \frac{{R_1}^2}{d_{31}} \left[\left(1 - \frac{\dot{R}_4}{c} \right) R_4 + \frac{4\mu}{\rho c} \right] \\
& - \frac{{R_4}^2}{d_{14}} \left[\left(1 - \frac{\dot{R}_3}{c} \right) R_3 + \frac{4\mu}{\rho c} \right] \frac{{R_1}^2}{d_{41}} \Bigg\} \left[A_2 - \frac{3}{2} \left[1 - \frac{\dot{R}_2}{3c} \right] \dot{R}_2^2 - \frac{2R_1 \dot{R}_1^2}{d_{21}} - \frac{2R_3 \dot{R}_3^2}{d_{23}} - \frac{2R_4 \dot{R}_4^2}{d_{24}} \right] \\
& + \Bigg\{ \left[\left(1 - \frac{\dot{R}_1}{c} \right) R_1 + \frac{4\mu}{\rho c} \right] \frac{{R_4}^2}{d_{24}} \frac{{R_3}^2}{d_{43}} + \frac{{R_3}^2}{d_{13}} \frac{{R_1}^2}{d_{21}} \left[\left(1 - \frac{\dot{R}_4}{c} \right) R_4 + \frac{4\mu}{\rho c} \right] + \frac{{R_4}^2}{d_{14}} \frac{{R_3}^2}{d_{23}} \frac{{R_1}^2}{d_{41}} \\
& - \left[\left(1 - \frac{\dot{R}_1}{c} \right) R_1 + \frac{4\mu}{\rho c} \right] \frac{{R_3}^2}{d_{23}} \left[\left(1 - \frac{\dot{R}_1}{c} \right) R_1 + \frac{4\mu}{\rho c} \right] - \frac{{R_3}^2}{d_{13}} \frac{{R_{j4}}^2}{d_{24}} \frac{{R_1}^2}{d_{41}} - \frac{{R_4}^2}{d_{14}} \frac{{R_1}^2}{d_{21}} \frac{{R_3}^2}{d_{43}} \Bigg\} \Bigg[A_3 \\
& - \frac{3}{2} \left[1 - \frac{\dot{R}_3}{3c} \right] \dot{R}_3^2 - \frac{2R_1 \dot{R}_1^2}{d_{31}} - \frac{2R_2 \dot{R}_2^2}{d_{32}} - \frac{2R_4 \dot{R}_4^2}{d_{34}} \Bigg] \\
& + \Bigg\{ \left[\left(1 - \frac{\dot{R}_1}{c} \right) R_1 + \frac{4\mu}{\rho c} \right] \frac{{R_3}^2}{d_{23}} \frac{{R_4}^2}{d_{34}} + \frac{{R_3}^2}{d_{13}} \frac{{R_4}^2}{d_{24}} \frac{{R_1}^2}{d_{31}} + \frac{{R_4}^2}{d_{14}} \frac{{R_1}^2}{d_{21}} \left[\left(1 - \frac{\dot{R}_3}{c} \right) R_3 + \frac{4\mu}{\rho c} \right] \\
& - \left[\left(1 - \frac{\dot{R}_1}{c} \right) R_1 + \frac{4\mu}{\rho c} \right] \frac{{R_4}^2}{d_{24}} \left[\left(1 - \frac{\dot{R}_3}{c} \right) R_3 + \frac{4\mu}{\rho c} \right] - \frac{{R_3}^2}{d_{13}} \frac{{R_1}^2}{d_{21}} \frac{{R_4}^2}{d_{34}} - \frac{{R_4}^2}{d_{14}} \frac{{R_3}^2}{d_{23}} \frac{{R_1}^2}{d_{31}} \Bigg\} \Bigg[A_4 \\
& - \frac{3}{2} \left[1 - \frac{\dot{R}_4}{3c} \right] \dot{R}_4^2 - \frac{2R_1 \dot{R}_1^2}{d_{41}} - \frac{2R_2 \dot{R}_2^2}{d_{42}} - \frac{2R_3 \dot{R}_3^2}{d_{43}} \Bigg] \Bigg\} \\
& / \Bigg\{ \left[\left(1 - \frac{\dot{R}_1}{c} \right) R_1 + \frac{4\mu}{\rho c} \right] \Bigg(\left[\left(1 - \frac{\dot{R}_2}{c} \right) R_2 + \frac{4\mu}{\rho c} \right] \left[\left(1 - \frac{\dot{R}_3}{c} \right) R_3 + \frac{4\mu}{\rho c} \right] \left[\left(1 - \frac{\dot{R}_4}{c} \right) R_4 + \frac{4\mu}{\rho c} \right] \\
& + \frac{{R_3}^2}{d_{23}} \frac{{R_4}^2}{d_{34}} \frac{{R_2}^2}{d_{42}} + \frac{{R_4}^2}{d_{24}} \frac{{R_2}^2}{d_{32}} \frac{{R_3}^2}{d_{43}} - \left[\left(1 - \frac{\dot{R}_2}{c} \right) R_2 + \frac{4\mu}{\rho c} \right] \frac{{R_4}^2}{d_{34}} \frac{{R_3}^2}{d_{43}} - \frac{{R_3}^2}{d_{23}} \frac{{R_2}^2}{d_{32}} \left[\left(1 - \frac{\dot{R}_4}{c} \right) R_4 + \frac{4\mu}{\rho c} \right] \\
& - \frac{{R_4}^2}{d_{24}} \left[\left(1 - \frac{\dot{R}_3}{c} \right) R_3 + \frac{4\mu}{\rho c} \right] \frac{{R_2}^2}{d_{42}} \Bigg) \\
& + \frac{{R_2}^2}{d_{12}} \Bigg(\frac{{R_1}^2}{d_{21}} \frac{{R_4}^2}{d_{34}} \frac{{R_3}^2}{d_{43}} + \frac{{R_3}^2}{d_{23}} \frac{{R_1}^2}{d_{31}} \left[\left(1 - \frac{\dot{R}_4}{c} \right) R_4 + \frac{4\mu}{\rho c} \right] + \frac{{R_4}^2}{d_{24}} \left[\left(1 - \frac{\dot{R}_3}{c} \right) R_3 + \frac{4\mu}{\rho c} \right] \frac{{R_1}^2}{d_{41}} \\
& - \frac{{R_1}^2}{d_{21}} \left[\left(1 - \frac{\dot{R}_3}{c} \right) R_3 + \frac{4\mu}{\rho c} \right] \left[\left(1 - \frac{\dot{R}_3}{c} \right) R_3 + \frac{4\mu}{\rho c} \right] - \frac{{R_3}^2}{d_{23}} \frac{{R_4}^2}{d_{34}} \frac{{R_1}^2}{d_{41}} - \frac{{R_4}^2}{d_{24}} \frac{{R_1}^2}{d_{31}} \frac{{R_3}^2}{d_{43}} \Bigg) \\
& + \frac{{R_3}^2}{d_{13}} \Bigg(\frac{{R_1}^2}{d_{21}} \frac{{R_2}^2}{d_{32}} \left[\left(1 - \frac{\dot{R}_4}{c} \right) R_4 + \frac{4\mu}{\rho c} \right] + \left[\left(1 - \frac{\dot{R}_2}{c} \right) R_2 + \frac{4\mu}{\rho c} \right] \frac{{R_4}^2}{d_{34}} \frac{{R_1}^2}{d_{41}} + \frac{{R_4}^2}{d_{24}} \frac{{R_1}^2}{d_{31}} \frac{{R_2}^2}{d_{42}} \\
& - \frac{{R_1}^2}{d_{21}} \frac{{R_4}^2}{d_{34}} \frac{{R_2}^2}{d_{42}} - \left[\left(1 - \frac{\dot{R}_2}{c} \right) R_2 + \frac{4\mu}{\rho c} \right] \frac{{R_1}^2}{d_{31}} \left[\left(1 - \frac{\dot{R}_4}{c} \right) R_4 + \frac{4\mu}{\rho c} \right] - \frac{{R_4}^2}{d_{24}} \frac{{R_2}^2}{d_{32}} \frac{{R_1}^2}{d_{41}} \Bigg) \\
& + \frac{{R_4}^2}{d_{14}} \Bigg(\frac{{R_1}^2}{d_{21}} \left[\left(1 - \frac{\dot{R}_3}{c} \right) R_3 + \frac{4\mu}{\rho c} \right] \frac{{R_2}^2}{d_{42}} + \left[\left(1 - \frac{\dot{R}_2}{c} \right) R_2 + \frac{4\mu}{\rho c} \right] \frac{{R_1}^2}{d_{31}} \frac{{R_3}^2}{d_{43}} + \frac{{R_3}^2}{d_{23}} \frac{{R_2}^2}{d_{32}} \frac{{R_1}^2}{d_{41}} \\
& - \frac{{R_1}^2}{d_{21}} \frac{{R_2}^2}{d_{32}} \frac{{R_3}^2}{d_{43}} - \left[\left(1 - \frac{\dot{R}_2}{c} \right) R_2 + \frac{4\mu}{\rho c} \right] \left[\left(1 - \frac{\dot{R}_3}{c} \right) R_3 + \frac{4\mu}{\rho c} \right] \frac{{R_1}^2}{d_{41}} - \frac{{R_3}^2}{d_{23}} \frac{{R_1}^2}{d_{31}} \frac{{R_2}^2}{d_{42}} \Bigg) \Bigg\}
\end{aligned}
$$

$$
\begin{aligned}
\ddot{R}_3 = \Bigg\{ & \Bigg\{ \frac{{R_1}^2}{d_{21}} \frac{{R_2}^2}{d_{32}} \left[\left(1 - \frac{\dot{R}_4}{c} \right) R_4 + \frac{4\mu}{\rho c} \right] + \left[\left(1 - \frac{\dot{R}_2}{c} \right) R_2 + \frac{4\mu}{\rho c} \right] \frac{{R_4}^2}{d_{34}} \frac{{R_1}^2}{d_{41}} + \frac{{R_4}^2}{d_{24}} \frac{{R_1}^2}{d_{31}} \frac{{R_2}^2}{d_{42}} - \frac{{R_1}^2}{d_{21}} \frac{{R_4}^2}{d_{34}} \frac{{R_2}^2}{d_{42}} \\
& - \left[\left(1 - \frac{\dot{R}_2}{c} \right) R_2 + \frac{4\mu}{\rho c} \right] \frac{{R_1}^2}{d_{31}} \left[\left(1 - \frac{\dot{R}_4}{c} \right) R_4 + \frac{4\mu}{\rho c} \right] - \frac{{R_4}^2}{d_{24}} \frac{{R_2}^2}{d_{32}} \frac{{R_1}^2}{d_{41}} \Bigg\} \left[A_1 - \frac{3}{2} \left[1 - \frac{\dot{R}_1}{3c} \right] \dot{R}_1^2 - \frac{2R_2 \dot{R}_2^2}{d_{12}} \right. \\
& \left. - \frac{2R_3 \dot{R}_3^2}{d_{13}} - \frac{2R_4 \dot{R}_4^2}{d_{14}} \right] \\
& + \Bigg\{ \left[\left(1 - \frac{\dot{R}_1}{c} \right) R_1 + \frac{4\mu}{\rho c} \right] \frac{{R_4}^2}{d_{34}} \frac{{R_2}^2}{d_{42}} + \frac{{R_2}^2}{d_{12}} \frac{{R_1}^2}{d_{31}} \left[\left(1 - \frac{\dot{R}_4}{c} \right) R_4 + \frac{4\mu}{\rho c} \right] + \frac{{R_4}^2}{d_{14}} \frac{{R_2}^2}{d_{32}} \frac{{R_1}^2}{d_{41}} \\
& - \left[\left(1 - \frac{\dot{R}_1}{c} \right) R_1 + \frac{4\mu}{\rho c} \right] \frac{{R_2}^2}{d_{32}} \left[\left(1 - \frac{\dot{R}_4}{c} \right) R_4 + \frac{4\mu}{\rho c} \right] - \frac{{R_2}^2}{d_{12}} \frac{{R_4}^2}{d_{34}} \frac{{R_1}^2}{d_{41}} - \frac{{R_4}^2}{d_{14}} \frac{{R_1}^2}{d_{31}} \frac{{R_2}^2}{d_{42}} \Bigg\} \left[A_2 \right. \\
& \left. - \frac{3}{2} \left[1 - \frac{\dot{R}_2}{3c} \right] \dot{R}_2^2 - \frac{2R_1 \dot{R}_1^2}{d_{21}} - \frac{2R_3 \dot{R}_3^2}{d_{23}} - \frac{2R_4 \dot{R}_4^2}{d_{24}} \right] \\
& + \Bigg\{ \left[\left(1 - \frac{\dot{R}_1}{c} \right) R_1 + \frac{4\mu}{\rho c} \right] \left[\left(1 - \frac{\dot{R}_2}{c} \right) R_2 + \frac{4\mu}{\rho c} \right] \left[\left(1 - \frac{\dot{R}_4}{c} \right) R_4 + \frac{4\mu}{\rho c} \right] + \frac{{R_2}^2}{d_{12}} \frac{{R_4}^2}{d_{24}} \frac{{R_1}^2}{d_{41}} + \frac{{R_4}^2}{d_{14}} \frac{{R_1}^2}{d_{21}} \frac{{R_2}^2}{d_{42}} \\
& - \left[\left(1 - \frac{\dot{R}_1}{c} \right) R_1 + \frac{4\mu}{\rho c} \right] \frac{{R_4}^2}{d_{24}} \frac{{R_2}^2}{d_{42}} - \frac{{R_2}^2}{d_{12}} \frac{{R_1}^2}{d_{21}} \left[\left(1 - \frac{\dot{R}_4}{c} \right) R_4 + \frac{4\mu}{\rho c} \right] \\
& - \frac{{R_4}^2}{d_{14}} \left[\left(1 - \frac{\dot{R}_2}{c} \right) R_2 + \frac{4\mu}{\rho c} \right] \frac{{R_1}^2}{d_{41}} \Bigg\} \left[A_3 - \frac{3}{2} \left[1 - \frac{\dot{R}_3}{3c} \right] \dot{R}_3^2 - \frac{2R_1 \dot{R}_1^2}{d_{31}} - \frac{2R_2 \dot{R}_2^2}{d_{32}} - \frac{2R_4 \dot{R}_4^2}{d_{34}} \right] \\
& + \Bigg\{ \left[\left(1 - \frac{\dot{R}_1}{c} \right) R_1 + \frac{4\mu}{\rho c} \right] \frac{{R_4}^2}{d_{24}} \frac{{R_2}^2}{d_{32}} + \frac{{R_2}^2}{d_{12}} \frac{{R_1}^2}{d_{21}} \frac{{R_4}^2}{d_{34}} + \frac{{R_4}^2}{d_{14}} \left[\left(1 - \frac{\dot{R}_2}{c} \right) R_2 + \frac{4\mu}{\rho c} \right] \frac{{R_1}^2}{d_{31}} \\
& - \left[\left(1 - \frac{\dot{R}_1}{c} \right) R_1 + \frac{4\mu}{\rho c} \right] \left[\left(1 - \frac{\dot{R}_2}{c} \right) R_2 + \frac{4\mu}{\rho c} \right] \frac{{R_4}^2}{d_{34}} - \frac{{R_2}^2}{d_{12}} \frac{{R_4}^2}{d_{24}} \frac{{R_1}^2}{d_{31}} - \frac{{R_4}^2}{d_{14}} \frac{{R_1}^2}{d_{21}} \frac{{R_2}^2}{d_{32}} \Bigg\} \left[A_4 \right. \\
& \left. - \frac{3}{2} \left[1 - \frac{\dot{R}_4}{3c} \right] \dot{R}_4^2 - \frac{2R_1 \dot{R}_1^2}{d_{41}} - \frac{2R_2 \dot{R}_2^2}{d_{42}} - \frac{2R_3 \dot{R}_3^2}{d_{43}} \right] \Bigg\} / \\
& / \Bigg\{ \left[\left(1 - \frac{\dot{R}_1}{c} \right) R_1 + \frac{4\mu}{\rho c} \right] \Bigg(\left[\left(1 - \frac{\dot{R}_2}{c} \right) R_2 + \frac{4\mu}{\rho c} \right] \left[\left(1 - \frac{\dot{R}_3}{c} \right) R_3 + \frac{4\mu}{\rho c} \right] \left[\left(1 - \frac{\dot{R}_4}{c} \right) R_4 + \frac{4\mu}{\rho c} \right] \\
& + \frac{{R_3}^2}{d_{23}} \frac{{R_4}^2}{d_{34}} \frac{{R_2}^2}{d_{42}} + \frac{{R_4}^2}{d_{24}} \frac{{R_2}^2}{d_{32}} \frac{{R_3}^2}{d_{43}} - \left[\left(1 - \frac{\dot{R}_2}{c} \right) R_2 + \frac{4\mu}{\rho c} \right] \frac{{R_4}^2}{d_{34}} \frac{{R_3}^2}{d_{43}} - \frac{{R_3}^2}{d_{23}} \frac{{R_2}^2}{d_{32}} \left[\left(1 - \frac{\dot{R}_4}{c} \right) R_4 + \frac{4\mu}{\rho c} \right] \\
& - \frac{{R_4}^2}{d_{24}} \left[\left(1 - \frac{\dot{R}_3}{c} \right) R_3 + \frac{4\mu}{\rho c} \right] \frac{{R_2}^2}{d_{42}} \Bigg) \\
& + \frac{{R_2}^2}{d_{12}} \Bigg(\frac{{R_1}^2}{d_{21}} \frac{{R_4}^2}{d_{34}} \frac{{R_3}^2}{d_{43}} + \frac{{R_3}^2}{d_{23}} \frac{{R_1}^2}{d_{31}} \left[\left(1 - \frac{\dot{R}_4}{c} \right) R_4 + \frac{4\mu}{\rho c} \right] + \frac{{R_4}^2}{d_{24}} \left[\left(1 - \frac{\dot{R}_3}{c} \right) R_3 + \frac{4\mu}{\rho c} \right] \frac{{R_1}^2}{d_{41}} \\
& - \frac{{R_1}^2}{d_{21}} \left[\left(1 - \frac{\dot{R}_3}{c} \right) R_3 + \frac{4\mu}{\rho c} \right] \left[\left(1 - \frac{\dot{R}_3}{c} \right) R_3 + \frac{4\mu}{\rho c} \right] - \frac{{R_3}^2}{d_{23}} \frac{{R_4}^2}{d_{34}} \frac{{R_1}^2}{d_{41}} - \frac{{R_4}^2}{d_{24}} \frac{{R_1}^2}{d_{31}} \frac{{R_3}^2}{d_{43}} \Bigg) \\
& + \frac{{R_3}^2}{d_{13}} \Bigg(\frac{{R_1}^2}{d_{21}} \frac{{R_2}^2}{d_{32}} \left[\left(1 - \frac{\dot{R}_4}{c} \right) R_4 + \frac{4\mu}{\rho c} \right] + \left[\left(1 - \frac{\dot{R}_2}{c} \right) R_2 + \frac{4\mu}{\rho c} \right] \frac{{R_4}^2}{d_{34}} \frac{{R_1}^2}{d_{41}} + \frac{{R_4}^2}{d_{24}} \frac{{R_1}^2}{d_{31}} \frac{{R_2}^2}{d_{42}} \\
& - \frac{{R_1}^2}{d_{21}} \frac{{R_4}^2}{d_{34}} \frac{{R_2}^2}{d_{42}} - \left[\left(1 - \frac{\dot{R}_2}{c} \right) R_2 + \frac{4\mu}{\rho c} \right] \frac{{R_1}^2}{d_{31}} \left[\left(1 - \frac{\dot{R}_4}{c} \right) R_4 + \frac{4\mu}{\rho c} \right] - \frac{{R_4}^2}{d_{24}} \frac{{R_2}^2}{d_{32}} \frac{{R_1}^2}{d_{41}} \Bigg) \\
& + \frac{{R_4}^2}{d_{14}} \Bigg(\frac{{R_1}^2}{d_{21}} \left[\left(1 - \frac{\dot{R}_3}{c} \right) R_3 + \frac{4\mu}{\rho c} \right] \frac{{R_2}^2}{d_{42}} + \left[\left(1 - \frac{\dot{R}_2}{c} \right) R_2 + \frac{4\mu}{\rho c} \right] \frac{{R_1}^2}{d_{31}} \frac{{R_3}^2}{d_{43}} + \frac{{R_3}^2}{d_{23}} \frac{{R_2}^2}{d_{32}} \frac{{R_1}^2}{d_{41}} \\
& - \frac{{R_1}^2}{d_{21}} \frac{{R_2}^2}{d_{32}} \frac{{R_3}^2}{d_{43}} - \left[\left(1 - \frac{\dot{R}_2}{c} \right) R_2 + \frac{4\mu}{\rho c} \right] \left[\left(1 - \frac{\dot{R}_3}{c} \right) R_3 + \frac{4\mu}{\rho c} \right] \frac{{R_1}^2}{d_{41}} - \frac{{R_3}^2}{d_{23}} \frac{{R_1}^2}{d_{31}} \frac{{R_2}^2}{d_{42}} \Bigg) \Bigg\}
\end{aligned}
$$

$$
\begin{aligned}
\ddot{R}_4 = \Bigg\{ & \Bigg\{ \frac{{R_1}^2}{d_{21}} \Bigg[\left(1 - \frac{\dot{R}_3}{c} \right) R_3 + \frac{4\mu}{\rho c} \Bigg] \frac{{R_2}^2}{d_{42}} + \Bigg[\left(1 - \frac{\dot{R}_2}{c} \right) R_2 + \frac{4\mu}{\rho c} \Bigg] \frac{{R_1}^2}{d_{31}} \frac{{R_3}^2}{d_{43}} + \frac{{R_3}^2}{d_{23}} \frac{{R_2}^2}{d_{32}} \frac{{R_1}^2}{d_{41}} - \frac{{R_1}^2}{d_{21}} \frac{{R_2}^2}{d_{32}} \frac{{R_3}^2}{d_{43}} \\
& - \Bigg[\left(1 - \frac{\dot{R}_2}{c} \right) R_2 + \frac{4\mu}{\rho c} \Bigg] \Bigg[\left(1 - \frac{\dot{R}_3}{c} \right) R_3 + \frac{4\mu}{\rho c} \Bigg] \frac{{R_1}^2}{d_{41}} - \frac{{R_3}^2}{d_{23}} \frac{{R_1}^2}{d_{31}} \frac{{R_2}^2}{d_{42}} \Bigg\} \Bigg[A_1 - \frac{3}{2} \Bigg[1 - \frac{\dot{R}_1}{3c} \Bigg] \dot{R}_1^2 \\
& - \frac{2R_2 \dot{R}_2^2}{d_{12}} - \frac{2R_3 \dot{R}_3^2}{d_{13}} - \frac{2R_4 \dot{R}_4^2}{d_{14}} \Bigg] \\
& + \Bigg\{ \Bigg[\left(1 - \frac{\dot{R}_1}{c} \right) R_1 + \frac{4\mu}{\rho c} \Bigg] \frac{{R_2}^2}{d_{32}} \frac{{R_3}^2}{d_{43}} + \frac{{R_2}^2}{d_{12}} \Bigg[\left(1 - \frac{\dot{R}_3}{c} \right) R_3 + \frac{4\mu}{\rho c} \Bigg] \frac{{R_1}^2}{d_{41}} + \frac{{R_3}^2}{d_{13}} \frac{{R_1}^2}{d_{31}} \frac{{R_2}^2}{d_{42}} \\
& - \Bigg[\left(1 - \frac{\dot{R}_1}{c} \right) R_1 + \frac{4\mu}{\rho c} \Bigg] \Bigg[\left(1 - \frac{\dot{R}_3}{c} \right) R_3 + \frac{4\mu}{\rho c} \Bigg] \frac{{R_2}^2}{d_{42}} - \frac{{R_2}^2}{d_{12}} \frac{{R_1}^2}{d_{31}} \frac{{R_3}^2}{d_{43}} - \frac{{R_3}^2}{d_{13}} \frac{{R_2}^2}{d_{32}} \frac{{R_1}^2}{d_{41}} \Bigg\} \Bigg[A_2 \\
& - \frac{3}{2} \Bigg[1 - \frac{\dot{R}_2}{3c} \Bigg] \dot{R}_2^2 - \frac{2R_1 \dot{R}_1^2}{d_{21}} - \frac{2R_3 \dot{R}_3^2}{d_{23}} - \frac{2R_4 \dot{R}_4^2}{d_{24}} \Bigg] \\
& + \Bigg\{ \Bigg[\left(1 - \frac{\dot{R}_1}{c} \right) R_1 + \frac{4\mu}{\rho c} \Bigg] \frac{{R_3}^2}{d_{23}} \frac{{R_2}^2}{d_{42}} + \frac{{R_2}^2}{d_{12}} \frac{{R_1}^2}{d_{21}} \frac{{R_3}^2}{d_{43}} + \frac{{R_3}^2}{d_{13}} \Bigg[\left(1 - \frac{\dot{R}_2}{c} \right) R_2 + \frac{4\mu}{\rho c} \Bigg] \frac{{R_1}^2}{d_{41}} \\
& - \Bigg[\left(1 - \frac{\dot{R}_1}{c} \right) R_1 + \frac{4\mu}{\rho c} \Bigg] \Bigg[\left(1 - \frac{\dot{R}_2}{c} \right) R_2 + \frac{4\mu}{\rho c} \Bigg] \frac{{R_3}^2}{d_{43}} - \frac{{R_2}^2}{d_{12}} \frac{{R_3}^2}{d_{23}} \frac{{R_1}^2}{d_{41}} - \frac{{R_3}^2}{d_{13}} \frac{{R_1}^2}{d_{21}} \frac{{R_2}^2}{d_{42}} \Bigg\} \Bigg[A_3 \\
& - \frac{3}{2} \Bigg[1 - \frac{\dot{R}_3}{3c} \Bigg] \dot{R}_3^2 - \frac{2R_1 \dot{R}_1^2}{d_{31}} - \frac{2R_2 \dot{R}_2^2}{d_{32}} - \frac{2R_4 \dot{R}_4^2}{d_{34}} \Bigg] \\
& + \Bigg\{ \Bigg[\left(1 - \frac{\dot{R}_1}{c} \right) R_1 + \frac{4\mu}{\rho c} \Bigg] \Bigg[\left(1 - \frac{\dot{R}_2}{c} \right) R_2 + \frac{4\mu}{\rho c} \Bigg] \Bigg[\left(1 - \frac{\dot{R}_3}{c} \right) R_3 + \frac{4\mu}{\rho c} \Bigg] + \frac{{R_2}^2}{d_{12}} \frac{{R_3}^2}{d_{23}} \frac{{R_1}^2}{d_{31}} \\
& + \frac{{R_3}^2}{d_{13}} \frac{{R_1}^2}{d_{21}} \frac{{R_2}^2}{d_{32}} - \Bigg[\left(1 - \frac{\dot{R}_1}{c} \right) R_1 + \frac{4\mu}{\rho c} \Bigg] \frac{{R_3}^2}{d_{23}} \frac{{R_2}^2}{d_{32}} - \frac{{R_2}^2}{d_{12}} \frac{{R_1}^2}{d_{21}} \Bigg[\left(1 - \frac{\dot{R}_3}{c} \right) R_3 + \frac{4\mu}{\rho c} \Bigg] \\
& - \frac{{R_3}^2}{d_{13}} \Bigg[\left(1 - \frac{\dot{R}_2}{c} \right) R_2 + \frac{4\mu}{\rho c} \Bigg] \frac{{R_1}^2}{d_{31}} \Bigg\} \Bigg[A_4 - \frac{3}{2} \Bigg[1 - \frac{\dot{R}_4}{3c} \Bigg] \dot{R}_4^2 - \frac{2R_1 \dot{R}_1^2}{d_{41}} - \frac{2R_2 \dot{R}_2^2}{d_{42}} - \frac{2R_3 \dot{R}_3^2}{d_{43}} \Bigg] \Bigg\} / \\
& / \Bigg\{ \Bigg[\left(1 - \frac{\dot{R}_1}{c} \right) R_1 + \frac{4\mu}{\rho c} \Bigg] \Bigg(\Bigg[\left(1 - \frac{\dot{R}_2}{c} \right) R_2 + \frac{4\mu}{\rho c} \Bigg] \Bigg[\left(1 - \frac{\dot{R}_3}{c} \right) R_3 + \frac{4\mu}{\rho c} \Bigg] \Bigg[\left(1 - \frac{\dot{R}_4}{c} \right) R_4 + \frac{4\mu}{\rho c} \Bigg] \\
& + \frac{{R_3}^2}{d_{23}} \frac{{R_4}^2}{d_{34}} \frac{{R_2}^2}{d_{42}} + \frac{{R_4}^2}{d_{24}} \frac{{R_2}^2}{d_{32}} \frac{{R_3}^2}{d_{43}} - \Bigg[\left(1 - \frac{\dot{R}_2}{c} \right) R_2 + \frac{4\mu}{\rho c} \Bigg] \frac{{R_4}^2}{d_{34}} \frac{{R_3}^2}{d_{43}} \\
& - \frac{{R_3}^2}{d_{23}} \frac{{R_2}^2}{d_{32}} \Bigg[\left(1 - \frac{\dot{R}_4}{c} \right) R_4 + \frac{4\mu}{\rho c} \Bigg] - \frac{{R_4}^2}{d_{24}} \Bigg[\left(1 - \frac{\dot{R}_3}{c} \right) R_3 + \frac{4\mu}{\rho c} \Bigg] \frac{{R_2}^2}{d_{42}} \Bigg) \\
& + \frac{{R_2}^2}{d_{12}} \Bigg(\frac{{R_1}^2}{d_{21}} \frac{{R_4}^2}{d_{34}} \frac{{R_3}^2}{d_{43}} + \frac{{R_3}^2}{d_{23}} \frac{{R_1}^2}{d_{31}} \Bigg[\left(1 - \frac{\dot{R}_4}{c} \right) R_4 + \frac{4\mu}{\rho c} \Bigg] + \frac{{R_4}^2}{d_{24}} \Bigg[\left(1 - \frac{\dot{R}_3}{c} \right) R_3 + \frac{4\mu}{\rho c} \Bigg] \frac{{R_1}^2}{d_{41}} \\
& - \frac{{R_1}^2}{d_{21}} \Bigg[\left(1 - \frac{\dot{R}_3}{c} \right) R_3 + \frac{4\mu}{\rho c} \Bigg] \Bigg[\left(1 - \frac{\dot{R}_3}{c} \right) R_3 + \frac{4\mu}{\rho c} \Bigg] - \frac{{R_3}^2}{d_{23}} \frac{{R_4}^2}{d_{34}} \frac{{R_1}^2}{d_{41}} - \frac{{R_4}^2}{d_{24}} \frac{{R_1}^2}{d_{31}} \frac{{R_3}^2}{d_{43}} \Bigg) \\
& + \frac{{R_3}^2}{d_{13}} \Bigg(\frac{{R_1}^2}{d_{21}} \frac{{R_2}^2}{d_{32}} \Bigg[\left(1 - \frac{\dot{R}_4}{c} \right) R_4 + \frac{4\mu}{\rho c} \Bigg] + \Bigg[\left(1 - \frac{\dot{R}_2}{c} \right) R_2 + \frac{4\mu}{\rho c} \Bigg] \frac{{R_4}^2}{d_{34}} \frac{{R_1}^2}{d_{41}} + \frac{{R_4}^2}{d_{24}} \frac{{R_1}^2}{d_{31}} \frac{{R_2}^2}{d_{42}} \\
& - \frac{{R_1}^2}{d_{21}} \frac{{R_4}^2}{d_{34}} \frac{{R_2}^2}{d_{42}} - \Bigg[\left(1 - \frac{\dot{R}_2}{c} \right) R_2 + \frac{4\mu}{\rho c} \Bigg] \frac{{R_1}^2}{d_{31}} \Bigg[\left(1 - \frac{\dot{R}_4}{c} \right) R_4 + \frac{4\mu}{\rho c} \Bigg] - \frac{{R_4}^2}{d_{24}} \frac{{R_2}^2}{d_{32}} \frac{{R_1}^2}{d_{41}} \Bigg)
\end{aligned}
$$

$$+\frac{{R_4}^2}{d_{14}}\left(\frac{{R_1}^2}{d_{21}}\left[\left(1-\frac{\dot{R}_3}{c}\right)R_3+\frac{4\mu}{\rho c}\right]\frac{{R_2}^2}{d_{42}}+\left[\left(1-\frac{\dot{R}_2}{c}\right)R_2+\frac{4\mu}{\rho c}\right]\frac{{R_1}^2}{d_{31}}\frac{{R_3}^2}{d_{43}}+\frac{{R_3}^2}{d_{23}}\frac{{R_2}^2}{d_{32}}\frac{{R_1}^2}{d_{41}}\right.$$
$$\left.-\frac{{R_1}^2}{d_{21}}\frac{{R_2}^2}{d_{32}}\frac{{R_3}^2}{d_{43}}-\left[\left(1-\frac{\dot{R}_2}{c}\right)R_2+\frac{4\mu}{\rho c}\right]\left[\left(1-\frac{\dot{R}_3}{c}\right)R_3+\frac{4\mu}{\rho c}\right]\frac{{R_1}^2}{d_{41}}-\frac{{R_3}^2}{d_{23}}\frac{{R_1}^2}{d_{31}}\frac{{R_2}^2}{d_{42}}\right)\Bigg\}$$

Bibliography

1. *Classe de Philosophie experinentale.* **Eueler, L.** 1754, Historie de l' Academie Royale des Sciences et Belles Letter, Vol. 10, pp. 227-295.

2. *Investigations into the Causes of Corrosion or Erosion of Propellers.* **Parsons, C. A., & Cook, S. S.** 2, 1919, Naval Engineers Journal, Vol. 31, pp. 536-541.

3. *VIII. On the pressure developed in a liquid during the collapse of a spherical cavity.* **Rayleigh, L.** 200, 1917, The London, Edinburgh, and Dublin Philosophical Magazine and Journal of Science, Vol. 34, pp. 94-98.

4. *The dynamics of cavitation bubbles.* **Plesset, M. S.** 1949, Journal of applied mechanics, Vol. 16, pp. 277-282.

5. *Bubble oscillations of large amplitude.* **Keller, J. B., & Miksis, M.** 2, 1980, The Journal of the Acoustical Society of America , Vol. 68, pp. 628-633.

6. *Ultrasound cardiography: contrast studies in anatomy and function.* **Gramiak, R., Shah, P. M., & Kramer, D. H.939-948.** 5, 1969, Radiology, Vol. 92, pp. 939-948.

7. *Ultrasonic detection of cavitation at catheter tips.* **Kremkau, F. W., Gramiak, R., Carstensen, E. L., Shah, P. M., & Kramer, D. H.** 1, 1970, American Journal of Roentgenology, Vol. 110, pp. 177-183.

8. *Bifurcation structure of bubble oscillators.* **Parlitz, U., Englisch, V., Scheffczyk, C., & Lauterborn, W.** 2, 1990, The Journal of the Acoustical Society of America, Vol. 88, pp. 1061-1077.

9. *Classification of the nonlinear dynamics and bifurcation structure of ultrasound contrast agents excited at higher multiples of their resonance frequency.* **Sojahrood, A. J., & Kolios, M. C.** 33, 2012, Physics Letters A, Vol. 376, pp. 2222-2229.

10. *Subharmonic route to chaos observed in acoustics.* **Lauterborn, W., & Cramer, E.** 20, 1981, Physical Review Letters, Vol. 47, p. 1445.

11. *Holographic observation of period-doubled and chaotic bubble oscillations in acoustic cavitation.* **Lauterborn, W., & Koch, A.** 4, 1987, Physical Review A, Vol. 35, p. 1974.

12. *Nonlinear transitions of a spherical cavitation bubble.* **Behnia, S., Jafari, A., Soltanpoor, W., & Jahanbakhsh, O.** 2, 2009, Chaos, Solitons & Fractals, Vol. 41, pp. 818-828.

13. *Stable period 1, 2 and 3 structures of the harmonically excited Rayleigh–Plesset equation applying low ambient pressure.* **Hegedűs, F., Hős, C., & Kullmann, L.** 6, 2012, Journal of Applied Mathematics, Vol. 78, pp. 1179-1195.

14. *Chaotic dynamics of microbubbles in ultrasonic fields.* **Macdonald, C. A., & Gomatam, J.** 3, 2006, Proceedings of the Institution of Mechanical Engineers, Part C: Journal of Mechanical Engineering Science, Vol. 220, pp. 333-343.

15. *Chaotic sonoluminescence.* **Holt, R. G., Gaitan, D. F., Atchley, A. A., & Holzfuss, J.** 9, 1994, Physical review letters, Vol. 72, p. 1376.

16. *Towards classification of the bifurcation structure of a spherical cavitation bubble.* **Behnia, S., Sojahrood, A. J., Soltanpoor, W., & Sarkhosh, L.** 8, 2009, Ultrasonics, Vol. 49, pp. 605-610.

17. *Bifurcation superstructure in a model of acoustic turbulence.* **Lauterborn, W., & Suchla, E.** 24, 1984, Physical review letters, Vol. 53, p. 2304.

18. *Sonoluminescence from single bubbles.* **Gaitan, D. F., & Crum, L. A.** S1, 1990, The Journal of the Acoustical Society of America, Vol. 87, pp. S141-S141.

19. *Modelling acoustic scattering, sound speed, and attenuation in gassy soft marine sediments.* **Mantouka, A., Dogan, H., White, P. R., & Leighton, T. G.** 1, 2016, The Journal of the Acoustical Society of America, Vol. 140, pp. 274-282.

20. **Etter, P. C.** *Underwater acoustic modeling and simulation.* s.l. : CRC Press, 2018.

21. *Ultrasound microbubble contrast agents: fundamentals and application to gene and drug delivery.* **Ferrara, K., Pollard, R. and Borden, M.** 2007, Annual review of biomedical engineering, p. 9.

22. *Ultrafast ultrasound localization microscopy for deep super-resolution vascular imaging.* **Errico, C., Pierre, J., Pezet, S., Desailly, Y., Lenkei, Z., Couture, O., & Tanter, M.** 7579, 2015, Nature, Vol. 527, p. 499.

23. *Clinical trial of blood-brain barrier disruption by pulsed ultrasound.* **Carpentier, A., Canney, M., Vignot, A., Reina, V., Beccaria, K., Horodyckid, C., Karachi, C., Leclercq, D., Lafon, C., Chapelon, J.Y. and Capelle, L.** 343, 2016, Science translational medicine, Vol. 8, pp. 343re2-343re2.

24. *Focused ultrasound-mediated drug delivery through the blood–brain barrier.* **Burgess, A., Shah, K., Hough, O., & Hynynen, K.** 5, 2015, Expert review of neurotherapeutics, Vol. 15, pp. 477-491.

25. *Controlled vesicle deformation and lysis by single oscillating bubbles.* **Marmottant, P., & Hilgenfeldt, S.** 6936, 2003, Nature, Vol. 423, p. 153.

26. *Membrane disruption by optically controlled microbubble cavitation.* **Prentice, P., Cuschieri, A., Dholakia, K., Prausnitz, M., & Campbell, P.** 2, 2005, Nature physics, Vol. 1, p. 107.

27. *Microbubbles as ultrasound contrast agents and in targeted drug delivery.* **Sheffield, P., Trehan, A., Boyd, B., & Wong, O. L.** 4, 2008, Critical Reviews™ in Biomedical Engineering, Vol. 36.

28. *Basic acoustic properties of microbubbles.* **De Jong, N., Bouakaz, A., & Frinking, P.** 3, 2002, Echocardiography, Vol. 19, pp. 229-240.

29. *Subharmonic imaging of contrast agents.* **Forsberg, F., Shi, W. T., & Goldberg, B. B.** 1-8, 2000, Ultrasonics, Vol. 38, pp. 93-98.

30. *Ultrasound contrast agents: an overview.* **Cosgrove, D.** 3, 2006, European journal of radiology, Vol. 60, pp. 324-330.

31. *Advantages of subharmonic over second harmonic backscatter for contrast-to-tissue echo enhancement.* **Shankar, P. M., Krishna, P. D., & Newhouse, V. L.** 3, 1998, Ultrasound in Medicine and Biology, Vol. 24, pp. 395-399.

32. *Cavitation bubble cluster activity in the breakage of kidney stones by lithotripter shockwaves.* **Pishchalnikov, Y. A., Sapozhnikov, O. A., Bailey, M. R., Williams Jr, J. C., Cleveland, R. O., Colonius, T., ... & McAteer, J. A.** v, 2003, Journal of endourology, Vol. 17, pp. 435-446.

33. *A millisecond micromixer via single-bubble-based acoustic streaming.* **Ahmed, D., Mao, X., Shi, J., Juluri, B. K., & Huang, T. J.** 18, 2009, Lab on a Chip, Vol. 9, pp. 2738-2741.

34. *Encapsulated ultrasound microbubbles: therapeutic application in drug/gene delivery.* **Liu, Y., Miyoshi, H., & Nakamura, M.** 1, 2006, Journal of controlled release, Vol. 114, pp. 89-99.

35. *Ultrasound-induced cell membrane porosity.* **Deng, C. X., Sieling, F., Pan, H., & Cui, J.** 4, 2004, Ultrasound in Medicine and Biology, Vol. 30, pp. 519-526.

36. *Focal disruption of the blood–brain barrier due to 260-kHz ultrasound bursts: a method for molecular imaging and targeted drug delivery.* **Hynynen, K., McDannold, N., Vykhodtseva, N., Raymond, S., Weissleder, R., Jolesz, F. A., & Sheikov, N.** 3, 2006, Journal of neurosurgery, Vol. 105, pp. 445-454.

37. *Sonoluminescence from single bubbles.* **Gaitan, D. F., & Crum, L. A.** S1, 1990, The Journal of the Acoustical Society of America, Vol. 87, pp. S141-S141.

38. *Sonoluminescence: Inside a micro-reactor.* **Lohse, D.** 6896, 2002, Nature, Vol. 418, p. 381.

39. *Chemical reactions in a sonoluminescing bubble.* **Yasui, K.** 9, 1997, Journal of the Physical Society of Japan, Vol. 66, pp. 2911-2920.

40. *The effects of coupling and bubble size on the dynamical-systems behaviour of a small cluster of microbubbles.* **Chong, K. J. Y., Quek, C. Y., Dzaharudin, F., Ooi, A., & Manasseh, R.** 6, 2010, Journal of Sound and Vibration, Vol. 329, pp. 687-699.

41. *Nonlinearity in the interaction of ultrasound contrast agents under the periodic acoustic forcing.* **Retkute, R., Macdonald, C., & Gomatam, J.** 2, 2010, EPL (Europhysics Letters), Vol. 89, p. 20010.

42. *Nonlinear oscillations of a cluster of bubbles in a sound field: Bifurcation structure.* **Takahira, H., Yamane, S., & Akamatsu, T.** 3, 1995, JSME International Journal Series B Fluids and Thermal Engineering, Vol. 38, pp. 432-439.

43. **Landau, L. D. & EM Lifshitz.** *Fluid Mechanics. Course of Theoretical Physics, 2nd edition.* s.l. : Butterworth-Heinemann, 1987.

44. **Keenan, J.H., F.G. Keyes, P.G. Hill, and B.S. Moore.** *Steam Tables: Thermodynamic Properties of Water Including Vapor, Liquid, and Solid Phases/With Charts.* New York : John Wiley & Sons Inc, 1969, pp. 104–107.

45. *A variable order Runge-Kutta method for initial value problems with rapidly varying right-hand sides.* **Cash, J. R., & Karp, A. H.** 3, 1990, ACM Transactions on Mathematical Software (TOMS), Vol. 16, pp. 201-222.

46. **Cramer, & Gabriel.** *Introduction a l'analyse des lignes courbes algebriques.* s.l. : Nabu Press, 1970.

47. *Numerical investigation of nonlinear oscillations of gas bubbles in liquids.* **Lauterborn, W.** 2, 1976, The Journal of the Acoustical Society of America, Vol. 59, pp. 283-293.

48. *Microbubbles in medical imaging: current applications and future directions.* **Lindner, J. R.** 6, 2004, Nature Reviews Drug Discovery, Vol. 3, p. 527.

49. *Microbubble size isolation by differential centrifugation.* **Feshitan, J. A., Chen, C. C., Kwan, J. J., & Borden, M. A.** 2, 2009, Journal of colloid and interface science, Vol. 329, pp. 316-324.

50. *Nonlinear shell behavior of phospholipid-coated microbubbles.* **Overvelde, M., Garbin, V., Sijl, J., Dollet, B., De Jong, N., Lohse, D., & Versluis, M.** 12, 2010, Ultrasound in medicine and biology, Vol. 36, pp. 2080-2092.

51. *A model for large amplitude oscillations of coated bubbles accounting for buckling and rupture.* **Marmottant, P., van der Meer, S., Emmer, M., Versluis, M., de Jong, N., Hilgenfeldt, S., & Lohse, D.** 6, 2005, The Journal of the Acoustical Society of America, Vol. 118, pp. 3499-3505.

52. *Ultrasound signal from sub-micron lipid-coated bubbles.* **Hernandez, C., Lilly, J. L., Nittayacharn, P., Hadley, J., Coyne, R., Kolios, M., & Exner, A. A.** 2017. Ultrasonics Symposium (IUS), 2017 IEEE International .

53. *investigation of the nonlinear dynamics of nanobubbles excited at clinically relevant ultrasound frequencies and pressures: The role oflipid shell buckling.* **JafariSojahrood, A., Nieves, L., Hernandez, C., Exner, A., & Kolios, M. C.** 2017. Ultrasonics Symposium (IUS), 2017 IEEE International.

54. *Frequency dependence of ultrasound attenuation and backscatter in breast tissue.* **d'Astous, F. T., & Foster, F. S.** 10, 1986, Ultrasound in Medicine and Biology, Vol. 12, pp. 795-808.

55. *Nonlinear model of acoustical attenuation and speed of sound in a bubbly medium.* **Sojahrood, A. J., Haghi, H., Karshafian, R., & Kolios, M. C.** 2015. Ultrasonics Symposium (IUS), 2015 IEEE International.

56. *Microbubble size isolation by differential centrifugation.* **Feshitan, J. A., Chen, C. C., Kwan, J. J., & Borden, M. A.** 2, 2009, Journal of colloid and interface science, Vol. 329, pp. 316-324.

57. *Acoustic bubble sorting for ultrasound contrast agent enrichment.* **Segers, T., & Versluis, M.** 10, 2014, Lab on a Chip, Vol. 14, pp. 1705-1714.